Deutsches Biomasseforschungszentrum
gemeinnützige GmbH

DBFZ REPORT NO. 57

Surface Diffusion and Adsorption of Gas Mixtures in Selective Carbon Membranes

Doctoral thesis
Matthis Reinke Kurth

In Cooperation with:

IMPRINT

Publisher:
DBFZ Deutsches Biomasseforschungszentrum
gemeinnützige GmbH
Torgauer Straße 116
04347 Leipzig
Phone: +49 (0)341 2434-112
info@dbfz.de

Funding:
DBFZ Deutsches Biomasseforschungszentrum gemeinnützige GmbH, Leipzig, an enterprise of the German Government with funding from the Federal Ministry of Agriculture, Food and Regional Identity pursuant to a resolution by the German Bundestag.

With support from
Federal Ministry of Agriculture, Food and Regional Identity
by decision of the German Bundestag

General Management:
Prof. Dr. mont. Michael Nelles
(Scientific Managing Director)
Dr. Christoph Krukenkamp
(Administrative Managing Director)

DBFZ Report No. 57
Surface Diffusion and Adsorption of Gas Mixtures in Selective Carbon Membranes
Leipzig: DBFZ, 2026
ISSN: 2197-4632 (Online)
ISBN: 978-3-949807-49-7
DOI: 10.48480/rhz7-gr32

Author:
Matthis Reinke Kurth

Pictures:
If not indicated on the image: DBFZ, Stefanie Bader (Map)
Title: Rico Ehrentraut (left), Magnific.com

Date of Publication:
09/2026

DIRECTIONS

By train: Arrival Leipzig main station; streetcar line 3/3E (direction Taucha/Sommerfeld) to stop Bautzner Straße; cross the street, leave the parking lot on the right and use the main entrance of the DBFZ (house 1, Torgauer Str. 116). Please register at the reception.

By car: on the A 14 motorway. Exit at Leipzig Nord-Ost; follow signs for Taucha; then follow signs for Leipzig; then follow signs for Zentrum, Innenstadt. Turn off left after the "bft" filling station (see "By train" for further directions).

By tram: line 3/3 E towards Taucha/Sommerfeld; Bautzner Strasse stop (see "By train" for further directions)

The German National Library lists these publications in the German National Bibliography; detailed bibliographic data are available on the Internet at the address www.dnb.de.

Surface Diffusion and Adsorption of Gas Mixtures in Selective Carbon Membranes

vorgelegt von
M. Sc.
Matthis Reinke Kurth
ORCID: 0000-0002-1894-6369

an der Fakultät III – Prozesswissenschaften
der Technischen Universität Berlin
zur Erlangung des akademischen Grades

Doktor der Ingenieurwissenschaften
- Dr.-Ing. -

Dissertation

Promotionsausschuss:

Vorsitzende:	Prof. Dr. Aleksander Gurlo
Gutachter:	Prof. Dr.-Ing. habil. Jens-Uwe Repke
Gutachter:	Prof. Dr.rer. nat. Ingolf Voigt

Berlin 2025

Dedicated to the collaborative and unbiased spirit of academia.

Affidavit

Hiermit erkläre ich an Eides statt, dass ich die vorliegende Arbeit selbstständig und eigenhändig sowie ausschließlich unter Verwendung der aufgeführten Quellen und Hilfsmittel angefertigt habe. KI-Sprachmodelle von *DeepL SE* (DeepL Write) und von *OpenAI* (GPT-4o) wurden ausschließlich verwendet, um bestehende englische Sätze umzuschreiben und so das Verständnis der englischen Sprache zu verbessern. Die inhaltliche Verantwortung für alle Aussagen liegt bei mir.

M. Sc.
Matthis Reinke Kurth
Hamburg, 26. August 2025

I hereby confirm that I prepared this thesis independently and by exclusive reliance on literature or tools indicated herein. AI language models from DeepL SE (DeepL Write) and OpenAI (GPT-4o) were used solely to rephrase existing English sentences to improve understanding of the English language. I am responsible for the content of all statements.

M. Sc.
Matthis Reinke Kurth
Hamburg, August 26, 2025

Acknowledgements

First, I want to thank Prof. Jens-Uwe Repke, my Ph.D. supervisor, for his guidance and support throughout this process. His expertise and focus have been invaluable.

I am grateful to the University of Queensland in Brisbane, Australia, where I developed much of my modeling approach. A special thanks to Prof. Suresh K. Bhatia for his time, clear explanations, and open-mindedness. I have learned a great deal from him. I also appreciate Gloria Monsalve Bravo for the engaging scientific discussions during my time at UQ.

My colleagues at TU Berlin have been a tremendous support. I would like to extend special thanks to M.Sc. Javed Mudassar for his assistance with the adsorption experiments, and to M.Sc. Volodymyr Kozachynskyi for his help with code checking and advice, which greatly enhanced my modeling and optimization work.

I appreciate the support from the DBFZ during this period. I also especially thank Dr.-Ing. Marco Klemm for his assistance in addressing various challenges.

I would like to acknowledge my colleagues at the DBFZ: Jakob Köchermann, Selina Nieß, Alexander Feist, Thomas Hirsch, and Sebastian Dietrich for their support and collaboration.

Thank you to Dr. Ing. Marcus Weyd from the Fraunhofer IKTS for his guidance in making decisions related to the experimental field.

I am grateful to my parents, Dipl.-Päd Anna-Maria Muschik and Dipl.-Ing. Reinhard Kurth, for their support and belief in my choices. A special "thank you" to my avid reader sister Frauke Diegner - her corrections were invaluable during the final stages.

Finally, I appreciate my partner, Edith, for her support and for sharing this journey with me.

Abstract

Deutsch

Die Motivation für diese Arbeit liegt im wachsenden Interesse an den Prozessen zur Herstellung von synthetischem Erdgas (SNG) aus alternativen Quellen wie biogenen Rohstoffen. Diese Prozesse sind entscheidend für die Reduzierung von Treibhausgasemissionen und die Verbesserung der Energieunabhängigkeit. Membranen in katalytischen Reaktoren verbessern die Reaktionseffizienz und Selektivität, indem sie Reaktion und Trennung in einem einzigen System koppeln, ohne dass der Gasstrom weiterverarbeitet werden muss. Diese Arbeit präsentiert eine umfassende Untersuchung der Adsorptions- und Stofftransportphänomene von Wasserstoff (H_2), Wasser (H_2O) und Methan (CH_4) in kohlenstoffbasierten nanoporösen Membranen unter erhöhten Temperaturbedingungen. Die Studie umfasst eine Reihe von Adsorptions- und Permeationsexperimenten, die an einem neuartigen nanoporösen Kohlenstoffmembranmaterial durchgeführt wurden, das vom Fraunhofer IKTS entwickelt wurde. Der Einsatz dieser kohlenstoffbasierten Membran ermöglicht den Betrieb unter härteren Bedingungen und ermöglicht es den Prozessen, optimale Reaktionsparameter zu erreichen. Adsorptionsmessungen wurden bei Temperaturen von 90 °C bis 120 °C und Drücken bis zu 45 bar durchgeführt. Diese Bedingungen wurden aufgrund von Einschränkungen der experimentellen Geräte und zur Erreichung der höchsten technisch erreichbaren Temperaturen gewählt, da die CO_2-Methanisierung typischerweise bei Temperaturen über 280 °C betrieben wird. Die Langmuir-Isotherme lieferte die beste Übereinstimmung mit den beobachteten Daten. Bemerkenswerterweise wurden die Adsorptionskapazitäten für beide Gase deutlich niedriger als die für konventionelle Kohlenstoffmaterialien berichteten Werte gefunden, was die einzigartigen Eigenschaften der untersuchten nanoporösen Membranstrukturen hervorhebt.

Zusätzlich zu den Adsorptionsstudien wurden Permeationsexperimente bei Temperaturen bis zu 220 °C mit reinen Gasen durchgeführt, was die Berechnung der Maxwell-Stefan-Oberflächendifusionskoeffizienten ermöglichte. Diese Koeffizienten stimmten mit empirischen Modellen überein und liefern wertvolle Daten für zukünftige Mehrkomponentenmodellierungen. Anschließend wurde ein binäres Stofftransportmodell auf Basis des Maxwell-Stefan-Oberflächendiffusionsansatzes entwickelt, das die experimentellen Adsorptions- und Permeationsdaten integriert. Das Modell wurde anhand binärer Experimente validiert und zeigte eine Unterschätzung des Stofftransports von H_2, während der Stofftransport von CH_4 leicht überschätzt wurde. Durch die Anpassung des Confinement-Faktors aus (Krishna und van Baten, 2009) und die Einführung einer optimierten, parameterbasierten logarithmischen Temperaturabhängigkeit konnte eine gute Übereinstimmung mit den binären Experimenten erzielt werden, da der temperaturabhängige Faktor die komplexe Natur der Wechselwirkungen bei höheren Temperaturen berücksichtigt.

Zusätzlich zum binären Modell wurde Wasser als dritte Komponente in Adsorptions- und Permeationsexperimente einbezogen. Ternäre und binäre Permeationsexperimente wurden durchgeführt, deren Daten für zukünftige Forschungsvorhaben genutzt werden können.

Die Ergebnisse dieser Arbeit schließen nicht nur bestehende Lücken in der Literatur zum Adsorptions- und Transportverhalten von H_2 und CH_4 in nanoporösen Membranen bei erhöhten Temperaturen, sondern liefern auch ein robustes Modellierungsframework, das das Verständnis und die Prognosefähigkeit von Gastrennprozessen verbessert. Die gewonnenen Erkenntnisse haben Implikationen für die Entwicklung und Optimierung von Membrantechnologien in Energie- und Umweltanwendungen, insbesondere im Kontext nachhaltiger Energieproduktion sowie Strategien zur Kohlenstoffabscheidung und -nutzung (CCU).

Diese kohlenstoffbasierten Membranen sind unter Anderem für Hochtemperaturprozesse geeignet, die eine selektive Trennung von H_2, CH_4 und H_2O erfordern, wie z.B. Wasserstoffreinigung, Dampfreformierung und die Herstellung synthetischer Kraftstoffe.

Schlüsselwörter: *Kohlenstoffbasierte Membranen, Versuche, Adsorptionsisotherme, Maxwell-Stefan-Diffusionsmodell*

English

The motivation for this work is rooted in the growing interest in CO_2-methanation and the production of synthetic natural gas (SNG) from alternative sources like biogenic feedstocks. These processes are critical for reducing greenhouse gas emissions and enhancing energy independence. Membranes in catalytic reactors enhance reaction efficiency and selectivity by coupling reaction and separation in a single system without the need to further process the gas stream. This work presents a comprehensive investigation of the adsorption and mass transport phenomena of hydrogen (H_2), water (H_2O) and methane (CH_4) in carbon-based nanoporous membranes under elevated temperature conditions. The study includes a series of adsorption and permeation experiments carried out on a novel nanoporous carbon membrane material developed by Fraunhofer IKTS. The use of this carbon-based membrane allows operation under harsher conditions, enabling processes to approach optimal reaction parameters. Adsorption measurements were performed at temperatures ranging from 90 °C to 120 °C and pressures up to 45 bar. These conditions were chosen due to limitations of the experimental devices and to achieve the highest technical achievable temperatures, as CO_2-methanation typically operates at temperatures above 280 °C. The Langmuir isotherm provided the best fit for the observed data. Notably, the adsorption capacities for both gases were found to be significantly lower than those reported for conventional carbon materials, highlighting the unique properties of the investigated nanoporous membrane structures.

In addition to the adsorption studies, single component permeation experiments were carried out at temperatures up to 220 °C, leading to the calculation of Maxwell-Stefan surface diffusion coefficients. These coefficients were found to be in agreement with empirical models, providing valuable data for future multi-component modelling approaches. A binary mass transport model was then developed based on the Maxwell-Stefan surface diffusion framework, integrating the experimental adsorption and permeation data. The model was validated against binary experimental measurements, demonstrating a underestimation of the mass transport of H_2 transport, while slightly overestimating the mass transport of CH_4. By adapting the confinement factor from (Krishna and van Baten, 2009) and introducing an optimized parameter-based logarithmic temperature dependency. With the adaptation the binary experiments could be described with good agreement since the tempera-

ture dependent factor is able to incorporate the undescribed complex nature of the interactions at higher temperatures.

In addition to the binary model, water was introduced as a third component with adsorption and permeation experiments. Ternary and binary permeation experiments were conducted and this data can be used in future research.

The results of this research not only fill open gaps in the existing literature on the adsorption and transport behavior of H_2 and CH_4 in nanoporous membranes, but also provide a robust modelling framework that enhances the understanding and predictive capabilities of gas separation processes. The knowledge gained from this work has implications for the design and optimization of membrane technologies in energy and environmental applications, particularly in the context of sustainable energy production and carbon capture and utilization (CCU) strategies. These carbon-based membranes are applicable to high-temperature processes requiring selective separation of H_2, CH_4, and H_2O, such as hydrogen purification, steam reforming, and synthetic fuel production.

Keywords: *Carbon-based membranes, Experimental trials, adsorption isotherms, Maxwell-Stefan diffusion model*

Publications

This thesis is partially based on already published contributions. In the following, these are divided into Journal articles, papers within conference proceedings, oral presentations without papers, and a list of all supervised theses.

Journal Articles

– M. Kurth, M. Javed, T. Schliermann, G. Brösigke, S. Kämnitz, S. K. Bhatia, J.-U. Repke (2024a): Pure Hydrogen and Methane Permeation in Carbon-Based Nanoporous Membranes: Adsorption Isotherms and Permeation Experiments. *Membranes* 14 (6), 123. ISSN: 2077-0375. DOI: 10.3390/membranes14060123. (Last access 06/15/2024)

– (In preparation:) M. Kurth, G. Monsalve-Bravo, S. K. Bhatia, J.-U. Repke (2025): Adsorption and Mass Transport of Methane and Hydrogen in Nanoporous Carbon Membranes - Binary Mass Transport Experiments and Modeling. *Journal of Membrane Science*

Conference Papers

– M. Kurth, J.-U. Repke, S. K. Bhatia (2024b): Maxwell-Stefan Surface Diffusion Modeling on Nano-Porous Carbon Membranes. *6th Doctoral Colloquium Bioenergy: University of Applied Sciences and Arts. Hildesheim/Holzminden/Göttingen.* Tagungsreader. Leipzig: DBFZ, 32–33. ISBN: 978-3-949807-10-7

– M. Kurth, S. Rönsch (2020): Herstellung, Charakterisierung und Modellierung von wasserselektiven Membranen für die Methanisierung von CO2. *DBFZ Jahrestagung 2020: Leipzig, 16./17. September 2020.* Tagungsreader. Leipzig: DBFZ, 288–289. ISBN: 978-3-946629-61-0

Oral Presentations and Posters Without Proceedings

– M. Kurth (2021): *Water Selective Membranes for CO2 Methanation.* Karlsruhe

– M. Kurth, S. Rönsch, J.-U. Repke (17.-19.02.2020): *Charakterisierung und Modellierung von wasserselektiven Membranen zur Umsatzsteigerung der Methanisierung.* Freising

– M. Kurth, J.-U. Repke, S. Rönsch (04.03.2020): *Herstellung, Charakterisierung und Modellierung von wasserselektiven Membranen zur Umsatzsteigerung der Methanisierung.* Frankfurt

– M. Kurth, J.-U. Repke, S. Rönsch (30.09.-01.10.2019): *Fabrication, characterization and modeling of water selective membranes for methanation reactors.* Nürnberg

– M. Kurth, S. Rönsch (06.03.2019): *Herstellung, Charakterisierung und Modellierung von wasserselektiven Membranen zur Umsatzsteigerung der Methanisierung.* Frankfurt am Main

Supervised Theses

– S. Buba (2019): Herstellung und Charakterisierung wasserdampfselektiver Silicatmembranen mittels Sol-Gel Verfahren zur Umsatzsteigerung der Methanisierung. *mathesis.* Hochschule Emden/Leer

Contents

List of Figures

List of Tables

List of Codes

List of Symbols

Abbreviations

Symbol	Description
BECCS	Bioenergy with Capture and Storage
BET	Brunauer, Emmett and Teller
BVP	Boundary Value Problem
CCS	Carbon Capture and Storage
CCU	Carbon Capture and Utilization
DBFZ	Deutsches Biomasseforschungszentrum gemeinnützige GmbH
dbta	Institute of TU Berlin: Dynamik und Betrieb technischer Anlagen
DFT	Density of functional theory
DGM	Dusty Gas Model
DMSE	Deviation or the root mean square deviation
DoE	Design of Experiments
DR	Dubinin-Radushkevich isotherm
DR	Dubinin-Radushkevich
FFKM	Perfluoroelastomer
GC	Gas chromatography
IAST	Ideal Adsorption Solution Theory
IKTS	Institute for Ceramic Technologies and Systems
IPCC	Intergovernmental Panel on Climate Change
IUPAC	International Union of Pure and Applied Chemistry
MFC	Mass Flow Controller
MMM	Mixed Matrix membranes
MOF	Metal Organic Framework
MS	Maxwell-Stefan
NC	Number of components
NE	Number of Elements

NLDFT	Non-local density functional theory
NLE	Non linear Equation System
PEG	Polyethylene glycol methyl ether
PFA	Furfuryl alcohol
PID	Piping and instrumentation diagram
SNG	Synthetic natural gas
STP	Standard temperature 293.15 K and pressure 101 325 Pa
TC	Temperature Controller
TU	Technical University
UQ	University of Queensland, Brisbane, Australia

Constants

Symbol	Description	Unit
π	3.141 59...	1
e	Euler's number = 2.718 28...	1
R	Universial gas constant = 8.314 46	$\mathrm{J\,mol^{-1}\,K^{-1}}$

Dimensionless Numbers

Symbol	Description	Definition
Kn	Knudsen number	$\lambda_i d_p^{-1}$
Re	Reynolds number	$\frac{wd\rho}{\eta}$

Greek Symbols

Symbol	Description	Unit
$\alpha_{i,j}$	Selectivity of component i over j	–
Δ	Difference	–
δ	Thickness	m
$\delta_{i,j}$	Kronecker delta	
Γ	Thermodynamic correction factor	–
λ	Mean free path	m
μ	Dynamic viscosity	Pa s
∇	Nabla operator	

ϕ	Optimization parameter	–
ρ	Density	$\mathrm{kmol\,m^{-3}}$
σ	Standard deviation	–
σ^{mol}	Size of molecule	m
τ	Turtuosity	–
θ_i	Fractional occupancy of surface	
ε	Porosity	–
ε^{DR}	Dubinin-Radushkevich characteristic energy	–
ζ_i	Confinement factor	–

Indices

Symbol	Description
i	Index for components
j	Index for components

Latin Symbols

Symbol	Description	Unit
$\mathcal{D}^s$	Maxwell-Stefan surface diffusion coefficient	$\mathrm{m\,s^{-2}}$
$\dot{Q}$	Heat	W
$\hat{p}$	mean pressure inside of the pore	Pa or bar
A	Area	$\mathrm{m^2}$
b	Langmuir constant	$\mathrm{bar^{-1}}$
B_0^e	Knudsen parameter	–
c	Concentration	$\mathrm{mol\,m^{-3}}$
D^{Kn}	Knudsen diffusion coefficient	$\mathrm{m\,s^{-2}}$
d_p	Pore diameter	m
F	Flow	$\mathrm{m^3\,s^{-1}}$
f^{toth}	Toth constant	–
h	Hour	3600s
K	Permeability	$\mathrm{mol\,m^{-2}\,s^{-1}\,m^{-1}\,Pa^{-1}}$
K^{fr}	Freundlich constant	–
K^{toth}	Toth constant	–
K_μ	Adsorption constant for Do isotherm	–
K_f	Adsorption constant for Do isotherm	–
K_H	Henry's constant	$\mathrm{mmol\,g^{-1}\,Pa^{-1}}$
L	Liter	$1\mathrm{E}{-3}\mathrm{m}^3$

$L_{i,j}$	Onsager coefficient	60s
min	Minute	60s
N	Diffusive flow	$\mathrm{mol\,m^{-2}\,s^{-1}}$
n	Number of molecules	mol
n^{fr}	Freundlich constant	—
P	Permeance	$\mathrm{mol\,m^{-2}\,bar^{-1}\,s^{-1}}$
p	Pressure	Pa or bar
p^{red}	Reduced pressure	—
p^{TMP}	Transmembrane pressure	bar
P_i^{multi}	Multicomponent i permeance	$\mathrm{mol\,m^{-2}\,bar^{-1}\,s^{-1}}$
P_i^{pure}	Pure component i permeance	$\mathrm{mol\,m^{-2}\,bar^{-1}\,s^{-1}}$
q	Adsorbed amount at surface	$\mathrm{mmol\,g^{-1}}$
$Q_{i,st}$	Isosteric heat of adsorption	$\mathrm{J\,mol^{-1}}$
R^2	squared correlation coefficient	—
S	Separation factor	—
S_0	Concentration of functional groups for Do isotherm	$\mathrm{mol\,g^{-3}}$
S_{BET}	BET specific Surface Area	$\mathrm{m^2\,g^{-1}}$
T	Temperature	°C or K
u	Mean velocity of molecule	$\mathrm{m\,s^{-1}}$
V	Volume	$\mathrm{m^3}$
v	Volume	$\mathrm{m^3}$
V_{mic}	Specific micropore volume	$\mathrm{m^3\,g^{-1}}$
V_T	Total specific volume	$\mathrm{m^3\,g^{-1}}$
v_T	Mean thermal velocity of molecule	$\mathrm{m\,s^{-1}}$
w	Probability factor	—
x	Mole fractions	$\mathrm{mol\,mol^{-1}}$
z	Spatial coordinate	m

Superscripts

Symbol	Description
$conf$	Confined space
$conv$	Convective term
$feed$	Feed side
II	Second pseudo interface
I	First pseudo interface
Kn	Knudsen term
LV	Vapor Liquid equilibrium
mem	Membrane
$multi$	Multicomponent

$_{perm}$	Permeate side
$_{pure}$	Single component/Pure
$_{T}$	Temperature corrected

Subscripts

Symbol	Description
$_{i}$	Component i
$_{j}$	Component j
$_{k}$	Component k
$_{T}$	Total amount

1 Introduction

This introduction frames the study within its background, outlines its objectives, and summarizes the modeling approach.

1.1 Background and context

Driven by climate change, largely caused by the burning of fossil fuels since the Industrial Revolution, the international community has set ambitious goals for climate neutrality. These targets aim to limit global warming to no more than 2 °C by mid-century.

To transition from fossil dependence, future energy systems must become more flexible; one approach involves using alternative resources like biogenic feedstocks to produce hydrocarbons as platform chemicals or energy carriers (Kaltschmitt, 2019).

In this context, biogenic CO_2 becomes a renewable feedstock for the synthesis of fuels and chemicals, especially when coupled with hydrogenation reactions using green hydrogen.

One prominent example is CO_2 methanation, where renewable methane (CH_4) is produced with advantages in storage and infrastructure compatibility over H_2 and the existing numerous use-cases for methane (see (Ghaib et al., 2016; Rönsch et al., 2016; Walspurger et al., 2014)). Although the current low price of natural gas limits the economic viability of CO_2 methanation, this barrier may diminish as market conditions evolve, compare (Ashok et al., 2020; Ullah et al., 2023). As such, methanation remains a promising pathway for integrating captured CO_2 into the energy system, particularly when coupled with renewable hydrogen.

Another example is thermochemical gasification, which offers a flexible route to generate hydrogen-rich syngas from alternative feedstocks at up to 900 °C, see (Kaltschmitt, 2019). This syngas, composed mainly of H_2 and CO, can be used directly or upgraded via catalytic processes. Its composition depends on feedstock, reactor type, and gasification agent, see (Karellas, 2015).

To enable efficient conversion and separation in such processes, membranes offer a robust and scalable solution (Melin and Rautenbach, 2007). In addition to simplifying downstream processing, membranes can enhance product quality by selectively separating fuels and chemicals from the reaction mixture, reducing contaminants and increasing purity. This not only improves the value of the final products but also protects downstream catalysts from degradation, extending their operational lifetime. When integrated directly into the reaction zone, membranes in membrane-reactors can increase overall conversion, while selective removal and recycling of unreacted educts further improve efficiency and product concentration (Figoli et al., 2016; Melin and Rautenbach, 2007; Nazely Diban and Ortiz, 2013; Schlereth and Hinrichsen, 2014; Tsuru et al., 2008). Carbon based nanoporous membranes offer thermal and chemical stability, which allows operation under harsh conditions, aligning with optimal reaction parameters. These membranes are particularly suited for high-temperature applications involving selective separation of H_2, CH_4, and H_2O, such as in hydrogen purification, steam reforming, and synthetic fuel production. Given the complexity of product gas mixtures and the need for extensive downstream purification—often involving energy-intensive cooling, compression, and multi-stage separation—carbon-based membranes provide a compact and integrated alternative. By enabling in situ separation under reaction conditions, they simplify process design, reduce energy demand, and enhance overall system efficiency.

Integrating membranes into thermochemical reaction and gas separation processes can improve technical performance and economic viability, supporting the shift toward renewable carbon sources and thus contribute to climate change mitigation.

At present, the mass transport properties of carbon based nanoporous membranes and their potential for application have not yet been fully characterized. A more profound understanding of the process parameters and their interaction with other gases could help to adapt further applications of carbon-based membranes in hydrogenation or high temperature processes. Through comprehensive experimental char-

acterization, a mass transport model could enable the implementation of nanoporous carbon membranes in process simulation software, thereby simplifying the execution of feasibility studies.

The present work contributes to this effort by experimentally characterizing a nanoporous carbon-based membrane and developing a binary mass transport model for high-temperature gas separation.

1.2 Research objectives

The present thesis seeks to deepen the understanding of multicomponent mass transport phenomena involving gases and vapors through nanoporous carbon membranes at elevated temperatures. By combining experimental characterization and validation with advanced modeling techniques, the present research helps understanding the permeation characteristics of the tested nanoporous membrane.

In order to systematically explore this research question, the following hypotheses are proposed:

Hypothesis 1 Maxwell-Stefan surface diffusion coefficients can be calculated from experimental data and applied in a binary mass transport model that is capable of predicting binary permeation measurements.

Hypothesis 2 The accuracy of the calculated Maxwell-Stefan surface diffusion coefficients, which are subject to uncertainty due to temperature extrapolation, can be significantly improved by applying a simple temperature-dependent correction function.

1.3 Methodology

The described hypothesis are answered with the following methodology. Through a combined experimental and theoretical approach, a valuable database of high temperature adsorption and permeation data will be generated. In addition a methodology

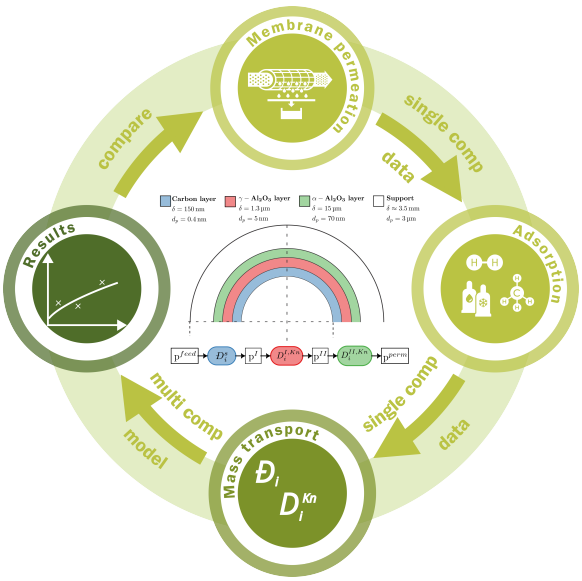

Fig. 1.1: The organisation of this thesis combining pure component experimental data to develop a multi component mass transport model (Kurth et al., 2024a).

to develop a binary mass transport model based on single component measurements is presented.

The methodology can be broken down into four distinct steps described in fig. 1.1:

1) Obtaining data for adsorption and permeation of the three individual components within the membrane system.

2) Calculation of the diffusion coefficients for each component within the membrane. These coefficients quantify the rate of molecular movement under a concentration gradient and are essential parameters for developing an accurate mass transport model.

3) The binary mass transport model that incorporates the collected data and calculated diffusion coefficients is developed. This model is capable of predicting the separation behavior of the components under various operating conditions.

4) To validate the accuracy of the model and to assess its predictive capabilities, we will perform a comprehensive comparison with experimental data obtained.

Based on the literature review (chapter 2), the first step was to perform single gas adsorption experiments at temperatures up to 110 °C and permeation trials with a sample of a membrane at temperatures from 120 °C to 220 °C. Different adsorption isotherm models were used to analyze the data. These models may include simplifications to describe the complex interactions between the gas molecules and the membrane surface. The results of these analyses, along with calculated diffusion coefficients, were then used to develop a binary mass transport model capable of predicting separation behavior for two-component gas mixtures. Finally, ternary experiments with three-component mixtures were conducted. After validation, the model was used to predict separation behavior for gas compositions relevant to industrial processes. This comprehensive approach provided an in-depth understanding of mass transport across the membrane, while recognizing the potential limitations associated with isothermal simplifications and the necessary temperature extrapolations.

The thesis is organized in six chapters. The introduction (chapter 1) is followed by a literature review (chapter 2), which explores the physics of adsorption in nanoporous membranes, identifies gaps in understanding, and establishes modeling approaches. The methods chapter (chapter 3) describes experimental and theoretical techniques. The theoretical and practical modeling approach is presented, and the simplifications and assumptions are shown. The outcome is presented in the results chapter (chapter 4) and then used to understand the development of the binary mass transport model and its limitations. The modeling results are then compared with the binary permeation experiments. Based on a parameter variation, the model is then used to understand the applicability of the analyzed membrane for use in industrial applications. The discussion (chapter 5) analyzes the results, considering their significance and limitations. Finally, the thesis concludes (chapter 6) by summarizing the achievements and providing an outlook for future research directions.

2 Literature review

This chapter summarizes the available literature and contextualizes the present work. It discusses the various types of membranes and the applications in this context, the different approaches to describe mass transport, and the required adsorption isotherms for the approach used in this work.

2.1 Introduction

Gas separation plays a critical role in many industrial separating processes and environmental applications, compare (Kraume, 2020). Traditional separation techniques, while effective, often have inherent limitations such as high energy consumption and environmental concerns. For instance condensation works by cooling a gas mixture to a temperature where specific components condense into liquid; however, it requires significant energy input, which can be inefficient and costly, especially for large-scale operations. Adsorption relies on the capacity of solid materials to capture gas molecules through surface interactions; this process can be limited by the adsorbent's surface area and regeneration challenges. The need for periodic regeneration can result in downtime and increased operational complexity. Chemical absorption captures specific gases in a liquid solvent through chemical reactions; this can lead to issues such as solvent degradation and the need for extensive solvent management, complicating the process and resulting in high operational costs, compare (Kohl and Nielsen, 1997; Kraume, 2020; Poling et al., 2001).

Membrane-based gas separation is a promising alternative, offering advantages in terms of energy efficiency, compactness, and scalability due to their continuous operation and the absence of phase changes. The method used in this work is based on basic understanding of diffusion theory and is based on the adsorption behavior

of pure gases on solids, which is introduced as well. The following section briefly introduces the family of gas separation membranes and touches the basic principle of membrane separation.

2.2 Gas separating membranes

Gas-separating membranes are classified as either organic or inorganic, and each type contains both symmetric and asymmetric membranes. These types differ in application and membrane structure, which defines the dominant separation mechanism.

Organic membranes are typically composed of polymeric materials and are widely used in various applications due to their flexibility, ease of processing, and cost-effectiveness. They are suitable for applications such as water treatment, gas separation at mild conditions, and pervaporation. However, organic membranes may suffer from limitations such as thermal and chemical instability, which can lead to degradation under harsh operating conditions, compare (Kohl and Nielsen, 1997; Melin and Rautenbach, 2007; Scott, 1995). These conditions can be described by elevated temperatures, high pressures or harsh chemical conditions like an extreme pH-value, impurities or reactive gases.

In contrast, inorganic membranes, such as those made from ceramics or zeolites, often require high-temperature processing methods, such as sol-gel synthesis, or sintering of particulate materials, compare (Briceño et al., 2012b; Brinker and Scherer, 2013). These methods can yield either symmetric, monolithic structures, in which the entire membrane is uniformly porous, or asymmetric structures, in which a thin, selective inorganic layer is deposited onto a preformed, porous support. A mixture of organic and inorganic membranes are Mixed Matrix Membranes, where a polymeric filler is mixed with high porous Metal-Organic Frameworks to enhance the performance of the membranes.

2.2.1 Possible applications of membrane gas separation

As indicated above, a large share of today's membrane technology relies on synthetic polymer membranes. The increasing demand for clean energy and efficient resource use drives the need for advancements in gas separation technology. Below are various applications of membrane gas separation, highlighting scenarios where in-situ or downstream gas separation can be beneficial and thus harsh conditions are present.

Carbon Dioxide methanation CO_2 methanation is a catalytic process that converts carbon dioxide (CO_2) and hydrogen (H_2) into methane (CH_4) and water (H_2O).

The exploration of methane production through CO_2 methanation is gaining significant attention as a promising alternative for sustainable energy storage (compare (Nieß et al., 2022; Rönsch et al., 2016)). Biorefineries, which are designed to utilize diverse biomass feedstocks for the production of biofuels and biochemicals, can integrate CO_2 methanation into their processes to improve overall sustainability (Kaltschmitt, 2019). By utilizing carbon dioxide-rich gases produced during biorefinery operations, this process not only reduces greenhouse gas emissions but also facilitates the conversion of waste streams into valuable energy resources (Kaltschmitt, 2019; Rönsch et al., 2016).

Implementing a membrane reactor system can increase turnover and improve the economic feasibility of biorefinery systems. Similar to intercooling steps that remove water content, the application of membranes would achieve this without the need to cool down the gas stream. Additionally, a membrane system could be applied in the intercooling steps of the cascading reactor, selectively removing water without condensation and minimizing energy dissipation.

Thermochemical gasification Similar to CO_2 methanation, thermochemical gasification offers a promising path to utilize carbon sources to produce chemicals or fuels. Gasification employs solid feedstocks such as coal or organic wastes, converting them into a gaseous mixture primarily composed of H_2, CO, CH_4, H_2O and CO_2,(Kaltschmitt, 2019; Kiendl et al., 2014; Klemm, 2005). A significant challenge in gasification is the generation of tar and ash, which can hinder the economic feasibility of certain technologies, compare (Ahlström et al., 2022).

Tab. 2.1: Syngas composition of steam/O_2 gasification of woody biomass on wet and dry basis (Kaltschmitt, 2019; Kaur et al., 2023; Thunman et al., 2019).

Component mol %	Dry composition mol %	Wet composition
H2	10-30	5-15
CO	20-40	10-20
CO2	15-25	7.5-12.5
CH4	1-12	0.5-2.5
H2O	0	20-50

Various gases can serve as gasification agents, with air (containing mostly N_2 and O_2) being the most commonly used, resulting in a product gas that predominantly consists of N_2. A more recent advancement involves using water vapor mixed with O_2 as a gasification agent, which yields a product gas with a higher calorific value. The gasification process typically operates at temperatures up to 900 °C and at atmospheric pressure or up to 100 bar, compare (Klemm, 2005). The reactor involves three main reaction steps, which can occur simultaneously or in separate reactors.

The composition of the wet and dry gas of the product gas is shown in table 2.1 and depends on the process conditions and the reactor type, which may also affect the composition. The composition of the feedstock determines the composition of the produced syngas, here woody biomass was used as a feedstock.

Highly stable inorganic porous membranes, which demonstrate superior thermal and chemical stability compared to organic alternatives, are particularly advantageous in gas separation processes where harsh operating conditions and limited plant size necessitate process intensification. This approach not only enhances separation efficiency but also improves economic feasibility, compare (Kaltschmitt, 2019; Rönsch et al., 2016). Consequently, this work will focus on inorganic porous gas separation membranes.

2.2.2 Basic terminology of membrane separation

The basic principle of membrane separation is introduced in fig. 2.1. The *Feed* gas is fed into one side of the membrane, resulting in two distinct streams: the *Permeate*, which consists of the gases that passed through the membrane, and the *Retentate*,

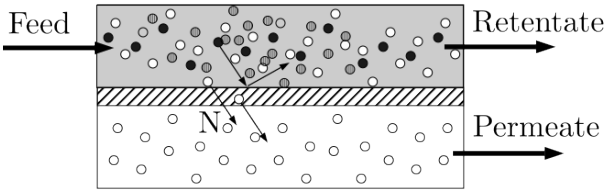

Fig. 2.1: Principle of membrane separation, according a figure from (Melin and Rautenbach, 2007). Only one species in the feed is transported through the separation layer resulting in a concentrated permeate and a diluted retentate stream.

which contains the remaining gases that did not permeate. The flow through the membrane layer N_i (compare eq. (2.1)) refers to the movement of gas molecules through the membrane layer as a product of the driving force and the ability of the molecule to pass through the membrane layer. The driving force of the flow can be described in terms of chemical potential μ_i, concentration c_i or partial pressure difference Δp_i, compare (Nagy, 2018) and section 2.3 for more details. The partial pressure difference Δp_i is also called *transmembrane pressure* or p_i^{TMP}.

$$N_i = P_i \cdot A^{mem} \cdot \Delta p_i \tag{2.1}$$

$$K_i = \frac{P_i}{\delta} \tag{2.2}$$

Although often used interchangeably, permeance P_i and permeability K_i have different dimensions (Melin and Rautenbach, 2007). Permeance quantifies the intrinsic ease with which a gas passes through a membrane material itself. It is expressed as the volume of gas that permeates per unit time, per unit area of membrane and per unit pressure difference across the membrane (compare eq. (2.1)).

Permeability takes into account the thickness of the membrane. It represents the combined effect of permeance and the resistance of the membrane to flow due to its thickness δ. The permeability K_i is a characterization parameter of a material rather than a membrane (compare eq. (2.2)).

In the case of nanoporous carbon membranes, the permeance P_i is the more applicable term, since the separation effect is not linear dependent on the thickness of the layer. The effect takes place because of specific deposition effects of the molecule on the surface.

Selectivity $\alpha_{i,j}$ refers to the ability of a membrane to preferentially pass certain gas molecules over others, as described in eq. (2.3), definition taken from (Melin and Rautenbach, 2007). Selectivity is often compared to the separation factor $S_{i,j}$ (see eq. (2.4)), which is the ratio of the permeance of the desired component (i) to the permeance of the undesired component (j). A higher separation factor indicates a greater preference for the component to pass through the membrane. In this context the selectivity $\alpha_{i,j}$ is measured, while the separation factor compares the multicomponent P_i permeances in the mixture to each other.

In multicomponent mass transport, the separation of components is often initially estimated by comparing the pure component permeances eq. (2.5) and assuming a similar behavior in the multicomponent case, see (Weyd et al., 2008).

In this work, the separation factor $S_{i,j}$ is compared to the ratio of pure component permeances P_i^{pure}/P_j^{pure} to emphasize the differences between pure and multicomponent experiments.

$$\alpha_{i,j} = \frac{x_i^{perm}/x_j^{perm}}{x_i^{feed}/x_j^{feed}} \tag{2.3}$$

$$S_{i,j} = \frac{P_i}{P_j} \tag{2.4}$$

$$P_i^{pure}/P_j^{pure} \tag{2.5}$$

While selectivity $\alpha_{i,j}$ is more commonly associated with experimental values, the comparison between multi- and pure-component permeance is more straightforward.

2.2.3 Inorganic porous gas separation membranes

Inorganic porous membranes have become well-established in specific micro- and ultrafiltration applications (Cardoso et al., 2018; Marcano and Tsotsis, 2002; Melin and Rautenbach, 2007; Ohya et al., 1997).

Compared to polymeric membranes, inorganic membranes offer several key advantages like enhanced temperature and chemical resistance, compare (Melin and Rautenbach, 2007). While inorganic membranes have carved out a market niches due to their advantages, particularly in reaction technology, they also have limitations compared to polymeric materials, see (Saracco et al., 1999; Scott, 1995). Due to the brittleness and thermal expansion the handling of such membrane systems requires a high degree of experience and caution. The manufacturing process requires multiple complex steps and is not easy to be scaled up to higher production scales, compare (Melin and Rautenbach, 2007; Richter et al., 2017).

Within the field of membrane-based gas separation, nanoporous carbon membranes have received considerable attention due to their unique properties (Briceño et al., 2012a; Richter et al., 2017). These membranes exhibit exceptional selectivity for specific gas species, making them particularly attractive for applications such as CO_2 capture or H_2 purification (Melin and Rautenbach, 2007).

Carbon membranes generally have a macro porous support, an intermediate layer and a small porous top layer. Various membrane surface modification techniques have been researched in the past years, in order to improve the selectivity even further. The current research focuses on materials that exhibit molecular sieving properties, such as silica, zeolites, MOFs (metal-organic frameworks), graphene and carbon, compare (De Meis et al., 2018; Monsalve-Bravo et al., 2023; Monsalve-Bravo and Bhatia, 2018; Monsalve-Bravo et al., 2024).

Types of inorganic porous membranes Inorganic membranes have higher permeance, selectivity, and better resistance to higher pressure and temperature compared to polymeric membranes. The main materials used for porous inorganic membranes are alumina (Al_2O_3), silica (SiO_2), zirconia (ZrO_2), zeolite and carbon. Ceramics are compounds of metallic and non-metallic elements. They generally have a macro porous support, an intermediate layer and a small porous top layer. Because the

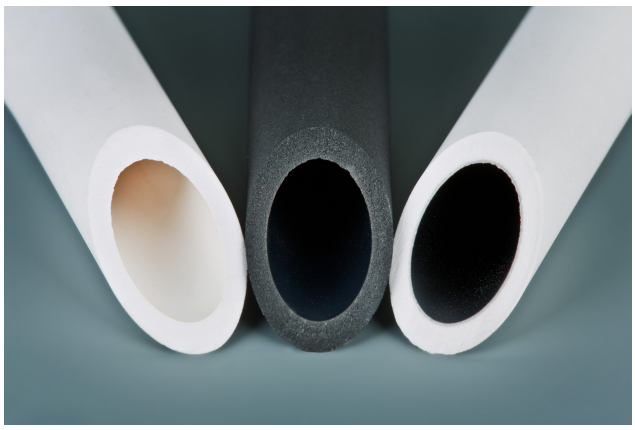

Fig. 2.2: Examples of cylindrical inorganic carbon membranes used for gas separation. **left:** uncoated ceramic support, **middle:** solid carbon membrane and **right:** inner coated carbon membrane Photo by Fraunhofer IKTS.

Knudsen gas separation regime has a very low selectivity (Melin and Rautenbach, 2007), various membrane surface modification techniques have been researched in the past years. The research focuses on materials that exhibit molecular sieving properties, such as silica, zeolites, MOFs (metal-organic frameworks), graphene and carbon (De Meis et al., 2018). In the following subsections the general mass transport principles are introduced and the different modeling approaches are introduced.

Symmetric porous membranes can be used as supports for finer membrane structures, but have also become important as microfiltration membranes.

According to the IUPAC nomenclature, inorganic membranes are divided into micro ($d_p < 2\,\text{nm}$), meso ($2\,\text{nm} \leq d_p \leq 50\,\text{nm}$) and macroporous ($d_p > 50\,\text{nm}$) structures (compare Do, 1998, p. 2). Different applications require not only different pore sizes, but also different shapes of the membrane, support and module. For laboratory applications in material development, disc or tube shaped supports are often used. In industrial processes, multi-channel elements, honeycomb structures or, more recently, inorganic hollow fibers are preferred (Kämnitz et al., 2022; Melin and Rautenbach, 2007; Richter et al., 2017; Simon et al., 2015; Weyd et al., 2008).

This work focuses on an asymmetrical membrane composed of a nanoporous carbon layer on the inside of a ceramic Al_2O_3 support. Such a membrane is illustrated in fig. 2.2 on the right-hand side, where the carbon layer is visible within the sup-

port. The membrane is produced by *Fraunhofer IKTS Hermsdorf*, and the synthesis process, structure, and experiments are thoroughly described in chapter 3.

Carbon membranes offer high selectivity for specific gases, such as CO_2, due to their tunable pore size and surface chemistry. They exhibit superior thermal stability, making them suitable for harsh environments and high-temperature operations. Some carbon membranes exhibit excellent chemical resistance, making them suitable for handling corrosive substances (Ismail et al., 2011). In addition, they tend to be more durable than polymer membranes, potentially resulting in longer service life (Ismail et al., 2011; Richter et al., 2017). Carbon membranes can be complex and expensive to manufacture, limiting their scalability for large-scale production. Sensitivity to oxidizing environments can degrade their performance and limit their applications.

In the following section the mass transport principles which are present in porous inorganic membranes are presented and discussed.

2.3 Mass transport of gases through a membrane layer

This section first describes the basic diffusion through membranes, then narrows the focus to specific mechanisms in porous membrane layers.

2.3.1 Diffusion

The fundamental principle of gas diffusion through membranes relies on the difference in permeance of the components, allowing certain components to pass more easily while hindering others. The selectivity $\alpha_{i,j}$ is influenced by factors such as molecular size, diffusivity, and solubility (or adsorption) in the membrane material.

The driving force for gas flow of the component i, N_i across the membrane is primarily the chemical potential gradient $\nabla\mu$, which can be rewritten regarding the pressure or concentration gradient over the membrane, ∇p_i or ∇c_i, respectively. With R as the universal gas constant in $\mathrm{J\,mol^{-1}\,K^{-1}}$ and T as the temperature in K and D_i as the *Fick* diffusion coefficient in $\mathrm{m^2\,s^{-1}}$.

$$N_i = -\frac{D_i c_i}{RT} \cdot \nabla \mu_i \tag{2.6}$$

With the differential for the chemical potential

$$\mu = \mu^0(T) + RT \ln\left(\frac{p_i}{p_i^0}\right) \tag{2.7}$$

and the definition of concentration of an ideal gas

$$c_i = \frac{n}{v} = \frac{p_i}{RT} \tag{2.8}$$

this can be rewritten as:

$$N_i = -D_i \cdot \frac{1}{RT} \nabla p \tag{2.9}$$

The *Fick* diffusion model is capable of describing the diffusion of single components through a homogenous material like a gas through air, liquids in a solution or gases in polymeric material, where free molecular diffusion is the primary mass transport mechanism, compare (Melin and Rautenbach, 2007) and see fig. 2.4. However, using nanoporous membranes the interactions between the molecules and the pore walls are not negligible, since the Van der Waals forces from the pore walls are stronger. This necessitates describing the interactions between the different components and the membrane walls and surface, where pore diffusion, molecular adsorption and surface diffusion are predominant in describing the mass transport.

As can be seen on fig. 2.1 the membrane used in this work consists of different layers, where a different mode of diffusion is necessary to describe the mass transport.

2.3.2 Diffusion in porous media

As can be seen in fig. 2.4 the mass transport description needs to be adapted depending on the pore size d_p of the porous membrane. For smaller pore diameters d_p and based on the mean free path of the molecules, the molecule-wall interactions become more and more important.

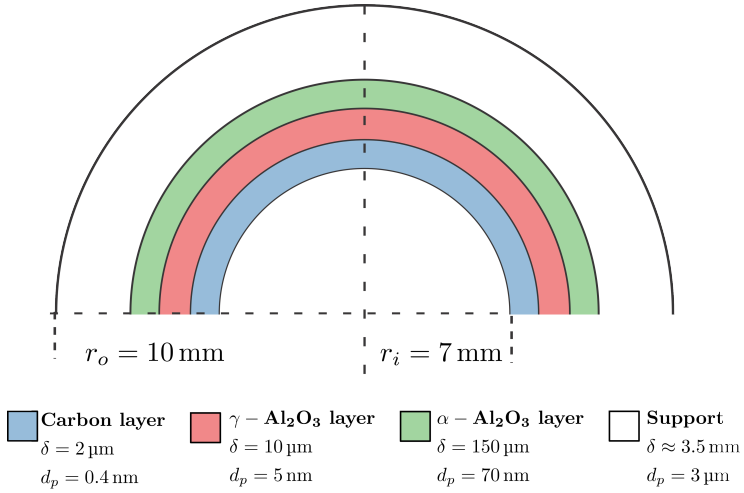

Fig. 2.3: The different layers described in this work. One carbon layer with a nanoporous pore size is supported by two macro-porous layers, where the mass transport principle is different.

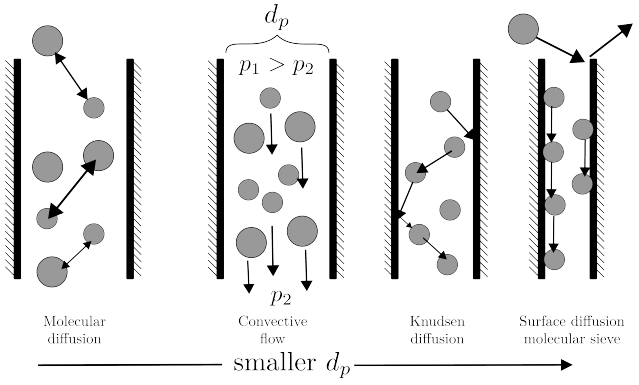

Fig. 2.4: Different modes of molecular transport in porous media with the wall-molecule interactions as parameter. Idea from (Melin and Rautenbach, 2007).

The mean free path of a molecule (λ_i) can be described by eq. (2.10), where λ_i is the mean free path in m, k_B is the Boltzmann constant ($k_B = 1.34 \times 10^{-23}\,\mathrm{J\,K^{-1}}$), T is the temperature in K, $\hat{p_i}$ is the mean pressure inside the pore in Pa, and σ^{mol} is the size of the transported species' molecules in m.

$$\lambda_i = \frac{k_B T}{\sqrt{2}\pi \hat{p_i} (\sigma^{mol})^2} \tag{2.10}$$

The relationship between the mean free path and the pore diameter, d_p is called the *Knudsen number* (Kn).

$$Kn_i = \frac{\lambda_i}{d_p} = \frac{k_B T}{\sqrt{2}\pi (\sigma^{mol})^2 \hat{p_i} d_p} \tag{2.11}$$

When the pore size is much larger than the mean free path, the dominant mode of transport is the molecular diffusion, where a free exchange of potential is possible and the molecule-wall interaction can be neglected. When a pressure gradient is present in the transport layer of the membrane the flow can even be described using convective flow describable with the Hagen-Poiseuille equation eq. (2.12), where ε, τ and μ are the porosity, the tortuosity and the dynamic viscosity in Pa s, respectively.

Since this mode of transport is not apparent in the used nanoporous carbon membrane, the theory will not be described further.

$$N_i^{conv} = -\frac{p_i}{RT} \frac{\varepsilon d_p^2}{\tau 32 \mu} \frac{dp_i}{dz} \tag{2.12}$$

When decreasing the pore size, the molecule-pore interactions become important and thus the mass transport needs to be described using *Knudsen diffusion* which is done in section 2.3.3, where the Knudsen number is much larger than unity

$Kn \gg 1$ (Nagy, 2018). The Knudsen diffusion approach is needed for porous nano- or ultrafiltration membranes and is discussed in detail in section 2.3.3.

When the pore size is even smaller, the molecule-wall interaction is the dominant force of mass transport in such narrow pores and thus can be described using a description of the surface diffusion. Describing the surface diffusion the *Maxwell-Stefan surface diffusion* is the approach used in this context and is described in section 2.3.4.

2.3.3 Knudsen diffusion

If the Knudsen number Kn is in the range of $0.1 \leqslant Kn \leqslant 10$, e.g. the mean free path (λ_i) of the molecule is in the same order of magnitude as the pore diameter, the Knudsen flow is dominant. If the pore size becomes even smaller (Nagy, 2018), e.g. for micropores ($dp < 2\,\mathrm{nm}$), the force field inside the pore replaces the molecules, leading to diffusion as an activated process, either by activated gas diffusion or by surface diffusion if the interaction potential is strong enough. Different approaches can be used to describe these different diffusion processes (Krishna, 1990; Melin and Rautenbach, 2007; Nagy, 2018) and a well known approach is the use of the *dusty gas model* (DGM), see (Das, 2019). The DGM is used in several publications, but in recent years has been shown to be somewhat erroneous for pores smaller than 2 nm due to the misleading thermodynamic basis, see (K. Bhatia et al., 2011).

When mass transport is described by *Knudsen diffusion*, the mean free path significantly exceeds the diameter of the channel containing the diffusing molecules. The Knudsen number serves as the parameter describing the conditions that favor this mode of transport, compare (Knudsen, 1909). Based on these assumptions, the description of Knudsen diffusion N^{Kn} is a probabilistic description and thus can be described by a probabilistic factor w, the density of the molecules ρ in $\mathrm{mol\,m^{-3}}$ and the mean thermal velocity of each molecule v_T in $\mathrm{m\,s^{-1}}$ (see eq. (2.13)) (Do, 1998).

$$N^{Kn} = w\rho v_T \tag{2.13}$$

$$w = \frac{1}{4}\frac{1}{1 + 3\delta/(4d_p)} \tag{2.14}$$

The probability factor w is depending on the geometry of the system and thus needs to be exchanged when dealing with another pore structure. Dealing with cylindrical capillary structures w can be written as mentioned in eq. (2.14).

Often the *Knudsen diffusion* get simplified using the case for long straight capillary (where $\delta \gg 10d_p$ (Do, 1998)) and based on this assumption one can follow, that the Knudsen diffusion coefficient D_i^{Kn} can be described using eq. (2.15). When computing the Knudsen diffusion coefficient in this way, the flow N^{Kn} for a pure component can be described using eq. (2.16).

$$D_i^{Kn} = \frac{d_p}{3}\sqrt{\frac{8RT}{\pi\tilde{M}_i}} \tag{2.15}$$

Using this diffusion coefficient the flow can be described:

$$N^{Kn} = -D^{Kn}\frac{1}{RT}\frac{dp}{dz} \tag{2.16}$$

We can follow, that based on this assumption the Knudsen diffusion is applicable for a certain range of pore sizes d_p and for a certain range of layer thickness δ, which might not be applicable to all circumstances. Thus, when dealing with a thin carbon layer with a pore size below 1 nm, the Knudsen diffusion might not be applicable and thus a different approach is needed. This is based on the same argumentation as the limitations of the *DGM* mentioned above and as seen in (K. Bhatia et al., 2011).

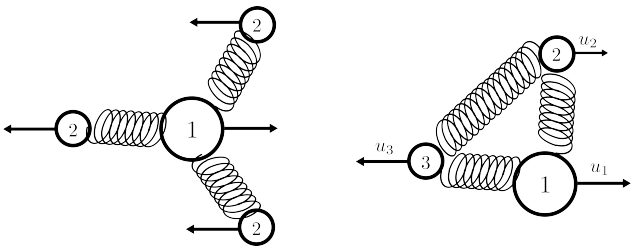

Fig. 2.5: Demonstration of the frictional interactions among moving molecules in the Maxwell—Stefan transport model, depicted for both the two-component scenario (**left**) and the three-component transport scenario (**right**). Adapted from (Nagy, 2018).

2.3.4 The Maxwell—Stefan surface diffusion

The application of surface diffusion can be seen in fig. 2.4 on the right hand side, where the pore walls are much smaller than the mean free path (eq. (2.10)) of the molecules and the wall-molecule interaction is dominant. The generalized Maxwell—Stefan equations operate under the assumption that the motion of species results from a driving force, counteracted by the friction encountered among the moving species and their surroundings (Krishna and van Baten, 2008, 2009; Krishna, 2019). In fig. 2.5, the schematic representation illustrates the hindering effect of the friction force on the species' movement. The equation's generalized form is then applied to multicomponent fluid mixtures which is shown in eq. (2.17), where μ_i, $\mathcal{D}_i^s$ and u are the chemical potential, the Maxwell—Stefan surface diffusion coefficient and the molecules mean velocity, respectively. Since the model describes the effect of the friction of different molecules, this multi component description is needed for the description of a binary system.

$$-\frac{\nabla\mu_i}{RT} = \sum_{j=1,j\neq i}^{NC} \frac{x_j(u_i - u_j)}{\mathcal{D}_{ij}} \tag{2.17}$$

The gradient of the thermodynamic potential $\nabla\mu_i$ can be represented using mole fraction x_i gradients, partial pressures or, alternatively, in terms of the gradients of the surface fractional occupancies $\nabla\theta_i$, when dealing with the description of an adsorbed species.

The Maxwell—Stefan diffusion can be used in different contexts, where a multi-component description of the mass transport is necessary. When dealing with surface diffusion in a narrow pore network, the mole fraction (x_i) is replaced with the fractional occupancy θ_i, which is described by eq. (2.18), where q_i is the surface concentration of the species i in $\mathrm{mmol\,g^{-1}}$.

$$\theta_i = \frac{q_i}{\sum_i^{NC} q_i} \tag{2.18}$$

This leads to the description of eq. (2.17) in terms of θ_i in eq. (2.19). When dealing with a multi component description of in the context of Knudsen diffusion the adsorbed concentration can be replaced with the total concentration c_T.

$$q_T \frac{x_i}{RT} \nabla \mu_i = \sum_{j=1, i \neq j}^{NC} \frac{q_j N_i - q_i N_j}{q_T \mathcal{D}_{i,j}^s} + \frac{N_i}{\mathcal{D}_i^s} \tag{2.19}$$

The μ_i can be described using chemical activity with the use of the thermodynamic correction factor:

$$\frac{x_i}{RT} \nabla \mu_i = \sum_{j=1}^{j=n-1} \Gamma_{i,j} \nabla x_i \tag{2.20}$$

With the kronecker delta δ:

$$\Gamma_{ij} = \delta_{ij} + x_i \frac{d \ln \gamma_i}{dx_j} \tag{2.21}$$

When dealing with ideal solutions the relation of the activity γ_i to the molar fraction x_i is not existent and thus:

$$\Gamma_i = 1 \tag{2.22}$$

Developing a multi component description for the gas phase, the system can be developed for the Knudsen diffusion:

$$-\frac{c_T}{RT}\frac{d\mu_i}{dz} = \sum_{j=1,i\neq j}^{n}\frac{x_i N_j - x_j N_i}{D_{ij}^{Kn}} + \frac{N_i}{D_i^{Kn}} \tag{2.23}$$

with the ideal gas law following:

$$c_T = \frac{n}{v} = \frac{p}{RT} \tag{2.24}$$

$$-\frac{p}{(RT)^2}\frac{d\mu_i}{dz} = \sum_{j=1,i\neq j}^{n}\frac{x_i N_j - x_j N_i}{D_{ij}^{Kn}} + \frac{N_i}{D_i^{Kn}} \tag{2.25}$$

For the multi component approach the binary interaction parameters $\mathcal{D}_{i,j}^{s}$ or D_{ij}^{Kn} are needed. These are crucial in predicting multicomponent mass transport and cannot be measured directly (Nagy, 2018). Its value can be estimated from experimental data or calculated from a logarithmic average of single component Maxwell-Stefan diffusivities based on (Krishna and Baur, 2003). This approach is known as the *Vignes method* (Nagy, 2018) and is shown in eq. (2.26) for the adsorbed concentration and in eq. (2.27) for the bulk gas phase.

For the carbon layer with adsorbed concentrations from (Nagy, 2018):

$$\mathcal{D}_{i,j}^{s} = (\mathcal{D}_i^{s})^{\theta_i/(\theta_i+\theta_j)}(\mathcal{D}_j^{s})^{\theta_j/(\theta_i+\theta_j)} \tag{2.26}$$

For the two support layers with gas phase partial pressures:

$$D_{ij}^{Kn} = (D_i^{Kn})^{p_i/(p_i+p_j)}(D_j^{Kn})^{p_j/p_i+p_j} \tag{2.27}$$

2.3.5 Multi component mass transport

Modeling permeance through membranes is simplified in the case of single components. Here, a well-defined driving force results in molecular movement across the membrane, allowing for relatively simple models based on diffusion and solubility.

Binary or ternary mixtures, however, introduce complexity. Competition for space, interactions between components, and deviations from ideal gas behavior require multicomponent diffusion models and activity coefficients to account for these factors. As a result, modeling permeance in mixtures becomes significantly more complicated than in single component scenarios.

This is the reason why a comparision between the pure and the multicomponent permeance of a component is worthwhile to gather understanding about the effects of one component onto the other. In this work this is done by calculating the ratio of pure permeances, compare eq. (2.5).

Other approaches are discussed in the literature, such as the *Flory — Huggins'* theory, where the multicomponent mixture is described by the entropy of mixing. This is important, but not the main focus of the description in the context of surface diffusion, see (Nagy, 2018).

2.3.6 Gap in the literature

Many of the models currently under development rely on molecular simulation, which can be linked to a theoretical database similar to the one mentioned above (M. Monsalve Bravo, 2016; Monsalve-Bravo et al., 2024). In contrast, a modeling approach utilizing Maxwell—Stefan surface diffusion allows for the incorporation of real experimental data and is able to enhance the model's applicability. This approach is particularly relevant for carbon membrane layers, which offer numerous advantages. Several publications have explored this method for binary mixtures (Cardoso et al., 2018; Monsalve-Bravo et al., 2024), based on either simulation or literature data. To calculate the Maxwell—Stefan surface diffusion coefficient $\mathcal{D}_i^s$ single and multicomponent permeation experiments are essential. Thus, the Maxwell—Stefan approach provides a more comprehensive framework that includes real-world experiments for binary systems, which is currently missing in the literature. As mentioned earlier, in addition to the mass transport experiments through nanoporous membranes, the adsorption of components on the membrane material is crucial for developing a comprehensive model. Specifically, for the mass transport description based on Maxwell—Stefan surface diffusion, understanding the adsorbed phase is essential.

Therefore, the following section will describe the theory and physics of adsorption on solids and will introduce the used adsorption isotherms.

2.4 Adsorption

The adsorption of gases and vapors on porous carbon materials can be described by adsorption isotherms, where under constant temperature the adsorbed amount q_i in $\mathrm{mol\,g^{-1}}$ of i is measured against an increasing partial pressure of the component p_i in bar. Various theories are used to develop adsorption isotherm descriptions with parameters that can be estimated from the measured data. Based on these different theories the *IUPAC* classification was introduced to distinguish the different forms of adsorption, this classification framework is shown in fig. 2.6. In this figure Type I isotherms are indicative of microporous adsorbents. Types II and III, on the other hand, describe adsorption on macroporous adsorbents with strong and weak adsorbate-adsorbent interactions, respectively. Types IV and V correspond to adsorption isotherms exhibiting hysteresis. Lastly, type VI is characterized by isotherms featuring distinct steps.

By describing the adsorption of each component, the interaction between the molecule and the pore wall can be described, which is important for the use of Maxwell—Stefan surface diffusion. In the following section, different approaches to describe the adsorption of gases such as H_2 and CH_4 are described, followed by a more detailed description of the adsorption of vapors such as H_2O on carbon surfaces.

2.4.1 Adsorption of gases in porous carbon

Recent literature (Bienfait et al., 2004; Choi et al., 2003; de Oliveira et al., 2019) and the *Database of Novel and Emerging Adsorbent Materials* from (Daniel Siderius, 2023) indicate that only a limited number of data sets on porous carbon materials, and even fewer on nanoporous carbon materials, have been published regarding the adsorption of H_2 and CH_4. All available adsorption isotherms at the time of writing were recorded at temperatures up to 100 °C (compare section 2.4.6), leaving a gap in adsorption theory and isotherms for higher temperature regions. However, many porous membranes are utilized at higher temperatures for gas separation and are

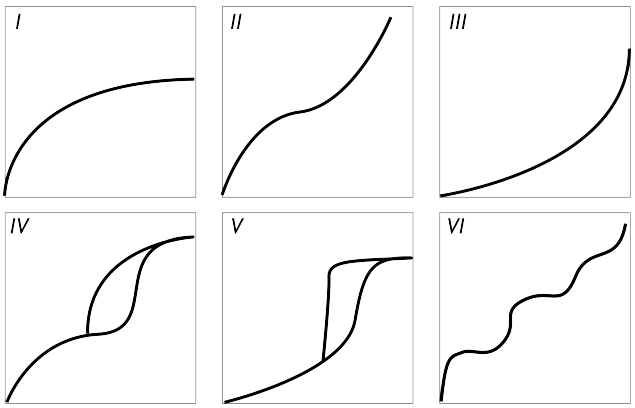

Fig. 2.6: The IUPAC classification of adsorption isotherms. Adapted from (Findenegg, 1992).

planned for use in membrane reactors, highlighting the need for further research in this area.

Therefore, conducting experiments and gathering additional data at higher temperatures is essential for advancing the understanding and application of porous carbon materials in gas separation and membrane reactor systems. To obtain reliable data, it is crucial to have a solid understanding of the theories underlying different adsorption isotherms.

Henry's law Henry's Law (compare eq. (2.28)) with K_H in $\mathrm{mmol\,g^{-1}\,Pa^{-1}}$ as the Henry's constant, describes the linear relationship between the partial pressure of a gas and its adsorbed amount q_i on the surface of a material (Erbil, 2006). In the context of gas adsorption on porous solids, Henry adsorption is particularly relevant for low-pressure regimes. According to Henry's Law, at low gas pressures, the amount of gas adsorbed on the porous solid is directly proportional to the gas pressure. This behavior is suitable for situations where the adsorption process is dominated by physical interactions, such as van der Waals forces, and the formation of a monolayer of gas molecules on the solid surface.

$$q_i = K_H p_i \tag{2.28}$$

Porous solids, such as activated carbon or zeolites, with their high surface areas and well-defined pore structures, often exhibit Henry adsorption behavior. Understanding Henry adsorption is crucial in applications such as gas storage, separation processes, and catalysis, where the ability to predict and control the adsorption behavior at low pressures is essential for optimizing performance and efficiency.

Langmuir Isotherm The Langmuir model is based on the assumption that the porous solid consists of a fixed number of distinct active sites located on a uniform surface. The assumptions made when using the Langmuir isotherm are that each site occupies only one molecule, that there is no mobility on the surface, and that the heat of adsorption is constant. It is assumed that the rate constants for the adsorption and desorption are invariant for all of the species.

$$\theta_i = \frac{q_i(p)}{q_{sat}} = \frac{bp_i}{1 + bp_i} \tag{2.29}$$

Various authors of published research have used the Langmuir isotherm for single gas adsorption (Hao et al., 2014; Monsalve-Bravo et al., 2023; Wang and Guo, 2020). The Langmuir isotherm provides a relatively simple description of gas or liquid adsorption on a solid surface (Cardoso et al., 2017; Gregg and Sing, 1982; Lagorsse et al., 2005; Laskar and Hashisho, 2020).

The expressions for single gas Langmuir models are given in eq. (2.29), which includes q_i, the amount of adsorbate i adsorbed by the solid in $\mathrm{mmol\,g^{-1}}$, and q_{sat}, the maximum amount the solid can adsorb at the specific temperature and pressure in $\mathrm{mmol\,g^{-1}}$. The fractional occupancy θ_i is the quotient of the latter two.

The Langmuir isotherm can be used for light adsorbed gases on porous media and offers a simple approach in describing the adsorption process.

Freundlich isotherm The Freundlich isotherm, originally proposed by Herbert Freundlich in 1922, is based on empirical observations (Freundlich, 1922). It lacks a rigorous theoretical derivation from fundamental principles and serves as a phenomenological model that effectively fits a wide range of experimental data. The

Freundlich isotherm (eq. (2.30)) is used to describe adsorption on heterogeneous surfaces where the adsorption energy varies across the surface. The underlying assumption of this model is that multiple layers of adsorbate can form on the surface, with each layer contributing to the total adsorption.

$$q_i = K_i^{fr} p_i^{n_i} \tag{2.30}$$

Toth isotherm The Toth isotherm (compare eq. (2.31)) is an empirical model that describes many sub-monolayer systems considerable well (Do, 1998; Tóth, 1995). The Toth isotherm serves as an extension of the Langmuir isotherm, providing a more adaptable model by incorporating an adsorption intensity parameter (f_i^{toth}). Its derivation assumes a comparable equilibrium between adsorption and desorption, but introduces a distinct functional form that accommodates a wider range of adsorption behaviors. The Toth isotherm is particularly valuable in situations where the adsorption process deviates from the strict assumptions of the Langmuir model. In contrast to the *Freundlich* isotherm it is thermodynamically consistent at low loading and therefore follows Henry's law in this loading regions.

$$q_i = q_{i,sat} \cdot \frac{K_i^{toth} p_i}{(1 + (K_i^{toth} p_i)^{f_i^{toth}})^{1/f_i^{toth}}} \tag{2.31}$$

Dubinin-Radushkevich isotherm The Dubinin-Radushkevich (DR) equation effectively describes vapor adsorption on activated carbons by modeling micropore filling based on the Polanyi potential theory (Dubinin and Serpinsky, 1981). Its ability to account for the heterogeneous microporous structure and characteristic adsorption energy makes it well-suited for capturing adsorption equilibria of subcritical vapors in these materials. Multiple sources, including (Cardoso et al., 2017; Gregg and Sing, 1982; Lagorsse et al., 2005; Laskar and Hashisho, 2020), have discussed the DR isotherm's assumptions and provided insight into its mathematical representation.

The Dubinin-Radushkevich isotherm assumes that the adsorption energy of the adsorbate decreases exponentially with the adsorbed amount, and that the porous material has a heterogeneous distribution of adsorption energies.

$$\theta_i = \frac{q_i(p)}{q_{sat}} = \exp\left[-\left(\frac{RT\ln(p_i/p_i^{LV})}{\varepsilon_i^{DR}}\right)^2\right] \tag{2.32}$$

Where p_i^{red} is the reduced pressure.

$$p_i^{red} = \frac{p_i}{p_i^{LV}} \tag{2.33}$$

In eq. (2.32) ε_i^{DR} is the characteristic energy. In (Lagorsse et al., 2005) an in depth comparison of different isotherm is discussed for the usage of single gases mixtures of condensible vapors. The reduced pressure p_i^{red} is used to describe the ratio between the partial pressure p_i and the vapor pressure of the component p_i^{LV} at given temperature T.

2.4.2 Adsorption of vapors on carbon

Vapor adsorption on carbon is a distinct theory due to the unique interactions and phase behaviors of vapors, which significantly influence adsorption dynamics and equilibria. In the following the main theory of water adsorption and one leading adsorption isotherm is described.

Theory of water adsorption in nanoporous material Research on the adsorption of water on nanoporous carbon is still ongoing, and a single conclusive theory is currently not available. Therefore, it's essential to summarize some approaches taken on this subject. Figure 2.7 illustrates the various stages of water adsorption in porous materials. According to publications such as (Do and Do, 2000; Do et al., 2009; Lagorsse et al., 2005), the primary mechanism for the adsorption process of water in porous carbon materials can be summarized as follows:

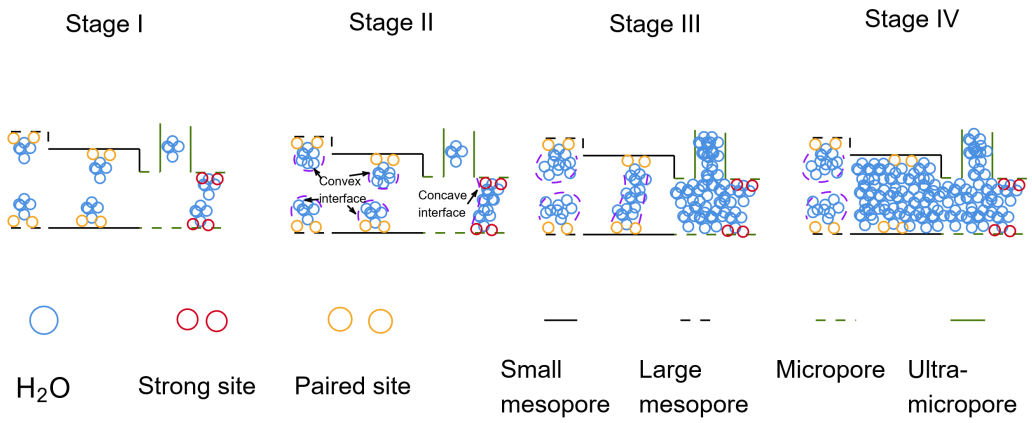

Fig. 2.7: Illustration of the theoretical different stages of water adsorption on porous carbon material. Figure after (Liu et al., 2017).

1) At low pressure the first adsorption occurs at functional oxygen groups which are part of the hydrophobic carbon material. In figure 2.7 the functional oxygen groups are shown as *Strong* and *Paired sites*, where the water molecules can adsorb most easily.

2) As the pressure increases, water molecules are added to the already adsorbed ones and form clusters. This growth continues up until a number of 5-8 molecules. At this point the pores with a pore diameter of 2 nm (Do and Do, 2000; Do, 1998; Lagorsse et al., 2005) fill with adsorbed water molecules.

3) With increasing reduced pressure ($p_i^{red} \simeq 0.9$ (compare section 2.4)) the water clusters move into the meso- and macro pores and pore condensation occurs.

While the *DR isotherm* (eq. (2.32)) effectively describes water adsorption at low relative pressures in porous media, it does not account for cluster formation or the effects of very narrow pore walls. Its use at low relative pressures is justified, as the DR isotherm is a robust model grounded in fluid-solid equilibrium theory from (Cardoso et al., 2017). However, at higher relative pressures, the results may be less reliable, indicating the need for an alternative approach.

Do adsorption isotherm Research on water adsorption, including studies cited in (Bhatia, 1993; Do and Do, 2000; Lagorsse et al., 2005), has led to an adsorption isotherm description that incorporates the concentration of the active sites and the formation of the stable clusters. One recent isotherm employed was the one proposed in (Do et al., 2009) and is shown in equation 2.34.

$$q_i = q_i^{sat} \frac{K_\mu \sum_{n=\alpha+1} x^n}{K_\mu \sum_{n=\alpha+1} x^n + \sum_{n=\alpha+1} x^{n-\alpha}} + S_0 \frac{K_f \sum_{n=1} n x^n}{1 + K_f \sum_{n=1} x^n} \tag{2.34}$$

The adsorption loading, noted as q_i in $\mathrm{mmol\,g^{-1}}$, is calculated alongside q_i^{sat} and S_0, the maximum adsorbed water concentration and the concentration of functional groups, respectively, both in $\mathrm{mmol\,g^{-1}}$. K_μ and K_f are used as dimensionless equilibrium constants for the adsorption isotherm, which need to be fitted to available data.

Theories presented in (Horikawa et al., 2011) and (Do et al., 2009) postulate that water molecules form clusters proximal only to functional groups in porous carbon. The concentration of these groups (S_0) was hence identified as an essential parameter in the isotherm equation. As the pressure increases, more water clusters accumulate until they reach a critical size (α), at which point their dispersive energy allows them to enter micropores ($d_p < 2\,\mathrm{nm}$). This accumulation continues until a relative pressure of 0.9, at which point capillary condensation occurs. Finally, due to the desorption of water clusters from the micropores, further adsorption is diminished once relative pressure surpasses 0.9.

2.4.3 Multi component adsorption isotherms

The studied adsorption isotherms of a single component serve as a basis for the study of adsorption systems. In most cases, adsorption systems involve multiple components, so it is essential to study equilibria where different types of molecules compete. This understanding is critical both for understanding the system itself and for design purposes , like mentioned in (Do, 1998). First, the extended Langmuir isotherm equation, the simplest theory for explaining multicomponent equilibria, is

introduced. The widely accepted Ideal Adsorption Solution Theory (IAST) is then presented.

Extended Langmuir isotherm Markham and Benton were responsible for developing the treatment of the extended Langmuir isotherm for binary systems (Markham and Benton, 1931). In this context, a comprehensive treatment for a multicomponent gaseous system containing NC species is given.

The same assumptions made for the pure component Langmuir isotherm, as described in section 2.4.1 are valid for the multicomponent case as well. The assumptions are the same for all described components. In eq. (2.35) the adsorption isotherm for the component i is given in a mixture with in total NC components.

$$\theta_i = \frac{q_i}{q_{i,sat}} = \frac{b_{L,i} p_i}{1 + \sum_{j=1}^{NC} b_{L,j} p_j} \tag{2.35}$$

While the extended Langmuir isotherm is theoretically sound, its assumptions during derivation - such as one molecule-one site interaction, no interaction between adsorbate molecules, and constant heat of adsorption with loading - are overly restrictive and may not be easily adapted to practical systems. As a result, it often falls short in accurately describing multicomponent adsorption equilibria. In the absence of universally superior models for describing equilibria, empirical approaches are often used. This is particularly evident in dynamic studies of adsorption columns, such as fixed bed or pressure swing adsorption (PSA) columns (Do, 1998; Kohl and Nielsen, 1997).

Ideal Adsorption Solution Theory Acknowledging the limitations of the extended Langmuir equation, despite its solid theoretical foundation in thermodynamics and kinetics, alternative approaches have been proposed. One such approach is the ideal adsorbed solution theory (IAST) by Myers and Prausnitz, from (Myers and Prausnitz, 1965), which predicts the adsorption behavior of gas mixtures based on the assumption that each component behaves as if it were in a separate ideal solution

on the adsorbent surface, with negligible interactions between different adsorbate molecules.

However, this work will not utilize IAST's theory. Instead, it focuses on the binary Langmuir isotherm to model the adsorption behavior of binary gas mixtures on solid surfaces. The binary mixture of components i and j can be described by the Langmuir isotherm, where the adsorption equilibrium for each component is defined independently.

2.4.4 Application of adsorption isotherms

In addition to calculating the surface loading of different species, physically based adsorption isotherms can be used to determine various properties of the observed material and the interactions between the adsorbent and the adsorbed component (adsorbate).

Isosteric heat of adsorption The isosteric heat of adsorption, denoted by $Q_{i,st}$, quantifies the enthalpic change associated with the process of transition of adsorbate molecules from the bulk gas phase to the adsorbed phase (Tun and Chen, 2021). It is an important parameter for the design of adsorption processes and provides insight into the heterogeneity of the gas-solid interface. $Q_{i,st}$ can be calculated or measured with different approaches described in the literature (Builes et al., 2013; Sircar et al., 1999; Tun and Chen, 2021). The data available for H_2 (Tun and Chen, 2021; Zheng et al., 2012; Zhou et al., 2004) and CH_4 (Abdulsalam et al., 2020; He and Seaton, 2006; Stadie et al., 2013) on carbon material varies from one material to the other and thus needs to be determined for each material to be used in further calculations.

The pure component $Q_{i,st}$ can be calculated using the *Clausius-Clapeyron equation* (eq. (2.36)) (Builes et al., 2013), where R, T and p_i are the universal gas constant, the temperature and the partial pressure of component i, respectively.

$$Q_{i,st} = RT^2 \left(\frac{\partial \ln p_i}{\partial T} \right)_{n_i} \tag{2.36}$$

Membrane characteristics Material characterization through adsorption isotherms, such as the Brunauer-Emmett-Teller (BET) and Dubinin-Radushkevich (DR) isotherms (compare section 2.4.1), provides valuable insights into the surface area, pore volume, and pore size distribution of porous materials. The BET isotherm is widely used for determining the specific surface area of materials by analyzing nitrogen adsorption data at liquid nitrogen temperature. It assumes multilayer adsorption and is particularly effective for characterizing mesoporous materials. Although it has wide application, the theory will not be explained further in this work. In contrast, the DR isotherm focuses on microporous materials and provides information about the energy of adsorption, allowing for the assessment of the material's porosity and adsorption capacity, compare (Do, 1998; Dubinin, 1959).

Advanced characterization methods, such as the Non-Local Density Functional Theory (NLDFT) and Monte Carlo simulations, complement traditional isotherm analyzes. The NLDFT method enables the calculation of pore size distributions and adsorption characteristics by modeling the adsorption process at a molecular level, accounting for the effects of pore geometry and surface heterogeneity. Meanwhile, the statistical Monte Carlo method simulates adsorption behavior, providing insights into the thermodynamic properties and phase behavior of adsorbates in porous materials, compare (Do, 1998).

2.4.5 Temperature extrapolation of adsorption isotherms

By applying the Langmuir isotherm (eq. (2.29)) one can include the apparent equilibrium constant b_i at different temperatures and following the argumentation in (Son et al., 2018; Tun and Chen, 2021; Yang, 1987) one can follow that eq. (2.37). Subsequently the eq. (2.38) can be used to calculate E_i from the slope of $\ln(E_i)$ over T^{-1}, and thus can be used to calculate $Q_{i,st}$ based on (He and Seaton, 2006).

$$Q_{i,st} = E_i \tag{2.37}$$

$$b_i = b_i^0 \exp\left(\frac{E_i}{RT}\right) \tag{2.38}$$

There are different approaches for extrapolation or interpolation, with dissimilarities in the case of H_2 and CH_4 as compared to H_2O. The adsorption of H_2 and CH_4 is explicated by means of *Langmuir* isotherms, which have the potential of extension within a predetermined range of the isosteric heat of adsorption (Q_{st}). In the following equations eq. (2.39) and eq. (2.40) the extrapolation can be achieved by estimating the parameter X on the available data and calculate the heat of adsorption with eq. (2.37) and eq. (2.38).

$$q_{sat} = q_{sat,0} \exp\left[X\left(1 - \frac{T}{T_0}\right)\right] \tag{2.39}$$

$$b_k = b_{k,0} \exp\left[\frac{Q_{st}}{RT}\left(\frac{T_0}{T} - 1\right)\right] \tag{2.40}$$

2.4.6 Available adsorption data

To provide a comprehensive understanding of the adsorption behavior in nanoporous carbon, the available adsorption data was analyzed using the Langmuir isotherm model (compare section 2.4.1). The choice of the Langmuir model was motivated by its simplicity, comparability of isotherms, and the excellent fit it provides for these membranes, allowing for effective comparison based on the equilibrium constant. This analysis also highlights the scarcity of data for temperatures exceeding 100 °C.

The Langmuir isotherm was employed to determine the equilibrium constant (b_i) from the measured adsorption isotherms. These values were then compared to findings from the NIST database (Daniel Siderius, 2023), encompassing activated carbons with larger pore sizes. Figure 2.8 visualizes this comparison.

Figure 2.8 further highlights the scarcity of data available for this specific temperature range. Coupled with the observed discrepancies, this necessitates further experimentation to solidify and expand the current understanding.

After describing the gap in the available adsorption data literature the conclusion from this analysis follows.

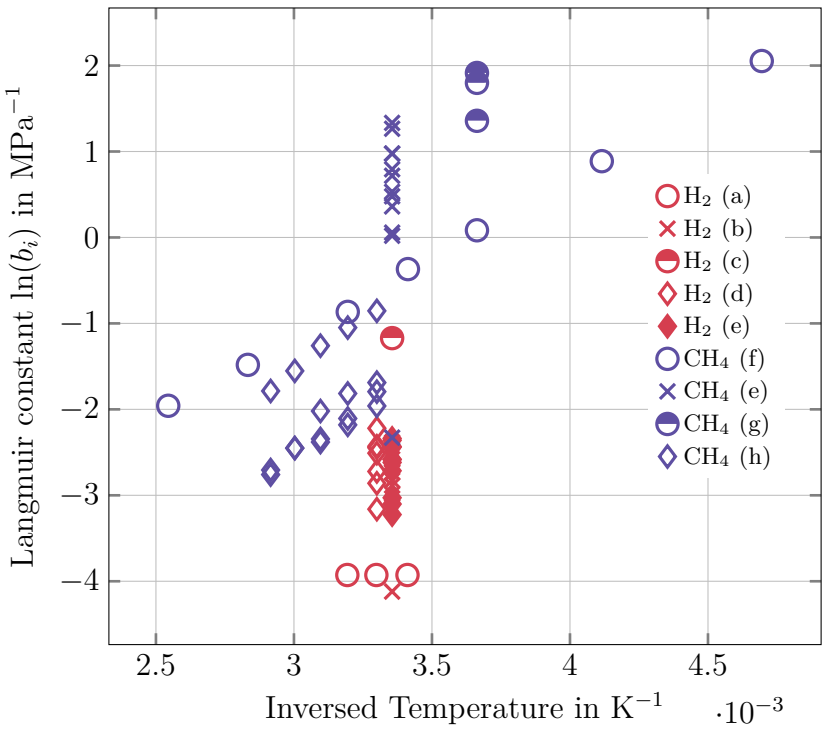

Fig. 2.8: Comparison of the available equilibrium constants from adsorption of hydrogen (Choi et al., 2003)(a), (Voskuilen et al., 2012)(b), (Rother and Fieback, 2013)(c), (Takagi et al., 2004) (d), (P. Marco-Lozar et al., 2012)(e) and methane (Men'shchikov et al., 2021)(f), (P. Marco-Lozar et al., 2012)(e),(Ito et al., 2013)(g), (Hao et al., 2014)(h) on different activated carbon materials at different temperatures available at (Daniel Siderius, 2023) with the published data of this work. Note that the carbon materials for each source cited are not the same and thus measured at one distinct temperature with different adsorption behavior.

2.5 Conclusion

Membranes play an important role in mitigating climate change by scalable and tailored applications. Nanoporous carbon membranes offer several advantages over other types of membranes. A sufficient mass transport description is vital for the future application of such membranes.

This literature review highlights a gap between experimental trials for permeation and adsorption of such an applied membrane system at industrial conditions and thus at elevated temperatures.

For instance the missing high-temperature adsorption data for hydrogen (H_2) and methane (CH_4) limit the development of accurate models, hindering progress in industrial application. Critical gaps remain in experimental data for water (H_2O) adsorption. A comprehensive analysis of isothermal models for H_2, CH_4, and H_2O is essential, since in the current literature very few data sets are measured in this temperature range.

Existing models based on molecular simulation lack real-world experimental validation, especially for Maxwell-Stefan surface diffusion in binary systems. The current literature lacks a comprehensive approach that combines molecular simulations and experimental data, creating a gap in the development of accurate and applicable surface diffusion models for different systems.

As mentioned in section 2.4.6, the available adsorption and permeation experiments for such membrane systems are performed at temperatures often below 100 °C. In order to use such models, this thesis's approach attempts to fill this gap by providing data for temperatures above 100 °C and a methodology to describe mass transport at higher temperatures.

In the following chapter the methods will be described that will help close the gap between experiments and applicable models by conducting experiments, analyzing the isotherms and the permeation through a membrane layer and develop a mass transport model, that can be applied to existing membranes.

3 Methods

This chapter introduces three key sections:

- The Experimental Section (section 3.1) provides a detailed description of the materials used and the experiments conducted.

- The Theoretical Modeling Section (section 3.2) offers an overview of the model and the assumptions made.

- The Computational Modeling Section (section 3.2) discusses the methods employed to translate the theoretical approach into code. Additionally, it outlines the libraries utilized for physical properties and the simplifications applied.

3.1 Experimental

Pure gases of hydrogen, methane and water vapor were used for adsorption experiments of the coating material of the active separation layer of a carbon membrane. Pure, binary and ternary mixtures of gases were used for permeation experiments with a sample of the nanoporous carbon membrane.

The membranes and coating materials were prepared at the Fraunhofer Institute for Ceramic Technologies and Systems (IKTS) in Hermsdorf, Germany. A Quantachrome Autosorb-iQ-C analyzer and a RuboLab RuboSORB magnetic suspension balance were used for the pure gas adsorption experiments on the carbon casting material. The results of standard characterization techniques applied to the cast material are summarized in table 3.1.

Tab. 3.1: Properties of the casted membrane material used for adsorption experiments.

S_{mic} $m^2\,g^{-1}$	V_{mic} $cm^3\,g^{-1}$	d_p nm	V_T $cm^3\,g^{-1}$	Adsorbate at temperature (Estimation method)
373	0.134	0.63	-	CO_2 at 273 K (Monte-Carlo)
385	0.127	0.57	-	CO_2 at 273 K (NLDFT)
415	0.156	1.03	-	CO_2 at 273 K (DR)
6	< 0.001	-	< 0.01	N_2 at 77 K (BET & DR)

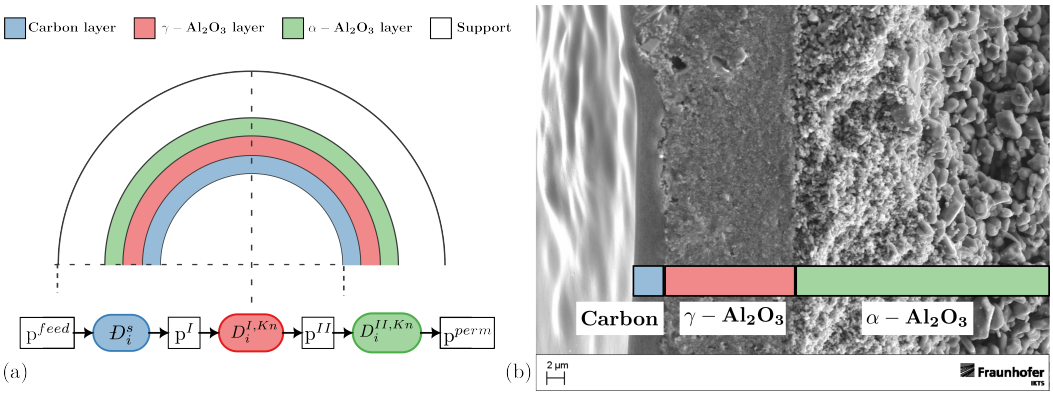

Fig. 3.1: (a)The carbon layer (nano pores) is modeled with Maxwell-Stefan surface diffusion, $\mathcal{D}i^s$, while the two Al_2O_3 support layers are described by Knudsen diffusion, D_i^{Kn}; the layers above these supports are not included in the model. (b) SEM picture of the membrane provided by the *Fraunhofer IKTS*, Hermsdorf.

The permeation experiments were performed using cylindrical membranes consisting of a nanoporous carbon layer supported by two additional layers. These membranes, as shown in fig. 3.1, have a length of 105 mm and outer and inner radii of 3.5 mm and 10 mm, respectively. For a comprehensive overview of the different layers and their parameters, see table 3.2.

In the following section, the various materials used are mentioned. The preparation process is outlined, along with the adsorption experiments conducted on two different devices and the permeation experiments.

3.1.1 Used material

Based on the reasoning for applying membranes in hydrogenation reactions discussed in the last chapter (see section 2.2.3), this work focuses on a nanoporous carbon

membrane, in this case prepared by Fraunhofer IKTS, Hermsdorf, Germany. The preparation process is outlined below.

Membrane preparation The membranes for the permeation experiments and the casting material for the adsorption experiments were prepared based on the publications in (Kämnitz et al., 2022; Weyd et al., 2008). The required chemicals for the synthesis of the active separation layer, furfuryl alcohol (PFA) and pyrrole, were purchased from MERCK (Germany). Polyethylene glycol methyl ether 750 (PEG 750) and concentrated nitric acid (HNO_3) were obtained from Sigma-Aldrich (Germany). The PFA precursor was synthesized according to an optimized formulation from Hucke (compare (Burket, 2007)). The polymer composition consisted of 30 mL furfuryl alcohol, 6 mL pyrrole, 15 mL PEG 750 and 1 mL concentrated nitric acid as catalyst. Furfuryl alcohol was added and pyrrole was added while stirring. PEG 750 was melted and added while stirring at high speed. Concentrated nitric acid was then added slowly while cooling (0.05 mL/300s). This was done using a titrator (Titronic ®300, SI Analytics). After the complete addition of the nitric acid, a black solution of the polymer was obtained. This polymer solution was used to coat the membranes. It was also used to prepare the casting material for the adsorption experiments.

Al_2O_3 single channel tubes with a 5 nm α-Al_2O_3 membrane layer were used as supports. The openings of the individual ducts are sealed by means of glass. Under clean room conditions, the inside of the tubes was coated by dip coating. A semi-automatic coating system (IKTS) was used for the coating of the inside of the tubes. Up to the glass seal mark, the single channel tube to be coated was immersed in the precursor solution. The tube was completely filled with PFA solution using a vacuum pump. The single channel tube was evacuated with nitrogen at a flow rate of $60\,\mathrm{mL\,min^{-1}}$ after a holding time of 60 s. The PFA coatings were first dried for 24 h under clean room conditions and then cross-linked at a temperature of 80 °C for 4 h in air. The polymer coatings were decomposed into carbon membranes by pyrolysis. For this process, the PFA coated supports were heated to 500 °C under nitrogen ($500\,\mathrm{L\,h^{-1}}$). From a pyrolysis temperature of 500 °C the system was switched to argon ($200\,\mathrm{L\,h^{-1}}$) and further heated to 670 °C. The system was switched back to nitrogen at a cooling temperature of 500 °C.

Casting material properties Several tests were performed on the cast material prior to the adsorption analysis in order to better understand the different adsorption results. A *3P micro 200 Porosity Analyzer (3P Instruments)* and an *Autosorb-iQ-C (Quantachrome)* were used to characterize the textural properties of the membranes by gas sorption. Pores ranging in size from sub-nanometers to several hundred nanometers were characterized using different adsorbents. The measurements with nitrogen at 77 K were carried out on a *Micro 200* using liquid nitrogen. For CO_2 sorption at 273 K, *Autosorb-iQ-C* equipped with a *CryoTune 195 (3P Instruments)* was used. Before analysis, membranes were vacuum pretreated for 30 min at 90 °C and 12 h at 250 °C to desorb preadsorbed molecules. A minimum sample mass of the casting membrane material of 250 mg was used.

Nitrogen sorption at 77 K was evaluated for specific surface area (S_{BET}) according to Brunauer, Emmett and Teller (BET) theory and micropore volume (V_{mic}) according to Dubinin-Radushkevich (DR) (Gregg and Sing, 1982) theory. The total pore volume (V_t) was determined at a relative pressure of p_{rel} 0.995. The CO_2 sorption data were evaluated using the Dubinin-Radushkevich (DR) method as well as Monte-Carlo and NLDFT models on carbons. More details on the Monte Carlo and DFT methods can be found in (Rouquerol et al., 2013). All characterization results are presented in table 3.1.

Properties of prepared membranes The membranes are cylindrical with an inner diameter of 7 mm and an outer diameter of 10 mm and have a length of 105 mm. A thin carbon membrane is supported by one layer of α-Al_2O_3 and one layer of γ-Al_2O_3 ceramics with different pore sizes. The different layers of the membrane are shown in table 3.2 with their respective pore sizes d_p, δ the thickness of the layer, the main material of the layer, the porosity of the layer ε and the calculated Knudsen number (compare eq. (2.11)) at 120 °C of H_2. A representation of the membrane is visualized in fig. 3.1. On the left-hand side, the different layers of the membrane and their respective modelling approaches are shown. For the carbon layer with nanopores, Maxwell-Stefan surface diffusion ($\mathcal{D}i^s$), and for the two Al_2O_3 support layers the Knudsen diffusion (D_i^{Kn}) are the principal mechanisms of mass transport. The layers above the two supporting layers are not considered in the model.

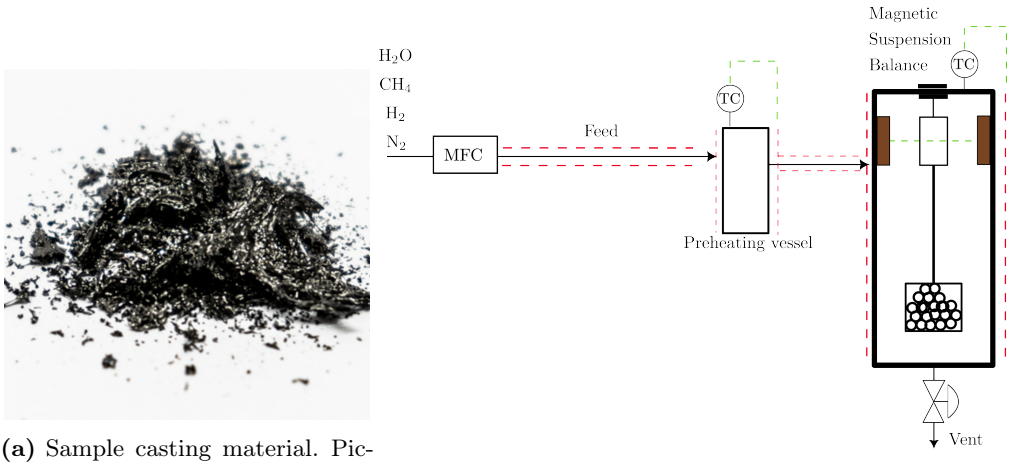

(a) Sample casting material. Picture taken by Rico Ehrentraut at DBFZ..

(b) Simplified PID of the RuboLab magnetic suspension balance.

Fig. 3.2: Left: Sample material which was tested for adsorption behavior. This material was produced by Fraunhofer IKTS on the basis of an alcohol precursor. Right: The simplified PID of the used RuboLab magnetic suspension balance.

Tab. 3.2: The different layers of the produced membranes by the Fraunhofer IKTS and the corresponding Knudsen number of H_2 at 120 °C in these layers calculated using eq. (2.11).

Layer	d_p in m	δ in µm	Material	ε in %	Kn	Mechanism
Support	$3.0{\cdot}10^{-6}$	$1.5{\cdot}10^{3}$	α-Al_2O_3	32 - 35	$4.9{\cdot}10^{-3}$	none
Coarse UF	$7.0{\cdot}10^{-8}$	$1.5{\cdot}10^{2}$	α-Al_2O_3	45	$2.1{\cdot}10^{-1}$	Knudsen
Fine UF	$5.0{\cdot}10^{-9}$	$1.0{\cdot}10^{1}$	γ-Al_2O_3	55	$2.9{\cdot}10^{0}$	Knudsen
Porous carbon	$4.0{\cdot}10^{-10}$	$2.0{\cdot}10^{0}$	Carbon	45	$3.5{\cdot}10^{1}$	Maxwell-Stefan

Other layers are added to the membrane for manufacturing purposes and to further supporting the active layer. For simplicity and to avoid revealing any intellectual properties, only those critical to mass transfer are considered. Following this line of thought all subsequent membrane layers are treated as a single support layer (see fig. 3.1).

3.1.2 Adsorption experiments

As described in chapter 2, to fill the gap of the missing adsorption isotherms at elevated temperatures is one of the major objectives of the present work. In the following subsection the adsorption experiments of pure gases at temperatures of maximum 120 °C for H_2 and CH_4 and for 90 °C for H_2O are presented.

Experimental setup and methodology The adsorbent's characteristics are shown in table 3.1, which were analyzed using standard methods utilizing N_2 and CO_2 adsorption. Prior to the measurment, the sample was pretreated in vacuum at 150 °C for 2 h to desorb any moisture content. With the pure gases of CH_4 and H_2 the adsorption is measured at 90 °C, 110 °C and 120 °C with the *RuboSORP* magnetic suspension balance at the institute *Dynamik und Betrieb technischer Anlagen (dbta)* of the *TU Berlin*. The simplified flow sheet is shown in fig. 3.2b. The pressure of the pure gas for each experimental trial is started at 5 bar and then increased to 45 bar with pressure increments of 5 bar. The pressure is maintained until equilibrium is reached with a maximum of 4 h and then maintained for 2 h for the measurement to be made. For H_2 and CH_4 the flow rates at each equilibrium point was set to be at 20 mL min^{-1}. The flow rate to increase the pressure between each experimental point was set to be 150 mL min^{-1}.

For the adsorption experiments with water the adsorption isotherms were measured at temperatures of 25 °C, 50 °C and 90 °C on two different experimental devices. The adsorption and desorption isotherm at 25 °C was measured on an *Autosorb-iQ-C (Quantachrome)* at DBFZ. The theory of adsorption of water is not based on the absolute partial pressure of the vapor but on the reduced pressure of the vapor which are mentioned in the applied adsorption isotherms for water (eq. (2.32) and eq. (2.34)) and in section 2.4.2. At the given temperatures water needs to be

in a mixture with other components to be gaseous and the experiments with the *RuboSorb* were carried out using N_2 as sweeping gas. Around $2\,\mathrm{mg\,min^{-1}}$ of H_2O were fed with $0.2\,\mathrm{L\,min^{-1}}$ into the feed stream. The water had a mole fraction of $0.123\,\mathrm{mol\,mol^{-1}}$.

The reduced pressure is defined in eq. (2.33) and since the reduced pressure has the main impact on the adsorption of water in porous carbon it is rather used as the design parameter of the experimental trials.

The experimental method had some drawbacks, since both devices used where limited in temperature. First the *Autosorb-iQ-C (Quantachrome)* is not capable of heating the sample above 25 °C secondly the *RuboSORP* balance has other limitations which are mentioned in section 3.1.4.

3.1.3 Permeation experiments

In the following section the permeation experiments at temperatures between 120 °C and 220 °C are presented and the difference in single, binary and ternary experiments are described. The overall methodology of the experiments is introduced and the avoided pitfalls are described.

Experimental setup and method The permeation experiments were performed using a permeation test rig (simplified flowsheet shown in fig. 3.3). The downstream permeate pressure and the feed pressure is controlled with a control valve.

The membrane is mounted with O-rings gaskets inside of a permeation testing cell shown in fig. 3.5. The cylindrical membranes can have a diameter of 10 mm and the active length of the membrane is limited by the distance between the gaskets of 81 mm. On each side of the housing are 8 mm *Swadgelok* fittings for the four different streams in the operation of the membrane. With the *feed* and *retentate* stream from and off the side of the housing, feeding the membrane on the inner side and with the *sweep* stream of N_2 sweeping the permeated material from the outer side of the cylindrical membrane to the *permeate* side. The gaskets are made of *FFKM* with a cord size of 2 mm and can withstand temperatures of up to 300 °C.

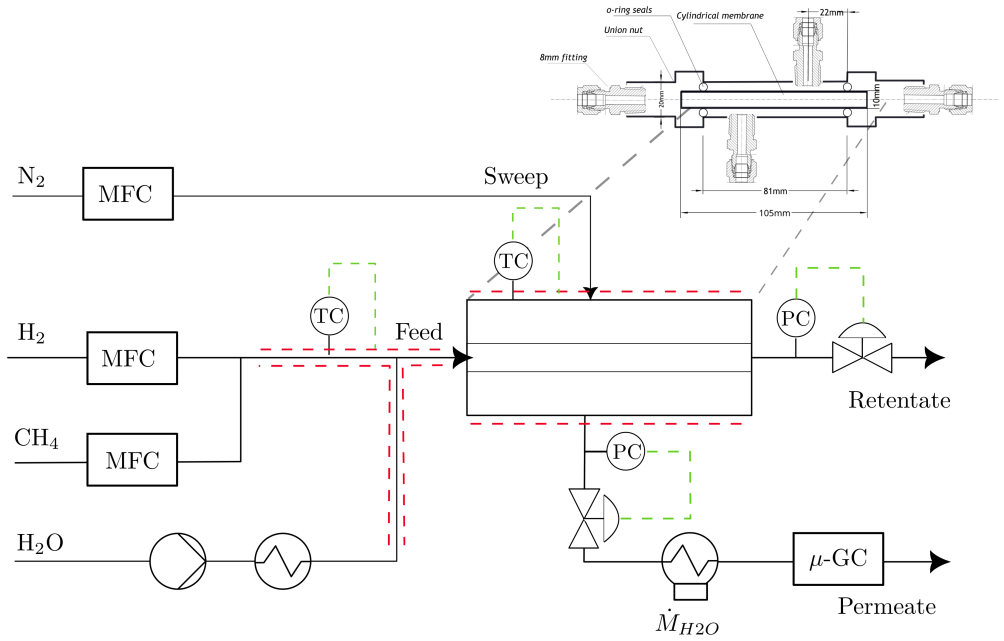

Fig. 3.3: Simplified PID of the permeation testing rig at DBFZ.

Fig. 3.4: Left: The structure of the used membrane with the three layers, Right: The simplified PID of the used permeation testing rig.

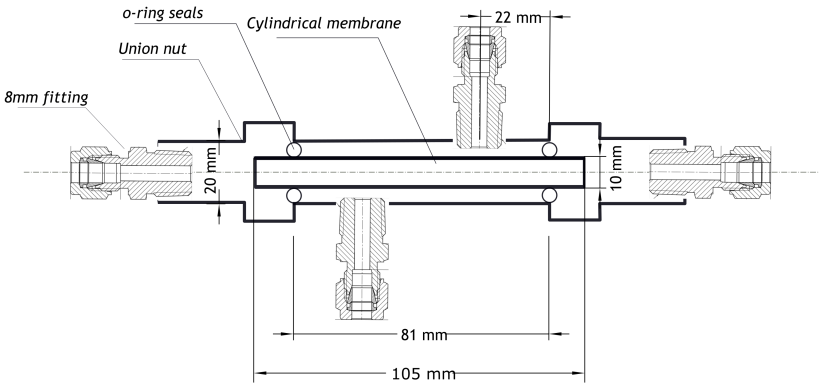

Fig. 3.5: Technical drawing of the permeation testing cell manufactured by Fraunhofer IKTS. Drawing: own work.

The permeation side of the membrane was flushed with a sweep stream of N_2 of $50\,L\,h^{-1}$ (STP). Before each experimental point the system is held at the experimental temperature for 2 h.

Pure gases of H_2, CH_4 and H_2O vapor are applied to the inner side of the membrane at different feed pressures (p^{feed}), permeate pressures (p^{perm}) and temperatures (T) and the permeation behavior is characterized based on the resulting permeate flux F_i^{perm}, which is calculated based on measured values. To ensure a static stream of H_2O a sweep stream of N_2 was used.

For experiments with water the water was pumped with a peristaltic pump and heated using pipe heat tracing. To ensure a static flow of vapor the trials with the pure water the pipe was flushed with 20 mL of N_2. The water content on the permeate side was measured using a condensation vessle at atmospheric pressure and at a constant temperature of 1 °C, which was established using an ice bath around the vessel. A discharging valve is placed at the bottom of the vessel, where every 2 min condensate is discharged and weighing with a *Radwag PS 1200.R2* balance. Downstream of the vessel the gas was dried with silica gel, in order to ensure the needed safety conditions for the μ-GC system. The silica gel was weighed before and after each experimental trial. The collected amount in the silica gel was at all experimental trials insignificant compared to the total value of water in the permeate stream and thus was not included in the calculation of the permeation stream.

With the membrane characteristics the permeation P_i of component i can be calculated (compare eq. (3.1)), where A^{mem} and Δp_i are the membrane surface in m^2 and the pressure drop in bar.

$$P_i = \frac{F_i^{perm}}{A^{mem}\Delta p_i} \tag{3.1}$$

The temperature is varied from 120 °C over 170 °C to 220 °C. The pressures were varied in accordance to the design of experiments, which is shown in the annex chapter C. The gas composition of the permeate stream was analyzed every 4 min using an *Inficon μ-GC* downstream of the permeation test rig. Each experimental point was measured over the time of 30 min.

Knowing the sweep flow (F^{Sweep}) in $\mathrm{mol\,min^{-1}}$, the composition (x_i) of the permeate stream, by the gas chromatic analysis and the water content, assuming an ideal gas the permeation flow F_i^{perm} through the membrane can be calculated with eq. (3.2).

$$F_i^{perm} = \frac{x_i \cdot F^{sweep}}{x_{N_2}} \tag{3.2}$$

All experimental conditions for the pure, binary and ternary permeation experiments are shown in table 3.3 and are marked with numbers from (0) up to (6) for the corresponding experiments.

Pure component experiments The pure component experiments ((0) to (2) in table 3.3) varied by gas because of differences in setups and permeances. For CH_4, feed pressure ranged from 5 bar to 15 bar; for H_2, from 2 bar to 5 bar; and for water, the reduced pressure (compare eq. (2.33)) varied from 0.2 to 0.4 and up to 0.6. To minimize systematic error, a *design of experiments (DoE)* with a factorial design and Response Surface Methodology (RSM) was established, and the set points for the pressure and temperature levels were adjusted accordingly. A complete description of the DoE is shown in chapter C.

Binary permeation experiments For the binary experiments ((3) to (5) in table 3.3) of H_2 and CH_4 the composition was set to be at H_2: 30 mol % and CH_4: 70 mol %. The pressure was varied between 5 bar and 15 bar with H_2 and CH_4. With mixtures of H_2O the reduced pressure p_i^{red} of the feed was the main design parameter, that was varied from 0.2 over 0.4 up to 0.6.

To show the influence of H_2O as a third component in the binary experiments, mixtures of H_2/H_2O and CH_4/H_2O were fed to the feed side of the membrane. The mixtures were adjusted in order to meet the conditions for the needed reduced pressured p^{red} ranges and thus the compositions were not stable over the course of the different temperatures and pressure ranges. Binary permeation experiments with H_2O exhibit a high margin of error in measuring the water flow through the

membrane; therefore, the calculated permeances P_i and separation factors $S_{i,j}$ are also prone to significant errors.

The compositions and conditions of the binary permeation experiment are shown in table 3.3.

Ternary permeation experiments For the ternary experiments ((6) in table 3.3) the composition of H_2, CH_4 and H_2O was chosen with CO_2 methanation in focus. As mentioned in section 2.2.1, the hydrogenation of CO_2 with H_2 produces a number of different gas compositions consisting of the main products CH_4 and H_2O with residues of CO_2 up to 2 % and H_2 up to 5 %, depending on the process conditions. A stable nanoporous carbon membrane can be used in-situ or downstream of a CO_2 methanation reactor, where the composition of the feed can vary from one modification to the other. In this context a downstream application is used, where the temperatures are lower than in the actual reactor and the feed consists only of small amounts of educt components. In order to achieve the feed compositions a Gibbs reactor was modeled with the aid Aspen Plus™at $T = 400\,°C$, $p = 5\,bar$ and with a feed composition of H_2: 80 % and CO_2: 20 %, which is a stoichiometric ratio of 4:1 (H_2:CH_4). The resulting composition of the product gas downstream of the reactor is CO: 0.04 %, H_2: 10.31 %, CH_4: 29.02 %, CO_2: 2.55 % and H_2O: 58.08 %.

Based on the insignificant amounts of CO and CO_2 these components where left out and just the amounts of H_2, CH_4 and H_2O where used in the ternary experiments. The used composition is shown in table 3.3.

Tab. 3.3: Composition and Design of experiment used for the different permeation experiments. The numbers indicate the experimental conditions used for references.

Experimental Trial Number	0	1	2	3	4	5	6
Experimental parameter	H_2	CH_4	H_2O	H_2 | CH_4	H_2O | H_2	H_2O | CH_4	H_2 | CH_4 | H_2O
x	1	1	0.99	H_2: 0.3 CH_4: 0.7	H_2O: 0.41 H_2: 0.59	H_2O: 0.73 CH_4: 0.27	H_2: 0.1 CH_4: 0.3 H_2O: 0.6
T_{max}	120 °C	120 °C	120 °C	120 °C	120 °C	120 °C	120 °C
T_{min}	220 °C	220 °C	220 °C	220 °C	220 °C	220 °C	220 °C
p_{min}^{feed}	2 bar	5 bar	$p^{red} = 0.2$	5 bar	5 bar	5 bar	5 bar
p_{max}^{feed}	2.5 bar	15 bar	$p^{red} = 0.6$	15 bar	15 bar	15 bar	15 bar
p_{min}^{perm}	1 bar	1 bar	1 bar	1 bar	1 bar	1 bar	1 bar
p_{max}^{perm}	1.75 bar	3 bar	2 bar	2 bar	2 bar	2 bar	3 bar
F	0.018 mL min^{-1}	0.037 mL min^{-1}	5 g min^{-1}	H_2: 0.018 mL min^{-1} CH_4: 0.037 mL min^{-1}	H_2O: 5 g min^{-1} H_2: 24 L h^{-1}	H_2O: 2 g min^{-1} H_2: 60 L h^{-1}	H_2: 0.103 mL min^{-1} CH_4: 0.29 mL min^{-1} H_2O: 0.58 mL min^{-1}

3.1.4 Limitations and experimental error

The experiments were subject of some limitations, these will be discussed here.

Adsorption experiments The amount of adsorbate on the adsorbent decreases with increasing adsorption temperature, limiting the maximum measurable temperature to the balance's sensitivity. For the *RuboSORB* magnetic suspension balance, the maximum temperature for gas adsorption of H_2 and CH_4 on the tested material is 120 °C, making measurements above this temperature unviable.

Experiments detected H_2O residues of 20 ppm for H_2 and 100 ppm for CH_4 in the adsorption vessel, but these are not expected to significantly affect the results. The experimental error of the *RuboSORB* is 10^{-3} mg.

With H_2O the limitations are different, since the feed needs to bypass a preheating vessel fig. 3.2b, which has a design maximum temperature of 80 °C. Based on this design the maximum measurement temperature is limited by the condensation of vapor in this preheating vessel. Combined with the reduced pressure of $p^{red} = 0.8$, the maximum possible temperature in the water adsorption experiments was set to be 90 °C. In addition to these limitations the adsorption of N_2 onto the casting material was neglected, since N_2 is needed as a sweeping gas for the experimental trials.

Due to the complexities of water adsorption measurements and the significant difference between modeled and measured temperatures, only the highest directly measured temperature of 90 °C was used. No extrapolation of water adsorption was performed, as the associated error would have been impractical to incorporate.

Permeation experiments Due to the different permeabilities of CH_4 and H_2 the feed pressures of the pure component experiments could not be the same, since the mass flow controller were not able to provide a mass flow to set a feed pressure higher than 5 bar. All sensors and the associated accuracy for the permeation experiments are shown in table 3.4. As described above the feed pressure for the pure water experiments is varied according to the reduced pressure. Thus the three pure component experiments don't share the same feed pressures.

Tab. 3.4: The sensors and the measurement error for permeation experiments for the device in fig. 3.3.

Sensor description	Sensor name	Error σ	Measurement frequency
Temperature sensor	TC	1.5 °C	constant
Pressure sensor	PC	0.1 bar	constant
Gas chromatography	μ-GC	0.1 %	4 min
Gas flow	MFC	0.3 %	constant
Water pump	GQ	0.3 %	constant
Water condensation	$\dot{M}_{H_2O}$	standard deviation	2 min

The error of the permeation measurements is calculated by the standard deviation of the readings and is used in the Monte Carlo simulation. The technique used for measuring the water content in the permeate stream has a high standard deviation and thus is prone to error.

As described above, the experiments were conducted with H_2, CH_4, and H_2O. Including CO_2, which is often present in processes relevant to this work and can reach concentrations up to 15 mol mol^{-1}, would have been worthwhile, but it was avoided for several reasons: the experimental handling of CO_2 in the used apparatus was not suited and would have exceeded the project budget, and introducing a fourth component would have overly complicated the study. Consequently, CO_2 was not studied here.

The experiments ensured a stable system for two hours before each trial, allowing data analysis under the assumption of steady state. This simplifies permeation calculations by neglecting nitrogen (N_2) due to its minimal transfer across the membrane driven by the low pressure difference between the feed and permeate sides (eq. (3.2)).

For all experimental trials the error is calculated based on the standard deviation σ of the measured values.

Water in the experiments There are different implications on the measurement error when introducing water in the experiments. In general when dealing with water the important parameter is often not the absolute (partial) pressure of water p_{H_2O}, but the reduced pressure $p^{red}_{H_2O}$ (compare eq. (2.33)).

The binary permeation experiments with H_2O suffer from the high margin of error of the measurement of the water flow through the membrane and thus the connected permeances and the selectivities are prone to a high margin of error. This is due to the limitations of the testing rig, where the mass flow controller (MFC) needed to be used for all conditions presented. The binary permeation experiments with H_2O were mainly used to be compared to the pure component permeation experiments. Based on these limitations of the MFCs the permeation experiments at 220 °C were not able to reach the conditions and thus were skipped in the DoE. Due to limitations of the water feeding system at temperatures of 120 °C the reduced pressure was only achievable for to be at $p^{red}_{H_2O} = 0.08$. At the temperatures of 170 °C and 220 °C all desired reduced pressure were able to be achieved.

The adsorption isotherms were only able to be measured up to a temperature of 90 °C due to limitations in the experimental setup and the measurement of the permeation of water in the permeation experiments are bound to a high standard deviation. Those two experiments impose this error into all calculations that base on the experimental trials. This error can be quantified by the Monte-Carlo method in contrast to other types of error.

With the water adsorption any extrapolation is not physically sensible and thus is not performed. This alone imposes a non quantifiable bias onto all measurement and models using this data. In addition to that any usage of multi component isotherms with water adsorption is prone to error (Bhatia, 1993; Do et al., 2009). The objective to have a running model and be able to prove the presented method has a higher priority in to this work than building a physical sound system based on measurement with a high error in themselves.

Processing of experimental data The data from the μ-GC, the water measurements and the sensor data were processed, each with its own time stamp. For data manipulation and analysis, we used Python and specifically the Pandas library to calculate the mentioned parameters. Within each measurement point, the arithmetic mean were calculated using the *NumPy mean* function and the standard deviation by aggregating measurements over the course of one experimental point.

3.2 Theoretical modeling

The nanoporous membrane is used to separate gases due to different adsorption and surface diffusion properties within the active layer. In order to describe this mass transport process, some restrictions and simplifications must be made. As can be seen in fig. 2.4, there are several ways to represent and calculate the mass transport in a porous membrane layer. As shown in fig. 3.6, the use of the chemical potential as driving force has the particular advantage that no discontinuity occurs at the phase interface and therefore the whole membrane with adsorption and desorption description can be used within one description. If the gas phase concentration x_i is used, the adsorbed concentration θ_i can be used with the help of an adsorption isotherm to calculate the mass transfer.

As described in the section 3.1.4 water adsorption is prone to a high error in measurement and the highest usable temperature was 90 °C. Since the system with water description already shows a high level of error a simplification was considered where the water adsorption isotherm at 90 °C was taken and corrected with a simple linear temperature dependent reduction in adsorbed mass, to incorporate with the higher temperatures as shown in eq. (3.3), where T_0 is 363.15 K (90 °C) and $b_{i=3}$ is the water Langmuir parameter at 90 °C.

$$q_i(T) = \frac{b_{i=3}(T_0)p_{i=3}}{1 + b_{i=3}(T_0)p_{i=3}} \cdot \frac{T_0}{T} \tag{3.3}$$

Different layers of the membrane The membrane consists of three layers, as shown in fig. 3.1. Based on the adsorption and the permeation data a single component mass transport model was developed to calculate the Maxwell-Stefan and Knudsen diffusion coefficients in the carbon and in the support layers of the membrane, respectively (compare fig. 3.1 and eq. (3.6) and eq. (3.4)).

The thickness of the effective membrane layers ($< 200\,\mu m$) is negligibly small compared to the inner radius of the membrane with 3.5 mm, so the membrane is treated as a flat surface and Cartesian coordinates are used.

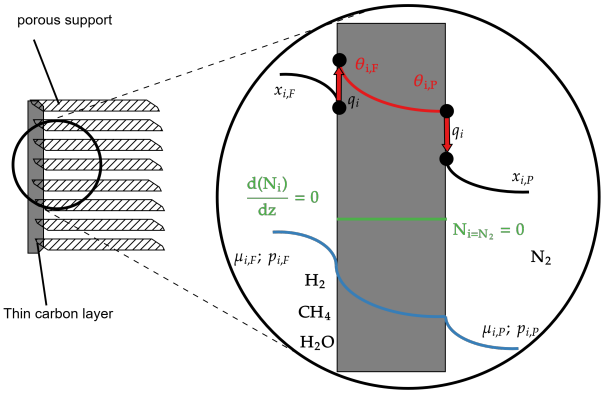

Fig. 3.6: Pressure profile in the membrane layer, with a simplified membrane structure with one active membrane layer and a porous support. The chemical potential μ_i (blue) and the concentration (red) are shown qualitatively. The condition of constant flux through the membrane is shown as well.

The given membrane consists of three different layers with different pore sizes and thicknesses as shown in table 3.2 and fig. 3.1.

Starting from eq. (2.17) the integration over the length of the membrane leads to the formulation for one component for the $\mathcal{D}_i^s$ in eq. (3.4), where $\mathcal{D}_i^s$ is the Maxwell-Stefan surface diffusion coefficient in $\mathrm{m^2\,s^{-1}}$, N_i^s as the molar flow in $\mathrm{mol\,m^{-2}\,s^{-1}}$, p_i the partial pressure in Pa, ρ, the material's density in $\mathrm{mol\,m^{-3}}$, ε the membranes porosity and θ_i the fractional occupancy of the surface.

$$\mathcal{D}_i^s = -\frac{N_i^s p_i}{\rho \varepsilon \theta_i} \tag{3.4}$$

The Knudsen number for the support layer are out of the Knudsen regime and thus Al_2O_3 layers with a pore diameter greater than $d_p \geqq 100\,\mathrm{nm}$ will be neglected in the description of the mass transport through the membrane. As previously described, gas transport through mesoporous media involves various mechanisms. One simple approach is Knudsen diffusion, which is compared with other methods for the Al_2O_3 layer in (Gao et al., 2012, 2013). For the support layer of α-Al_2O_3 with an average pore size of $d_p \approx 70\,\mathrm{nm}$ (compare (Gao et al., 2012)), Knudsen diffusion is dominant,

accounting for at least 80% of the mass transport resistance. Viscous flow is negligible in this region based on mass transport resistance comparisons.

In the interlayer of γ-Al_2O_3 with a mean pore size of $d_p \approx 5\,\text{nm}$, Knudsen diffusion is applicable but tends to overestimate gas diffusion. An alternative approach, the *oscillator model*, is suggested in (Gao et al., 2013), although Knudsen diffusion remains a useful model. Consequently, Knudsen diffusion is employed for both support layers.

As an example the Knudsen diffusion flow for the α-Al_2O_3 layer is defined as follows, according to (Nagy, 2018):

$$N_i = -D_i^{II,Kn} \frac{p_i^{II} - p_i^{perm}}{RT\Delta\delta^{\alpha}} \tag{3.5}$$

Here, δ^{α} is the thickness of the intermediate layer, and p_i^{II} is the pseudo partial pressure at the interface between the γ-Al_2O_3 and α-Al_2O_3 interlayers. This equation applies to both interlayers.

For the porous carbon layer with a pore size of approximately $d_p = 0.42\,\text{nm}$ (compare (Kämnitz et al., 2022)), Knudsen flow is not applicable. In these narrow pores, molecules are consistently influenced by the pore wall force field (Krishna and van Baten, 2008). Therefore Maxwell-Stefan Surface Diffusion is used to describe the present mass transport.

3.2.1 Pure gas mass transport

Following the previously defined descriptions for the individual gas transport through the three porous layers (eq. (3.6) - eq. (3.8)) by Knudsen diffusion, the partial pressure difference between each layer is calculated (see fig. 3.1) using the known pressures on both sides of the membrane. Thus, knowing the measured flow by eq. (3.9), the MS diffusion coefficients $\mathcal{D}_i^s$ can be calculated with eq. (3.10), using the pressure difference between the feed pressure p_i^{feed} and the first intermediate pressure p_i^I.

Carbon layer:

$$N_i^s \int_0^{\delta_C} dz = -\mathcal{D}_i^s q_i^{sat} \varepsilon^C \rho^C \int_{p_i^{feed}}^{p_i^{II}} \frac{\theta_i}{p_i} dp_i \tag{3.6}$$

The Knudsen diffusion coefficients can be written with eq. (2.15):

γ-Al_2O_3 layer:

$$N_i^{Kn,\gamma} = \frac{4}{3} \frac{\varepsilon^\gamma}{\tau^\gamma} \frac{d_p^\gamma}{\sqrt{2\pi RTM_i}} \frac{p_i^{II} - p_i^I}{\delta^\gamma} \tag{3.7}$$

α-Al_2O_3 layer:

$$N_i^{Kn,\alpha} = \frac{4}{3} \frac{\varepsilon^\alpha}{\tau^\alpha} \frac{d_p^\alpha}{\sqrt{2\pi RTM_i}} \frac{p_i^{II} - p_i^{perm}}{\delta^\alpha} \tag{3.8}$$

And with:

$$N_i^{Kn,\alpha} = N_i^{Kn,\gamma} = N_i^s \tag{3.9}$$

One can calculate the Maxwell-Stefan surface diffusion coefficients:

$$\mathcal{D}_i^s = -\frac{N_i^s \delta_C}{q_i^{sat} \epsilon^C \rho^C \int_{p_i^{feed}}^{p_i^{II}} \frac{\theta_i}{p_i} dp_i} \tag{3.10}$$

Since the difference between the partial pressure and fugacity for hydrogen (H_2) and methane (CH_4) is minimal (around 1% at 20 bar), the thermodynamic correction factor (Γ_i) was set to 1 (see eq. (2.20) and section 3.2.4). Fugacity calculations are detailed in listing B.2.

Based on the *Vignes Method* eq. (2.26) the binary interaction parameters $\mathcal{D}i,j^s$ of the Maxwell-Stefan surface diffusion and the binary interaction parameters of the

Knudsen diffusion $D_{i,j}^{Kn}$ are calculated. See section 2.3.4 for more detail and the methodology is described in fig. 3.7.

As described in (Yang, 1987) an empirical equation (compare eq. (3.11)) can be used to estimate surface diffusion $\mathcal{D}_i^s$ coefficients based on the isosteric heat of adsorption Q_i^{st}, where the isosteric heat of adsorption is adjusted by an arbitrary factor m (compare eq. (3.12)). This assumption is based on (Gilliland et al., 1974; Wang et al., 2004) and takes into account the effect of the adsorption energy on the surface diffusion rate.

The dependence of $\mathcal{D}_i^s$ can be described using:

$$\mathcal{D}_i^s = \mathcal{D}_i^{0,s} \exp\left(-\frac{E}{RT}\right) \tag{3.11}$$

Where $\mathcal{D}_i^{0,s}$ is the reference value at T_0 and E is the activation energy for surface diffusion. With the introduction of an arbitrary parameter m this can be plotted over the isosteric heat of adsorption Q_i^{st}:

$$\frac{Q_i^{st}}{mRT} \tag{3.12}$$

3.2.2 Binary mass transport of hydrogen and methane

In analogy to section 3.2.1, the description of binary mass transport becomes more complex due to the inclusion of an additional component in the model. The same understanding of the intermediate pressures p_i^I and p_i^{II} mentioned in section 3.2 holds for the binary case. The intermediate pressure between the layers of the membrane can not be calculated analytically, though and must be integrated in the numerical calculation. For this approach different additional parameters are needed to be used in the binary modeling approach. The binary interaction parameters and the binary description of the adsorption isotherms need to be integrated in the description of the Maxwell-Stefan surface diffusion and Knudsen diffusion description.

As described in fig. 3.7 the calculated binary interaction parameters $\mathcal{D}i,j^s$ and $D_{i,j}^{Kn}$ are calculated using Vignes method eq. (2.26) and eq. (2.27) with the pure component values described in section 3.2.1.

The binary case of the mass transport description needs to be formulated for all three layers. The consequent transportation mode is shown in fig. 3.1. All equations show the same structure which is used by (Krishna and van Baten, 2008) and described in theory in section 2.3.4.

Starting with the basic formulation:

$$-\frac{q_i}{RT}\nabla\mu_i = \sum_{j=1,i\neq j}^{n} \frac{q_j N_i - q_i N_j}{c_T \mathcal{D}_{ij}^s} + \frac{N_i}{\mathcal{D}_i^s} \tag{2.19}$$

with:

$$c_T = \sum_i^n q_i \text{ and } q_i = \theta_i q_{i,sat} \tag{3.13}$$

The adsorption of hydrogen and of methane on the nanoporous carbon layer can be described using the Langmuir isotherm (compare eq. (2.29)) and thus the binary interaction adsorption is described using the extended Langmuir isotherm (eq. (2.35)).

$$\theta_i = \frac{b_i p_i}{1 + b_{i=1} p_{i=1} + b_{i=2} p_{i=2}} \tag{3.14}$$

With the Onsager coefficients from (Krishna and van Baten, 2008) and the assumption of ideal gases one can follow:

$$\mu_i = \mu_i^0 + RT \ln(x_i) \tag{3.15}$$

$$N_i = \sum_{i=1}^{n} L_{i,j} \nabla\mu_i \tag{3.16}$$

$$\nabla\mu_i = \frac{RT}{p_i}\nabla p_i \tag{3.17}$$

The formulation for the Knudsen flow is similar but with a description of the molar concentration x_i instead of the adsorbed concentration:

$$-\frac{x_i}{RT}\nabla\mu_i = \sum_{j=1,i\neq j}^{n} \frac{x_j N_i - x_i N_j}{c_T D_{ij}^{Kn}} + \frac{N_i}{D_i^{Kn}} \tag{3.18}$$

After writing out for the binary case and rearranging (see appendix in chapter A) the flow of H_2 and CH_4 can be described using the Onsager formulated case:

$$N_1 = -RT\left[\frac{L_{11}(p_1,p_2)}{p_1}\frac{dp_1}{dz} + \frac{L_{12}(p_1,p_2)}{p_2}\frac{dp_2}{dz}\right] \tag{3.19}$$

$$N_2 = -RT\left[\frac{L_{21}(p_1,p_2)}{p_1}\frac{dp_1}{dz} + \frac{L_{22}(p_1,p_2)}{p_2}\frac{dp_2}{dz}\right] \tag{3.20}$$

Together with the formulated binary case of the Onsager formulated set of equations eq. (3.19) and eq. (3.20) the equation system can be solved considering the constant flow in the membrane layer

$$\nabla N = 0 \tag{3.21}$$

In the following the explanatory reformulation of the eq. (2.19) is shown, to develop the Onsager coefficients.

$$N_1 = -\frac{\alpha_1}{\beta_1 p_1}\frac{dp_1}{dz} + \frac{\gamma_1}{\beta_1}N_2 \tag{3.22}$$

$$N_2 = -\frac{\alpha_2}{\beta_2 p_2}\frac{dp_2}{dz} + \frac{\gamma_2}{\beta_2}N_1 \tag{3.23}$$

$$\begin{aligned}\underbrace{\left(-\frac{q_{1,sat}\theta_1}{p_1}\right)}_{\alpha_1}\frac{dp_1}{dz} = N_1\underbrace{\left(\frac{q_{2,sat}\theta_2\mathcal{D}_1 + (q_{2,sat}\theta_2 + q_{1,sat}\theta_1)\mathcal{D}_{1,2}}{(q_{1,sat}\theta_1 + q_{2,sat}\theta_2)\,\mathcal{D}_{1,2}\mathcal{D}_1}\right)}_{\beta_1} - \\ N_2\underbrace{\left(\frac{q_{1,sat}\theta_1}{(q_{1,sat}\theta_1 + q_{2,sat}\theta_2)\mathcal{D}_{1,2}}\right)}_{\gamma_1}\end{aligned} \tag{3.24}$$

$$\begin{aligned}\underbrace{\left(-\frac{q_{2,sat}\theta_2}{p_2}\right)}_{\alpha_2}\frac{dp_2}{dz} = N_2\underbrace{\left(\frac{q_{1,sat}\theta_1\mathcal{D}_2 + (q_{1,sat}\theta_1 + q_{2,sat}\theta_2)\mathcal{D}_{1,2}}{(q_{1,sat}\theta_1 + q_{2,sat}\theta_2)\,\mathcal{D}_{1,2}\mathcal{D}_2}\right)}_{\beta_2} - \\ N_1\underbrace{\left(\frac{q_{2,sat}\theta_2}{(q_{1,sat}\theta_1 + q_{2,sat}\theta_2)\mathcal{D}_{1,2}}\right)}_{\gamma_2}\end{aligned} \tag{3.25}$$

Then rewrite for N_i

$$N_1 = -\frac{\alpha_1}{\beta_1}\frac{d\mu_1}{dz} + \frac{\gamma_1}{\beta_1}N_2 \tag{3.26}$$

$$N_2 = -\frac{\alpha_2}{\beta_2}\frac{d\mu_2}{dz} + \frac{\gamma_2}{\beta_2}N_1 \tag{3.27}$$

rearranging:

$$N_1 = -\underbrace{\frac{\alpha_1\beta_2}{\beta_1\beta_2 - \gamma_1\gamma_2}}_{L_{11}}\frac{d\mu_1}{dz} - \underbrace{\frac{\gamma_1\alpha_2}{\beta_1\beta_2 - \gamma_1\gamma_2}}_{L_{12}}\frac{d\mu_2}{dz} \tag{3.28}$$

$$N_2 = -\underbrace{\frac{\alpha_2\beta_1}{\beta_1\beta_2 - \gamma_1\gamma_2}}_{L_{21}}\frac{d\mu_2}{dz} - \underbrace{\frac{\gamma_2\alpha_1}{\beta_1\beta_2 - \gamma_1\gamma_2}}_{L_{22}}\frac{d\mu_1}{dz} \tag{3.29}$$

And with eq. (3.21) the formulation is fixed.

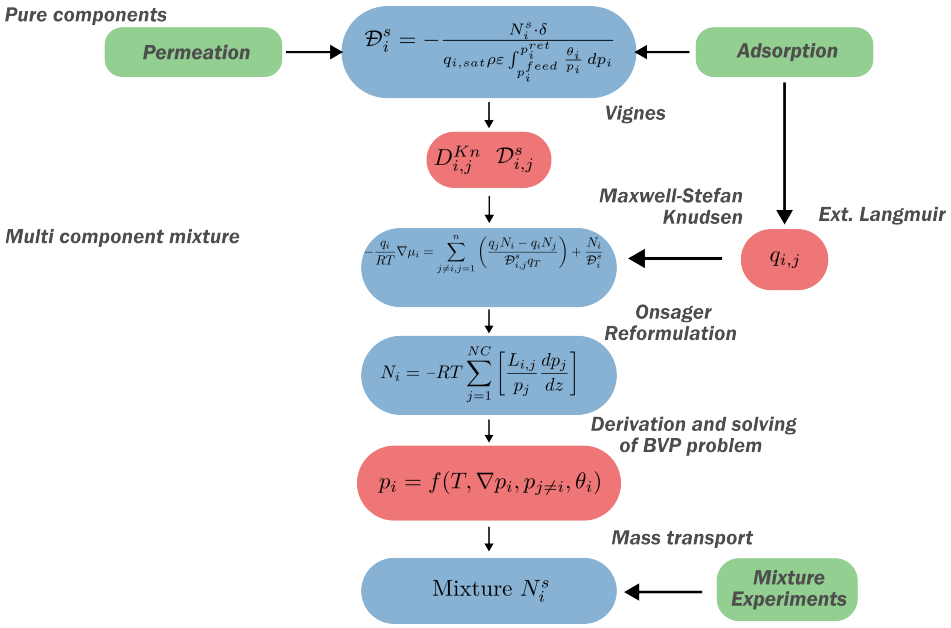

Fig. 3.7: Flow Chart of the modeling approach for a multi component mixture with the aid of pure component experimental data.

For the sake of simplicity the derivation of the Onsager formulated equations is shown in the Appendix (chapter A) and the computational calculation and implementation is shown in section 3.3.

3.2.3 Ternary Mass transport

The understanding of the intermediate pressures for each component (i), denoted p_i^I and p_i^{II}, remains consistent with the concept presented for the binary case in section 3.2. However, an analytical calculation of these intermediate pressures is not possible and requires numerical integration within the computational framework. This approach requires the inclusion of additional parameters beyond the binary case. In particular, the ternary interaction parameters and the ternary description of the adsorption isotherms must be incorporated into the existing model for Maxwell-Stefan surface diffusion and Knudsen diffusion.

By principle the ternary case is described in the same way as the binary case, the computational solution shows nevertheless a higher complexity and at some points simplifications.

With the start of the Onsager formulation for each of the three layers:

$$N_i = \sum_{i=1}^{n} L_{i,j} \nabla \mu_i \tag{3.16}$$

The ternary case can be written out accordingly:

$$N_1 = -RT \left[\frac{L_{11}(p_1,p_2,p_3)}{p_1} \frac{dp_1}{dz} + \frac{L_{12}(p_1,p_2,p_3)}{p_2} \frac{dp_2}{dz} + \frac{L_{13}(p_1,p_2,p_3)}{p_3} \frac{dp_3}{dz} \right] \tag{3.30}$$

$$N_2 = -RT \left[\frac{L_{21}(p_1,p_2,p_3)}{p_1} \frac{dp_1}{dz} + \frac{L_{22}(p_1,p_2,p_3)}{p_2} \frac{dp_2}{dz} + \frac{L_{23}(p_1,p_2,p_3)}{p_3} \frac{dp_3}{dz} \right] \tag{3.31}$$

$$N_3 = -RT \left[\frac{L_{31}(p_1,p_2,p_3)}{p_1} \frac{dp_1}{dz} + \frac{L_{32}(p_1,p_2,p_3)}{p_2} \frac{dp_2}{dz} + \frac{L_{33}(p_1,p_2,p_3)}{p_3} \frac{dp_3}{dz} \right] \tag{3.32}$$

The Onsager coefficients need to be described using the Maxwell-Stefan definition of the current case. This implies rewriting this case using the binary adsorption isotherms. When every isotherm can be described using Langmuir isotherms, the binary adsorption isotherm is describable with eq. (2.35). Although the calculations did not result in a useful model, the proposed approach for water as a third component is described in the following section.

Adaptation with water as third component As described in section 2.4.2 water is best described using different adsorption theories like the isotherm of *Do and Do* eq. (2.34) (compare (Do et al., 2009)) or for the description of lower loading θ_i with the use of *Dubinin-Radushkevish* eq. (2.32) (compare (Laskar and Hashisho, 2020)), where the formation of water clusters included in the calculation of the isotherms.

With the water adsorption isotherm the ternary case for the three layers can be described.

Starting from the basic formulation in eq. (2.19) and using the extended Langmuir formulation

$$\theta_i = \frac{b_i p_i}{1 + b_{i=1} p_{i=1} + b_{i=2} p_{i=2} + b_{i=3} p_{i=3}} \tag{3.33}$$

Due to measurement errors and experimental limitations (see section 3.1.4), the H_2O system of equations requires further simplifications. All assumptions are outlined in section 3.2.4.

The assumptions and simplifications affect the applicability of the results. The three-layer model, where two layers are described by Knudsen diffusion (see section 3.2), is not optimal for water vapor. According to (Gao et al., 2014), Knudsen diffusion is not applicable to mass transport through porous membranes. As a result, only the carbon layer can be modeled, necessitating an estimation of the interface partial pressure, which introduces a notable error in the calculations of $\mathcal{D}i^s$.

The derivation of the model for three components, including H_2O, involved numerous assumptions, leading to convergence challenges. A solution was found using isotherms from the literature at approximately 25 °C; however, no solution could be achieved with the measured adsorption isotherms and diffusion coefficients.

In contrast, a binary model (described in section 3.2.2) involving two components (H_2 and CH_4) has been successfully developed and is utilized in this work. This binary model provides reliable results and is more applicable given the limitations encountered with the three-component model.

Given the numerous assumptions in the three-component model, the interpretation of the results may be limited. Therefore, only the model development is described here and included in the annex, as its application with more suitable adsorption and permeation data holds potential value.

3.2.4 Assumptions and simplifications

In the following the assumptions and simplifications used for the theoretical model in this work are presented.

No charged particles are calculated and considered not present, neglecting electrostatic effects according to (Krishna and Wesselingh, 1997). Ideal gas law is assumed to be valid, neglecting the non-ideality effects. As a basis fugacity calculations for H_2 and CH_4, excluding H_2O where conducted prior to the calculation. A single spatial coordinate is employed, representing a flat membrane with constant area ($A \neq f(r)$) (membrane thickness is significantly smaller than its radius).

Only Knudsen flow (compare section 2.3.3) is considered within the membrane's support layers, neglecting viscous flow contributions (Knudsen flow is the dominant transport mechanism). The Maxwell-Stefan surface diffusion coefficients ($\mathcal{D}_i^s$) are independent of loading conditions ($\mathcal{D}_i^s = \mathcal{D}_i^s(\theta_i = 0)$) (compare (Nagy, 2018)). The model assumes an isothermal membrane, neglecting temperature variations (no specific reference for energy balance description). The water adsorption isotherm at 90 °C is used for all modeling and diffusion coefficient calculations. This is due to the fact, that any extrapolation from the scarce data sets to the higher temperatures of water are prone to error. The adsorption isotherms that are able to describe the adsorption of water reasonably do not offer any way to extrapolate the adsorption isotherm. Using the calculation using the isosteric heat of adsorption Q_i^{st} is not a viable way, since the calculation is too prone to error.

3.3 Computational modeling

The described model and the experimental trials have been incorporated in the present work with the help of different computational approaches. This section aims to give an overview of the different numerical libraries used and the way in which they supported the solution. This work is dealing with experimental data that is prone to experimental error. This error has to be implemented in the calculation and therefore Monte Carlo simulation is often used and will be described in the following subsection with the use cases, compare section 3.3.2.

3.3.1 Adsorption isotherm parameter estimation

The method described in section 3.2 is used to calculate parameters for adsorption isotherms from the experiments described in section 3.1. In order to be able

to calculate the adsorption isotherm parameters based on the limited data points available a sufficient software package is needed. In this study, the mopeds package written in *Python* was used to estimate isotherm parameters associated with different adsorption isotherms, compare (Volodymyr Kozachynskyi, 2025). The *IPOPT* algorithm from (Wächter and Biegler, 2006) was used estimate the parameters. The parameters of different adsorption isotherms are estimated using the non-linear optimization *CasADi* software package, compare (Andersson et al., 2019) with the *IPOPT* solver, implemented in the *mopeds* framework. To understand the physics of the recorded adsorption isotherms the *PyGaps* library was used from (Iacomi and Llewellyn, 2019).

3.3.2 Monte Carlo simulation method

The resulting error of all the experimental data is calculated using the standard deviation or the root mean square deviation (DMSE) of the functions with the estimated parameters and the measured values as the parameter estimation error from (Feldman and Cousins, 1998). All available data points are used to estimate the parameters of the model. These estimated values are then taken as the *true* parameters for subsequent simulations. To quantify the error associated with parameter estimation, the squared correlation coefficient (R^2) is calculated. This value reflects the proportion of the observed data variance that can be explained by the model. Next, new values of the dependent variable are generated for a number of trials. These simulated values are generated based on the estimated parameters and the previously calculated error. For each generated value, the model parameters are re-estimated. This re-estimation process is repeated for all trials. Finally, the spread of the resulting curves is analyzed to determine the 1 σ (one standard deviation) range. With this method, the error of all the used numerical calculation are incorporated into the simulation if the error of the input parameter is quantifiable.

3.3.3 Numerical solution of mass transport equations

As described in section 3.2 the Onsager formulated Maxwell-Stefan surface diffusion equation needs to be derived and then solved for the partial pressures. The formulation of the boundary value problem of the partial pressure of each component is

analytically not feasible and thus a system of computer aided libraries written in python were used to implement an automatic derivation system where a boundary value problem is created, that is solvable with the aid of other numerical libraries for python, as can be seen in listing B.1.

Using the python library *SymPy* and using LaTeXsyntax (as shown in eq. (2.19), eq. (3.19) and eq. (3.20)) the equation system can be defined. The Onsager coefficients L_{ij} are determined for each layer and using the Maxwell-Stefan equations they are determined by rearranging the different terms. This is done in *SymPy* as well. The resulting equations are then turned into computable functions using the *lambdify* function of the *SymPy* library, which turns the symbolic values into numerical values usable for the *NumPy* library. This is done for each component and the three layers.

The layers are subdivided in a series of finite elements for each of them the partial pressure functions can be evaluated. The function calls of the different layers are merged into one definition of a boundary value problem. The number of finite elements is $NE = 32$ for each layer of the membrane. Additional layers were considered; however, the computational time increased significantly without improving accuracy, and prior to this number, the results varied. This boundary value problem (BVP) is solved using the boundary conditions of the partial pressures on each side of the membrane layer and with initial conditions which were chosen to be a linear profile from the feed to the permeate side of the membrane. The code for this approach is attached in the annex of this work in chapter B.

3.4 Model variations

The model predictions for binary experiments are expected to deviate significantly from experimental values due to the large uncertainties in diffusion coefficients, the simplifications applied in this study (see section 3.2.4), and the extrapolation of temperature data (see section 2.4). To improve the accuracy of our binary model predictions, we have implemented two additional strategies to address potential discrepancies.

3.4.1 Accounting for confined space effects

Bhatia et al. (K. Bhatia et al., 2011) build on the work of Krishna (Krishna and van Baten, 2009) to describe a method for adjusting surface diffusion coefficients to reflect the effects of mass transport within confined spaces, such as slit pores with diameters ranging from $d_p = 1\,\text{nm}$ to $0.6\,\text{nm}$, which is comparable enough to the present membrane.

In these confined environments, binary mass transport is influenced both by interactions with the second component and by the spatial constraints. Krishna introduces a correction factor ζ_i, referred to as a fuzzy parameter by Bhatia et al. (K. Bhatia et al., 2011), to account for these effects. The parameter ζ_i, which ranges from 0 to 1, is calibrated to align with experimental results.

$$D_{i,j}^{conf} = D_{i,j} \cdot \zeta_i \tag{3.34}$$

In eq. (3.34) the binary diffusion coefficients are adjusted by the ζ_i factor to account for confined space effects. This parameter can be introduced into the binary model in order to incorporate a slight over interpretation of the model's mass transport.

3.4.2 Temperature dependence adjustment

Following the adjustment for confined space effects, we also consider the impact of temperature on the model results. To evaluate the impact of temperature on the model results, a logarithmic temperature-dependent function (see eq. (3.35)) was introduced. A logarithmic correction was chosen as it is well-suited to describe weak to moderate temperature sensitivity over a limited temperature range.

In this approach, the pure-component Maxwell-Stefan surface diffusion coefficient is scaled by a constant ϕ_i and a logarithmic term involving temperature:

$$\mathcal{D}_i^{s,T} = \mathcal{D}_i^s \cdot (\phi_i \ln(T)) \tag{3.35}$$

In this context, ϕ_i represents a component specific parameter to correct the temperature related behavior of $\mathcal{D}_{i,s}$. The values of ϕ_i are determined by the binary mass transport experiments described in section 4.1 and the model results from section 3.2. The results of the model and of the experiments are used for a parameter estimation utilizing the *L-BFGS-B* optimization algorithm as implemented in *SciPy* from (Virtanen et al., 2020). The used code is described in listing B.3.

As a result, the two approaches outlined will be integrated into the model to account for the overestimation of the mass transport and to introduce a simple temperature dependency of the mass transport.

The simplifications outlined in section 3.2.4, the experimental challenges highlighted in section 3.1, and the general limitations associated with the Maxwell-Stefan modeling approach collectively provide a solid foundation for justifying the introduction of this adjustment. Furthermore, they present an opportunity to further develop the model, as the mentioned improvements indicate areas where additional work may be required.

In summary, these adjustments for confined space effects and temperature dependence enhance the model's accuracy and provide a foundation for further development.

3.5 Variable variation study

After the numerical solution the validated mass transport model can be used to calculate data with conditions closer to industrial application processes, like described in section 2.2.1. As described in table 3.5 the influence of temperature on the permeance on consequently on the separation factor $S_{\mathrm{H_2,CH_4}}$ by varying temperature from 220 °C to 340 °C under fixed system parameters. Separation factor results were compared with experimental and optimized data and extrapolated to assess trends at higher temperatures. As detailed in section 3.3, the diffusion coefficient ($\mathcal{D}_i^s$) was not directly calculated at each temperature; instead, the nearest available value was used to avoid interpolation or extrapolation, which in turn would introduce an unquantifiable error to the system.

Tab. 3.5: Varied variables for the binary system of H_2 and CH_4. The Separation factor was analyzed for the comparison of the system.

Variable	Minimal value	Maximal value	Step size	Fixed value	Unit
x_{H_2}	0.3	0.95	0.05	$T = 220\,°C$	$mol\,mol^{-1}$
T	220	340	10	$x_{H_2} = 0.3\,mol\,mol^{-1}$	°C

In contrast to that adsorption isotherms for H_2 and CH_4 were extrapolated following the method in eq. (2.40), while the Langmuir isotherm for water at 90 °C was applied as described in section 3.2. To incorporate uncertainties, Monte Carlo simulations were performed (see section 3.3.2). The feed composition x_i^{feed} was varied from $0.3\,mol\,mol^{-1}$ to $0.95\,mol\,mol^{-1}$ with a step size of $0.05\,mol\,mol^{-1}$. The system temperature was extrapolated from the measured temperature of 220 °C up to 340 °C, a relevant industrial range balancing applicability and error margin. The full table for all the other variable that were kept constant is attached to this work in chapter F.

4 Results

In this chapter the results of the permeation and adsorption experiments are presented combined with the results from the developed model.

The adsorption and permeation behavior of a nanoporous carbon membrane was investigated in the laboratories of *Dynamik und Betrieb technischer Anlagen (dbta)* at *TU Berlin* and *DBFZ* in Leipzig, Germany. These experiments are the first objective of the work, since there is a gap in the available literature for permeation and adsorption data for nanoporous carbon membranes. With the measured adsorption isotherms and the performed permeation experiments a binary and ternary mass transport model can be developed. The developed model offers an adaptable methodology for other gases and describes the used simplifications (see section 3.2.4). It enables extrapolation to calculate membrane mass transport for industrial applications.

In most figures a color coding for a second parameter (temperature, pressure, etc.) is used to demonstrate additional information. One important result is gathered from the comparison between the ratio of pure components permeance P_i^{pure}, see eq. (2.5) with the binary or ternary permeances and thus the separation factor $S_{i,j}$. The mentioned binary or ternary permeance P_i describes the permeance of one distinct component in the binary or ternary mixture.

First the permeation results in section 4.1 are presented. Following this, section 4.2 details the adsorption data, comparing different adsorption isotherms and their estimated parameters, calculated according to chapter 3.

Subsequently, section 4.3 presents the calculated Maxwell-Stefan surface diffusion coefficients and the results of the binary mass transport model. Based on the validated model, predictions are then made and discussed in section 4.5.

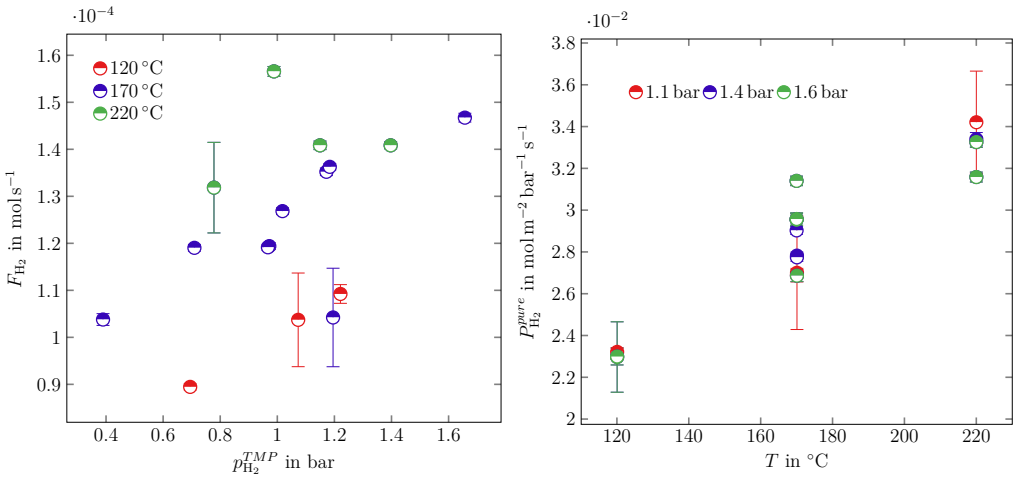

(a) Single component Flow F_{H_2} in mol s^{-1} over the transmembrane pressure p_i^{TMP} in bar of H_2.

(b) Single component permeance of H_2 $P^{pure}_{H_2}$ in mol m^{-2} bar^{-1} s^{-1} over the temperature in °C.

Fig. 4.1: Single component permeance in mol m^{-2} bar^{-1} s^{-1} and flow in mol s^{-1} of H_2 over the membrane. Experimental trial (0) from table 3.3.

4.1 Permeation experiments

In the following section the results of the pure component, binary and ternary mixture permeation experiments are presented as described in section 3.1.3.

4.1.1 Pure component permeation

The pure component permeation is the basis for the calculation of the Maxwell-Stefan surface diffusion coefficients $\mathcal{D}_i^s$ and thus plays an important role in the current work. The following figures show the permeance and flow of H_2, CH_4 and H_2O through the membrane over the system temperature T and the feed pressure p^{feed} or the reduced pressure p_i^{red}.

In fig. 4.1a the flow of H_2 is shown over the transmembrane pressure $p^{TMP}_{H_2}$, where the flow increases basically linear with increasing transmembrane pressure. The fig. 4.1b shows the permeance of H_2 versus temperature for the three different feed pressures used, shown in red, blue and green. The same is done for the calculated flow F_i versus feed pressure for the three different temperatures used, shown in red, blue

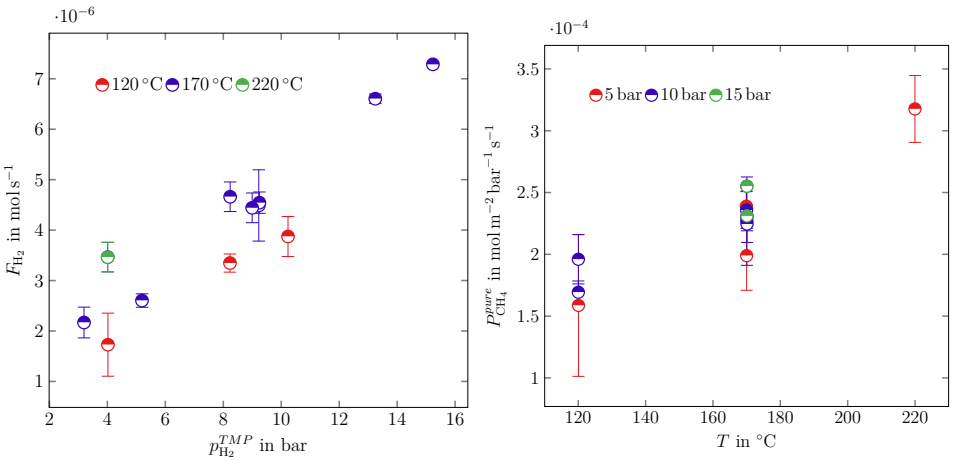

(a) Single component Flow F_{CH_4} in $\mathrm{mol\,s^{-1}}$ over the transmembrane pressure $p^{TMP}_{CH_4}$ in bar of CH_4 with a permeate pressure varying from 1 bar up to 2 bar.

(b) Single component permeance $P^{pure}_{CH_4}$ in $\mathrm{mol\,m^{-2}\,bar^{-1}\,s^{-1}}$ over the temperature in °C of CH_4.

Fig. 4.2: Single component permeance in $\mathrm{mol\,m^{-2}\,bar^{-1}\,s^{-1}}$ over the temperature T in °C and flow in $\mathrm{mol\,s^{-1}}$ of CH_4 over the transmembrane pressure $p^{TMP}_{CH_4}$. Experimental trial (1) from table 3.3.

and green. The permeance increases with temperature from 2.2 $\mathrm{mol\,m^{-2}\,bar^{-1}\,s^{-1}}$ to 3.3 $\mathrm{mol\,m^{-2}\,bar^{-1}\,s^{-1}}$. This is shown in fig. 4.1b where the feed pressure has no effect on the permeance.

For CH_4, fig. 4.2b and fig. 4.2a depict its behavior as feed pressure (p^{feed}) changes from 5 bar to 15 bar. A linear dependency is evident in fig. 4.2b, though fig. 4.2a suggests a slight dependence on inlet pressure for CH_4.

Looking at the pure component behavior of H_2O over different system parameters. As described in section 3.2.3, the introduction of water necessitating the analysis of its behavior using reduced pressure (p^{red}) to account for phase changes and strong adsorption effects.

However, fig. 4.3b shows a clear dependence of the flow on the feed pressure from 1 bar to 12 bar, where the flow raises from $0.15 \times 10^{-3}\,\mathrm{mol\,s^{-1}}$ up to $2.7 \times 10^{-3}\,\mathrm{mol\,s^{-1}}$ indicating a linear dependency. The temperature is varied from 120 °C up to 220 °C. There is no visible dependency of the flow on permeate pressure as shown in fig. 4.3a. Following the fig. 4.3b illustrates H_2O flow over feed pressure. A clear temperature dependence, as seen with H_2 and CH_4, is absent; instead, after increasing with

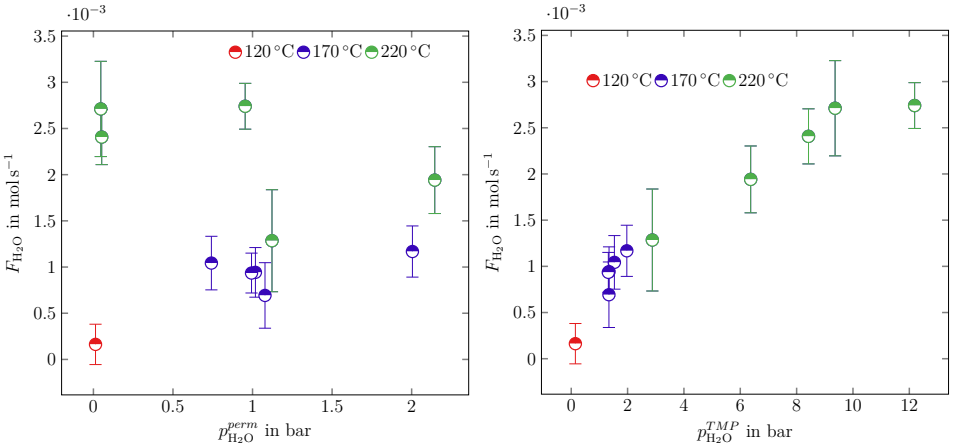

(a) Single component flow F_{H_2O} in mol s^{-1} over the permeate pressure p^{perm} in bar of H_2O.

(b) Single component flow F_{H_2O} in mol s^{-1} over the transmembrane pressure $p^{TMP}_{H_2O}$ in bar of H_2O.

Fig. 4.3: Single component flow over the transmembrane pressure $p^{TMP}_{H_2O}$ and the permeate pressure $p^{perm}_{H_2O}$ of H_2O. Experimental trial (2) from table 3.3.

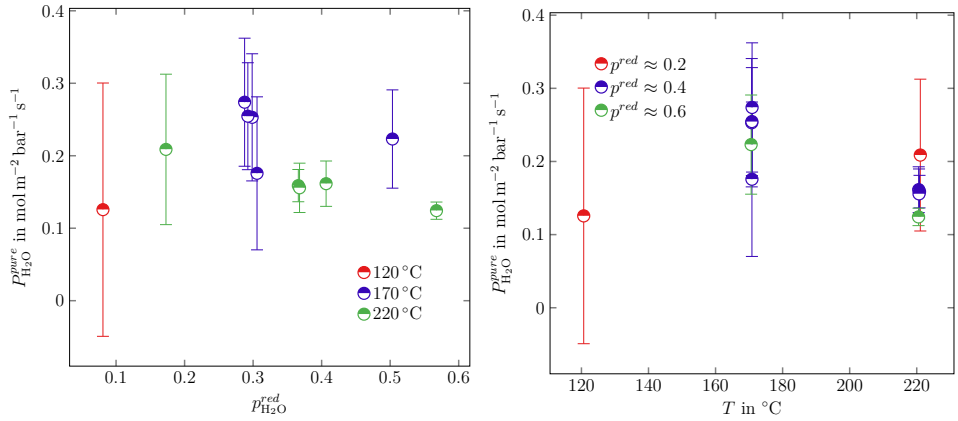

(a) Single component permeance $P^{pure}_{H_2O}$ in mol m^{-2} bar^{-1} s^{-1} over the reduced pressure of H_2O.

(b) Single component permeance $P^{pure}_{H_2O}$ in mol m^{-2} bar^{-1} s^{-1} over the temperature in °C of H_2O.

Fig. 4.4: Permeance P_{H_2O} in mol m^{-2} bar^{-1} s^{-1} of H_2O over the temperature T and the reduced pressure $p^{red}_{H_2O}$. Experimental trial (2) from table 3.3.

temperature, the permeance drops at higher values. The strong vapor pressure dependence of water necessitated that higher pressure flows were conducted at elevated temperatures as described in chapter 3. As shown in fig. 4.4a, the dependence on the reduced pressure (eq. (2.33)) is also clear. This dependence can be partly explained by considering the different modes of water adsorption (fig. 2.7) and mass transport in nanoporous membranes (fig. 2.4).

The behavior of H_2O differs significantly from H_2 and CH_4. The fig. 4.4b shows H_2O permeance increasing from $0.12\,\mathrm{mol\,m^{-2}\,bar^{-1}\,s^{-1}}$ at 120 °C to $0.5\,\mathrm{mol\,m^{-2}\,bar^{-1}\,s^{-1}}$ at 170 °C, then decreasing to $0.2\,\mathrm{mol\,m^{-2}\,bar^{-1}\,s^{-1}}$. When comparing the three different pure component experiments, the difference is that water permeance is two orders of magnitude higher than the permeance of H_2, which in turn is two orders of magnitude higher than the permeance of CH_4.

When dealing with complex permeation behavior, an important factor is binary permeation, where individual components influence each other and thus a different permeation is observed.

The results of the binary permeation experiments will be discussed in the following.

4.1.2 Binary permeation of methane and hydrogen

In the case of binary permeation, the permeation behavior of the components influences each other as explained in section 2.3.4. The binary flow of CH_4 and H_2 over the feed pressure p^{feed} is shown in fig. 4.5 as a function of the temperature T. A dependence on the feed pressure and temperature is visible. The higher the temperature and the feed pressure the higher the flow, which is physical sensible.

The permeance of CH_4 with values in the range of $2 \times 10^{-4}\,\mathrm{mol\,m^{-2}\,bar^{-1}\,s^{-1}}$ (Compare fig. 4.6a) shows a dependence towards T and p^{feed}. Permeance of H_2 with values of $2 \times 10^{-2}\,\mathrm{mol\,m^{-2}\,bar^{-1}\,s^{-1}}$ shows a positive correlation towards T, but a negative towards p_i^{TMP} (compare fig. 4.6b).

In fig. 4.7a the binary and pure component permeance of H_2 and CH_4 over the temperature T is shown. The difference between pure and binary permeance is within the margin of error. So there is no influence of the H_2 as a second component. In fig. 4.7b the pure component permeance is higher by a factor of about 50 %

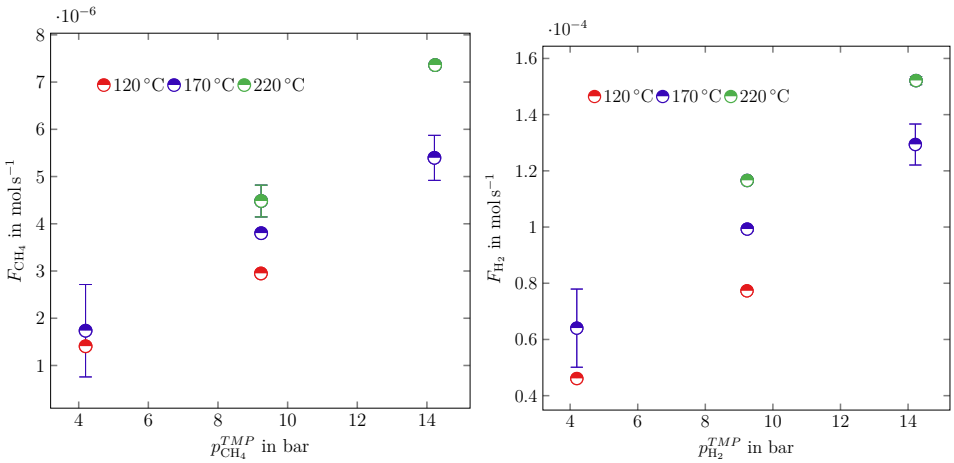

(a) Binary flow F_{CH_4} in mol s^{-1} of CH_4 over the transmembrane pressure p_i^{TMP} in bar.

(b) Binary flow F_{H_2} in mol s^{-1} of H_2 over the transmembrane pressure p_i^{TMP} in bar.

Fig. 4.5: Binary flows of CH_4 and H_2 over the feed pressure and with 120 °C, 170 °C and 220 °C. Experimental trial (3) from table 3.3.

compared to the binary permeances. An explanation could be that the larger CH_4 molecules block the pores for the H_2 molecules, so the permeance is lower.

In fig. 4.8a the behavior of the binary separation factor S_{H_2,CH_4} of H_2 over CH_4 is shown. The values for separation factor are calculated to be $S_{H_2,CH_4} = 110$ for $p^{feed} = 6$ bar and $T = 170$ °C and $S_{H_2,CH_4} = 90$ for $T = 120$ °C. It decreases with p^{feed} and temperature where at 220 °C and $p^{feed} = 15$ bar $S_{H_2,CH_4} = 60$. In contrast, the separation factor is compared to the ratio of pure components permeances like in eq. (2.5) $P^{pure}_{H_2}/P^{pure}_{CH_4}$ calculated from the pure component permeances in fig. 4.2b and fig. 4.1b. The ratio of pure permeances is higher than the separation factor by the factor of 2 and decreases with temperature.

The main findings of the described experiments are discussed in chapter 5 where the implications of the binary mass transport are described in more detail.

4.1.3 Binary permeation with water

As outlined in chapter 3, the measurement of H_2O permeance was affected by methodological factors and pumping system limitations, which hindered precise

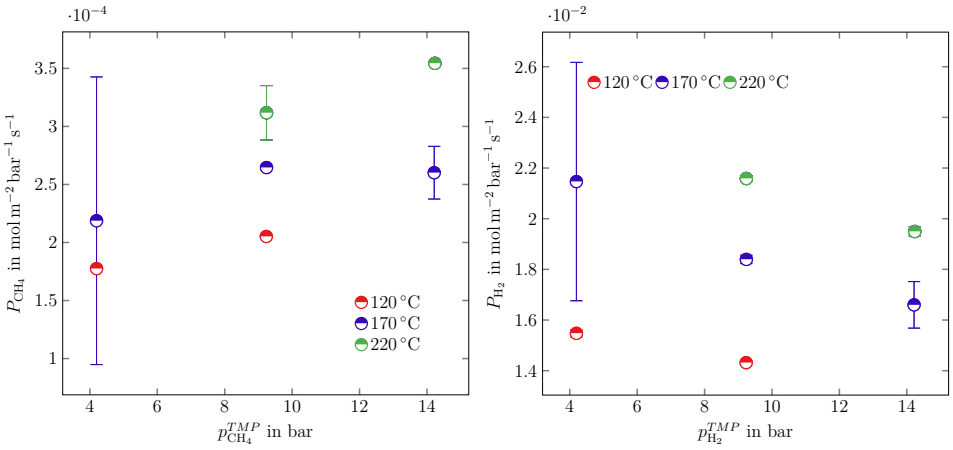

(a) Binary permeance P_{CH_4} in mol s^{-1} of CH_4 over the transmembrane pressure $p^{TMP}_{CH_4}$ in bar.

(b) Binary permeance P_{H_2} in mol s^{-1} of H_2 over the transmembrane pressure $p^{TMP}_{H_2}$ in bar.

Fig. 4.6: Binary permeance P_i in mol m^{-2} bar^{-1} s^{-1} over the transmembrane pressure p_i^{TMP} in bar of CH_4 and H_2. Experimental trial (3) from table 3.3.

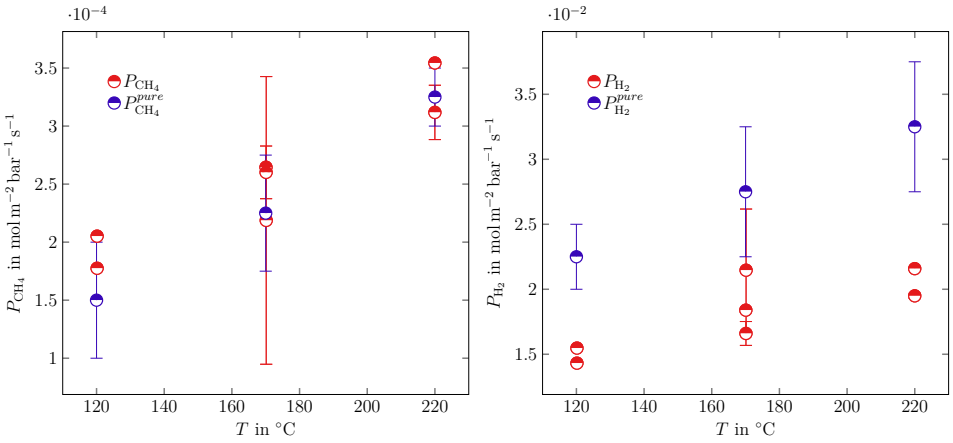

(a) Binary and pure component permeance P_{CH_4} in mol s^{-1} of CH_4 over the temperature T in °C.

(b) Binary and pure component permeance P_{H_2} in mol s^{-1} of H_2 over the temperature T in °C.

Fig. 4.7: Comparison of binary and pure permeances of CH_4 and H_2 in mol m^{-2} bar^{-1} s^{-1} over the temperature in °C. Experimental trial (3) from table 3.3.

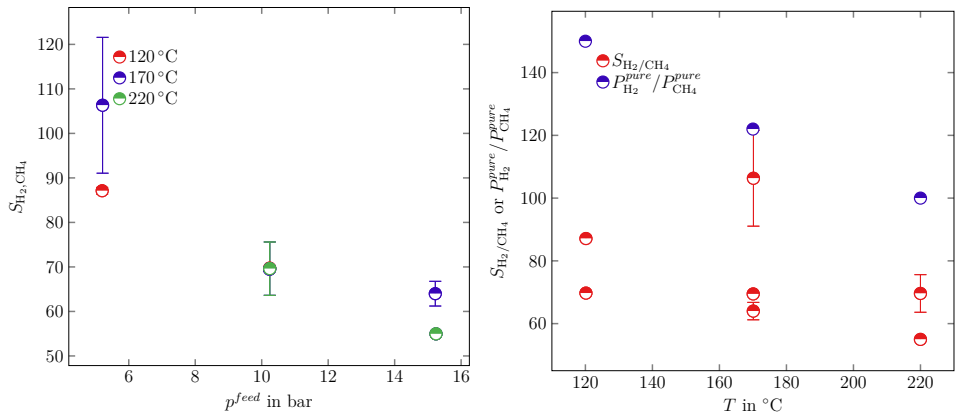

(a) Binary separation factor S_{H_2,CH_4} of H_2/CH_4 at 120 °C, 170 °C and 220 °C over the feed pressure p^{feed} in bar.

(b) Binary separation factor S_{H_2,CH_4} of H_2 and CH_4 over the temperature T compared to the ratio of pure component permeance P_{H_2}/P_{CH_4}.

Fig. 4.8: Binary separation factor S_{H_2,CH_4} of H_2 and CH_4 over feed pressure p^{feed} and temperature T in °C compared to the ratio of pure component permeance $P^{pure}_{H_2}/P^{pure}_{CH_4}$. Experimental trial (3) from table 3.3.

control of experimental conditions and the reduced pressure p^{red}, compare eq. (2.33). Despite these challenges, the data provide a fundamental understanding of binary separation involving H_2O vapor, offering valuable insights into its distinct transport behavior.

Binary permeation of methane and water The fig. 4.9 presents the binary permeances of H_2O and CH_4. The CH_4 permeance of approximately $10^{-4}\,mol\,m^{-2}\,bar^{-1}\,s^{-1}$ is significantly lower than that of water, with around $10^{-1}\,mol\,m^{-2}\,bar^{-1}\,s^{-1}$. Due to the inherent variability within the measurements, a clear influence of pressure on these binary permeances could not be definitively established or evaluated.

Binary permeation of hydrogen and water When looking at the permeance of H_2 and H_2O in fig. 4.10 in the binary mixture a different image is apparent. For low pressures and most of low temperature range the permeance of H_2 was not to be measured and then rises and at high pressures and temperatures of 170 °C and 220 °C up to values in the range of $10^{-2}\,mol\,m^{-2}\,bar^{-1}\,s^{-1}$. H_2O permeance in contrast shows a slight dependence towards the reduced pressure p^{red}.

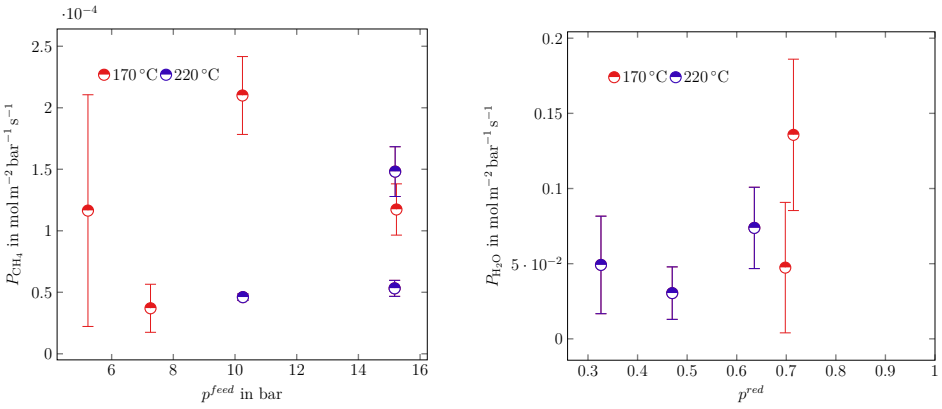

(a) Binary permeance P_{CH_4} in mol s^{-1} of CH_4 over the feed pressure p^{feed} in bar.

(b) Binary permeance P_{H_2O} in mol s^{-1} of H_2O over the feed pressure p^{feed} in bar.

Fig. 4.9: Binary permeances of CH_4 and H_2O in the binary mixture of CH_4 with H_2O. Experimental trial (5) from table 3.3.

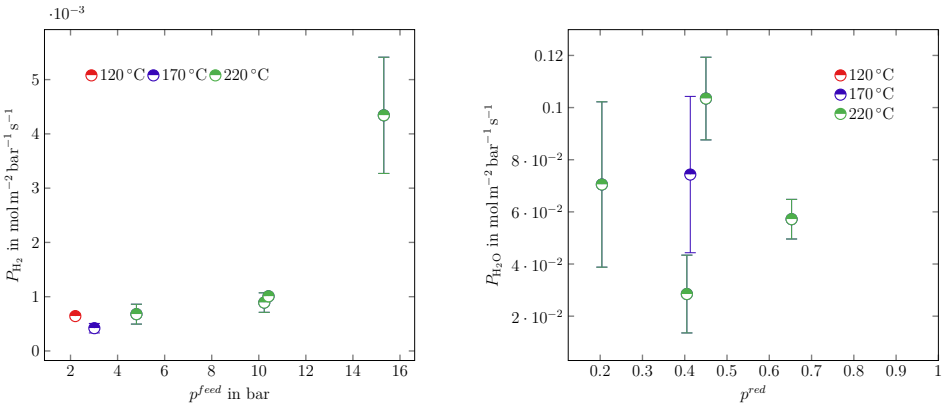

(a) Binary permeance P_{H_2} in mol s^{-1} of H_2 over the feed pressure p^{feed} in bar.

(b) Binary permeance P_{H_2O} in mol s^{-1} of H_2O over the feed pressure p^{feed} in bar.

Fig. 4.10: Binary permeances of H_2O and H_2 over the feed pressure. Experimental trial (4) from table 3.3.

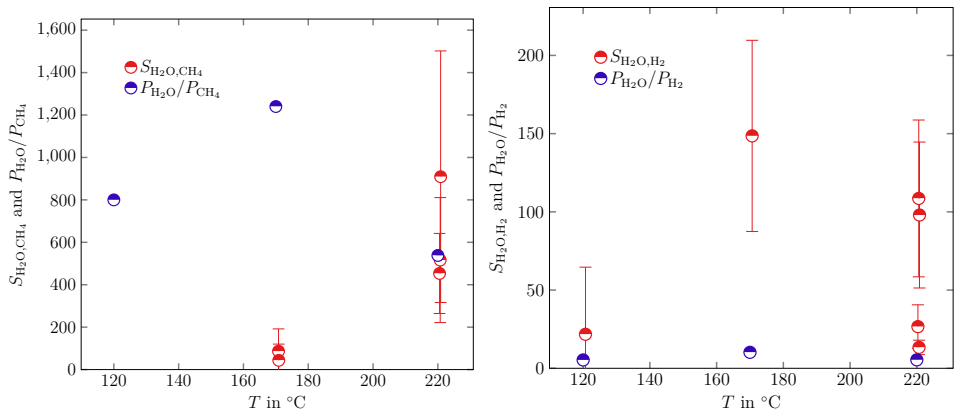

(a) Binary separation factors S_{H_2O,CH_4} over the temperature T compared to the ratio of single gas permeances P_{H_2O}/P_{CH_4}.

(b) Binary separation factors S_{H_2O,H_2} over the temperature T compared to the ratio of single gas permeances P_{H_2O}/P_{H_2}.

Fig. 4.11: Comparison of the binary separation factors of CH_4 to H_2O and H_2 to H_2O over the temperature in °C. Experimental trial (4) from table 3.3.

Binary results with water The section 4.1.3 presents a comparison of the measured separation factors ($S_{i,j}$) with the calculated ratios of pure permeances for the binary mixtures CH_4/H_2O and H_2/H_2O across the system temperature range. The difference between the two are explained in section 2.2.2.

While the inherent variability in the data influences the precision of interpretation, a comparison of the separation factor S_{H_2O,CH_4} and ratio of pure permeances reveals distinct trends. At 220 °C, both values are of the same order of magnitude. However, at 170 °C, the measured S_{H_2O/CH_4} is notably lower, by a factor of 100. These observations, despite their limitations, provide valuable insights for understanding the complexities of binary separation in such systems.

An interesting finding, illustrated in fig. 4.11b, is the significant discrepancy between the measured separation factor S_{H_2O/H_2} and the ratio of pure component permeances. Specifically, at 170 °C, S_{H_2O/H_2} reaches values up to 600, whereas the separation factor calculated from the pure H_2 and H_2O permeances (fig. 4.1b, fig. 4.4b) is close to 10. This substantial difference indicates that the presence of H_2O significantly hinders the permeation of H_2.

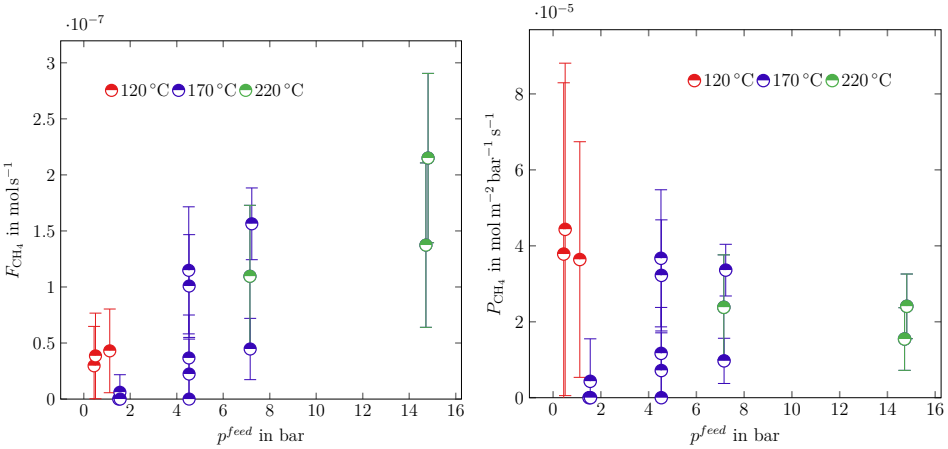

(a) Ternary flow F_{CH_4} in $\mathrm{mol\,s^{-1}}$ of CH_4 over the feed pressure p^{feed} in bar.

(b) Ternary permeance P_{CH_4} in $\mathrm{mol\,m^{-2}\,bar^{-1}\,s^{-1}}$ of CH_4 over the feed pressure p^{feed} in bar.

Fig. 4.12: Ternary flow in $\mathrm{mol\,s^{-1}}$ and permeation $\mathrm{mol\,m^{-2}\,bar^{-1}\,s^{-1}}$ of CH_4. Experimental trial (6) from table 3.3.

4.1.4 Ternary permeation

The ternary experiments were performed in the same temperature and absolute pressure ranges as the binary experiments in section 4.1.2, but with a mixture of H_2, CH_4, and H_2O close to the product gas composition downstream of a CO_2 methanation reactor as described in section 3.1.3. Water as a third component introduces a large margin of error in the experiments due to several factors discussed in section 3.1.4. Nevertheless, a major gap in the current literature is a comprehensive review of the permeation behavior of water through a carbon membrane at elevated temperatures with applicable gas compositions.

As can be seen from the comparison of the pure component permeation experiments (section 4.1.1) the three components H_2, CH_4 and H_2O show different permeation behavior as pure components and as shown in section 4.1.2 the interactions of the different components can be seen in the permeation of a binary mixture. In fig. 4.14 the flow of the three components over p^{feed} is shown, where H_2O has the highest flow rate with values of $10^{-4}\,\mathrm{mol\,s^{-1}}$. CH_4 has the lowest with values of $2 \times 10^{-7}\,\mathrm{mol\,s^{-1}}$ and H_2 is slightly higher with $5 \times 10^{-7}\,\mathrm{mol\,s^{-1}}$.

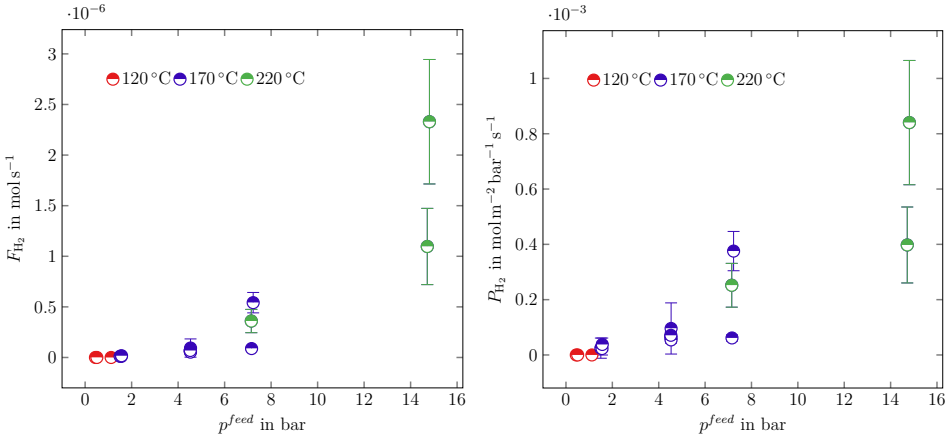

(a) Ternary flow F_{H_2} of H_2 over the feed pressure p^{feed}.

(b) Ternary permeance P_{H_2} in $\mathrm{mol\,m^{-2}\,bar^{-1}\,s^{-1}}$ of H_2 over the feed pressure p^{feed} in bar.

Fig. 4.13: Ternary flow F_{H_2} in $\mathrm{mol\,s^{-1}}$ and permeation P_{H_2} in $\mathrm{mol\,m^{-2}\,bar^{-1}\,s^{-1}}$ of H_2. Experimental trial (6) from table 3.3.

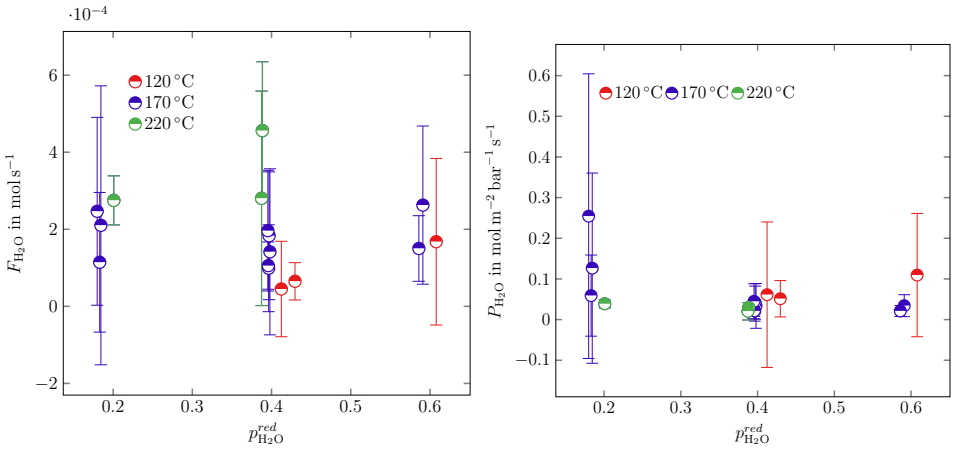

(a) Ternary flow F_{H_2O} in $\mathrm{mol\,s^{-1}}$ of H_2O over the reduced feed pressure p^{red}.

(b) Ternary permeance P_{H_2O} in $\mathrm{mol\,s^{-1}}$ of H_2O over the reduced feed pressure p^{red}.

Fig. 4.14: Ternary flow and permeation of H_2O over p^{red}_{H2O}. Experimental trial (6) from table 3.3.

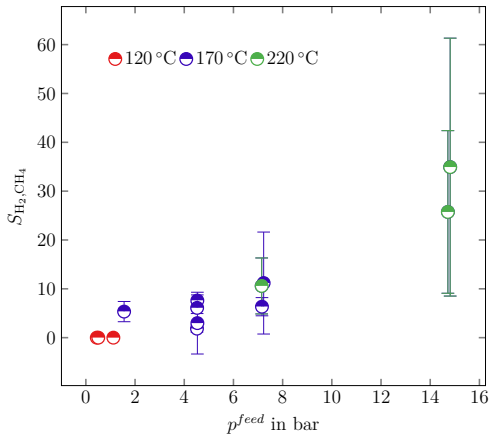

(a) Separation factor S_{H_2,CH_4} with ternary experiments over the feed pressure and with different temperature.

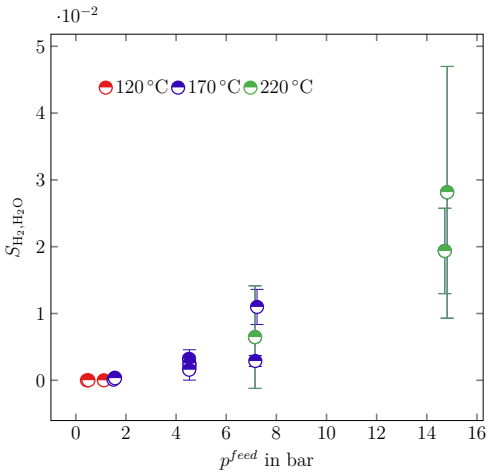

(b) Separation factor S_{H_2,H_2O} with ternary experiments over the feed pressure and with different temperature.

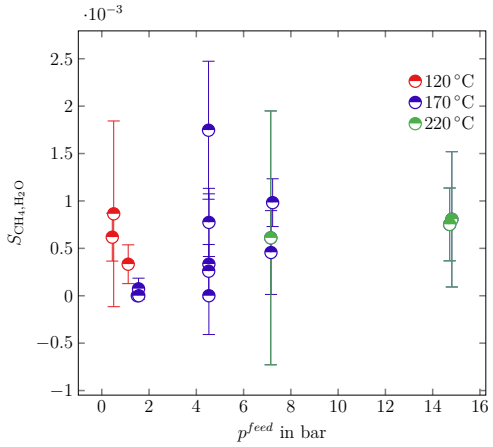

(c) Separation factor S_{CH_4,H_2O} with ternary experiments over the feed pressure and with different temperature.

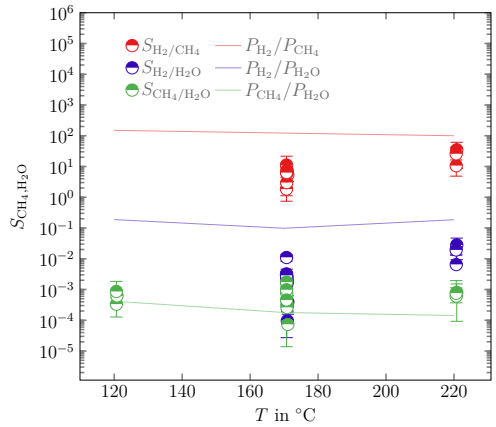

(d) Binary separation factor S_{H_2,CH_4} and comparison of pure component's permeance ratio $P_{H_2}^{pure}/P_{CH_4}^{pure}$ over the temperature T in °C.

Fig. 4.15: Binary separation factor S_{H_2,CH_4} at 120 °C, 170 °C and 220 °C over the feed pressure p^{feed} in bar and temperature T at the ternary permeation experiments. Ternary experimental trial (6) from table 3.3.

The same picture is seen when looking at the permeance of the three components in the ternary mixture.

The calculated separation factors can be seen in fig. 4.15a, fig. 4.15b and fig. 4.15c. The difference between binary and ternary separation factor is apparent when looking at the fig. 4.15a, where the separation factor is basically 0, (or inf), at low p^{feed}. This can be seen by looking at the flow of CH_4 (fig. 4.12b) and H_2 (fig. 4.13b). The permeance of CH_4 is larger than that of H_2 at low p^{feed} and only with increasing p^{feed} the permeance of H_2 increases and a permeance phenomenon comparable to that of binary permeation is visible. When the flow of the third component H_2O increases with increasing p^{feed} and T, the separation factor exceeds unity and increases up to $S_{H_2,CH_4} = 30$.

The separation factor of CH_4 over H_2O is shown in fig. 4.15c. Due to the high margin of error for water permeation and low, highly variable CH_4 permeance, a physically reasonable conclusion cannot be drawn. Values are on the order of 1E−3, as indicated by the permeance differences in fig. 4.12b and fig. 4.14b.

In fig. 4.15d the ternary separation factors $S_{i,j}$ are compared to ratios of pure components permeations P_i/P_j, which are calculated from pure component permeances (fig. 4.1b and fig. 4.4b) over temperature T. The CH_4 separation factor in the presence of H_2O is consistent with pure component permeances, similar to the binary case in fig. 4.6a where CH_4 permeance is unaffected by H_2.

The mean standard deviations of flow were $\sigma_{H_2} = 1.57 \times 10^{-4}\,\mathrm{mol\,min^{-1}}$, $\sigma_{CH_4} = 1.77 \times 10^{-5}\,\mathrm{mol\,min^{-1}}$, and $\sigma_{H_2O} = 1.96 \times 10^{-2}\,\mathrm{mol\,min^{-1}}$. The measurement error for H_2O is two orders of magnitude greater than for the other gases.

4.2 Adsorption

Adsorption isotherms are central to understanding the interaction between adsorbates and adsorbents, provide crucial information about the capacity and affinity of the adsorbent for the adsorbate at varying equilibrium concentrations. In combination with the pure component permeation experiments mentioned in the previous section, we can calculate Maxwell-Stefan surface diffusion coefficients. These coefficients, in turn, facilitate the modeling of binary and ternary mass transport

Tab. 4.1: Estimated parameters of the *Langmuir*, *Freundlich* and *Toth* isotherms for H_2 and CH_4 at temperatures of 90 °C, 110 °C and 120 °C.

Langmuir and Freundlich parameters.

Component	T °C	b_i^l bar^{-1}	$q_{i,sat}^l$ $\mathrm{mmol\,g}^{-1}$	R^2	K_i^{fr}	n_i^{fr}	R^2
H_2	90	0.512	0.093	0.98	0.132	0.302	0.993
H_2	110	0.513	0.04	0.915	0.069	0.409	0.92
H_2	120	0.407	0.03	0.147	0.007	1	0.138
CH_4	90	1.486	0.117	0.984	0.413	0.296	0.985
CH_4	110	1.442	0.067	0.993	0.253	0.386	0.997
CH_4	120	1.399	0.06	0.993	0.253	0.366	0.998

Toth parameters.

Component	T °C	K_i^t bar^{-1}	$q_{i,sat}^t$ $\mathrm{mmol\,g}^{-1}$	f_i^t	R^2
H_2	90	1	0.262	1.377	0.991
H_2	110	0.126	0.269	2	0.919
H_2	120	0.03	1	0.407	0.147
CH_4	90	0.117	1	1.486	0.984
CH_4	110	0.096	0.605	1.923	0.996
CH_4	120	0.108	0.531	2	0.998

and provide insight into complex adsorption processes, which will be done in the subsequent section.

First the results of the adsorption experiments are presented and briefly discussed. Then parameter of different adsorption isotherms, mentioned in chapter 2 will be estimated to the adsorption data and the most suited for the modeling approach will be used.

The results of the adsorption measurements of H_2, CH_4 and H_2O are presented in table 4.1 and table 4.2 in order to discuss the differences between the data. The most applicable adsorption isotherms for each component are estimated with the data and presented.

The presented data adsorption loading of H_2 in fig. 4.16a is the lowest of the measured components with a maximum surface loading at 45 bar at 90 °C of $q_i = 0.4\,\mathrm{mmol\,g}^{-1}$ and with a decrease in adsorbed amount with respect to the temperature. At 120 °C

Tab. 4.2: Estimated parameters of the *Langmuir*, *Dubinin Radushkevich* and *Do and Do* isotherms for H_2O at temperatures of 25 °C, 50 °C and 90 °C.

Langmuir and Dubinin-Radushkevich parameters.

T °C	$q_{i,sat}^{l}$ mmol g^{-1}	b_i^l bar^{-1}	R^2	$q_{i,sat}^{DR}$ mmol g^{-1}	E_i kJ mol^{-1}	R^2
25	134.72	2.19	0.048	5.3389	237.585	2.70E − 02
50				1.807	968.51	3.90E − 02
90	8.20E − 03	0.46	0.024	0.0016	1353.94	0.055

Do and Do parameters.

T °C	$C_{\mu,s}$ mmol g^{-1}	S_0 kJ mol^{-1}	K_f mmol g^{-1}	K_μ^l kJ mol^{-1}	R^2
25	4.36E + 01	6.39E + 01	2.01E + 00	5.38E + 02	0.028
50	4.93E − 09	7.57E − 01	2.43E + 01	1.89E − 07	0.019
90	0.00E + 00	4.63E − 01	8.08E + 07	3.62E-04	0.049

at 45 bar the adsorbed amount is $q_i = 0.2\,\text{mmol g}^{-1}$. With the measurements at 120 °C a high margin of error is visible, since some outliers are visible at 20 bar and 40 bar. Comparing the slope and structure of the isotherm with fig. 2.6, the adsorption of H_2 on the nanoporous carbon seems to have a *Type I* shape. As can be seen with the three temperatures all three estimated adsorption isotherms show a sensible behavior, where the *Freundlich* isotherm at 120 °C is slightly off at higher partial pressures.

With CH_4 in fig. 4.16b the adsorbed amount is higher with the highest being $q_i = 1.2\,\text{mmol g}^{-1}$ at 90 °C and 45 bar. The decrease of adsorbed amount with temperature is visible as well where at lower pressure ranges the amount between 110 °C and 120 °C is within the margin of error of the device. Again comparing the fig. 2.6, adsorption of CH_4 looks like a *Type I* shape. Due to the high temperature and the consequent low overall adsorbed amount the shape might not be as significant as at lower temperatures. The estimated adsorption isotherms are all in a viable range but at 120 °C the *Langmuir* isotherm shows the best fit, since it is clearly separated from the other temperature points.

With H_2O the adsorption shows a different image in fig. 4.16c. The shape in fig. 2.6 is comparable to *Type II* at 25 °C. To be comparable the adsorption isotherm is not plotted over the absolute pressure but over the reduced pressure p^{red} of each temperature. With the other temperatures the adsorption is not strong enough and they seem to be *Type I* adsorption isotherms. Nevertheless the maximum amount of adsorption shown with H_2O is with $q_i = 5.8\,\mathrm{mmol\,g^{-1}}$ but is decreasing drastically with temperature. At 90 °C the adsorbed amount is at $q_i = 1.304\,669 \times 10^{-3}\,\mathrm{mmol\,g^{-1}}$.

Different adsorption isotherms are required, as discussed in section 2.4.2. The *Do and Do* isotherm best captures the physical nature of water adsorption on carbon. The *Dubinin Radushkevich* isotherm describes vapor adsorption on nanoporous materials, while the simpler *Langmuir* isotherm offers a straightforward and computationally efficient model.

The fig. 4.16c shows that the *Do and Do* isotherm consistently describes the adsorption data across all three temperatures measured. The *Dubinin Radushkevich* isotherm is applicable only at 50 °C. The *Langmuir* isotherm describes data at 25 °C and 90 °C with reasonable accuracy, exhibiting a root mean square error of 4.78 % at 25 °C. The isosteric heat of adsorption Q_{st} for H_2 and CH_4 was calculated using the simplified *Langmuir* isotherm described in eq. (2.37). The values were calculated to be at: $Q_{st}^{H_2} = 11.03\,\mathrm{kJ\,mol^{-1}}$ and $Q_{st}^{CH_4} = 27.44\,\mathrm{kJ\,mol^{-1}}$. Calculation of $Q_{st}^{H_2O}$ was not possible, precluding a physically sensible extrapolation of its adsorption data as described in section 3.2.3. The next section incorporates measurement error into parameter ranges for the selected adsorption isotherms to support further calculations. Using the standard deviation and Monte Carlo simulation, the error impact is visualized for the most suitable isotherms of the three components. In fig. 4.17a, the error at 120 °C is evident, but the *Langmuir* isotherm remains usable, unlike other isotherms that fail to converge. The fig. 4.17b shows a smaller error margin, allowing all three isotherms to be applied. For H_2O in fig. 4.17c, only data at 50 °C and 90 °C are usable. Adsorption at 90 °C is negligible, making isosteric heat extrapolation unreliable. In this Figure data at 90 °C must be adapted empirically for higher temperatures, as no physical basis exists for extrapolation.

After analyzing the experiments, the *Langmuir* isotherm is chosen for all three components due to:

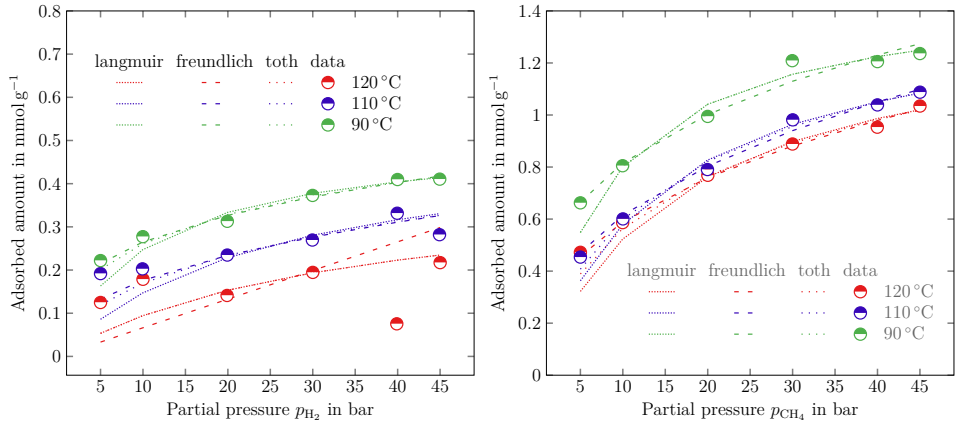

(a) Adsorbed amount of H_2 at 120 °C (red), 110 °C (blue) and 90 °C (green).

(b) Adsorbed amount of CH_4.

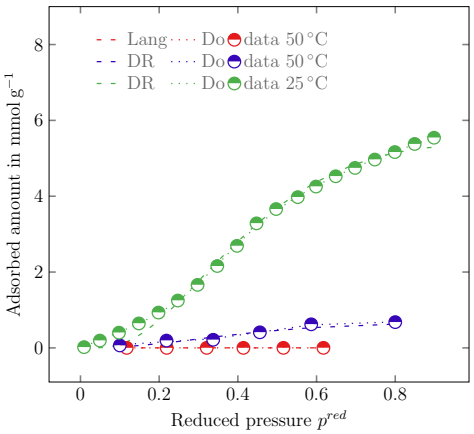

(c) Adsorbed amount of H_2O over the reduced pressure p^{red}.

Fig. 4.16: The adsorption of H_2, CH_4 at 120 °C (red), 110 °C (blue) and 90 °C (green) with the use of *Langmuir*, *Freundlich* and *Toth* isotherm. H_2O at 25 °C, 50 °C and 90 °C in comparison with *Do and Do* and *Dubinin Rudushkevich* isotherms..

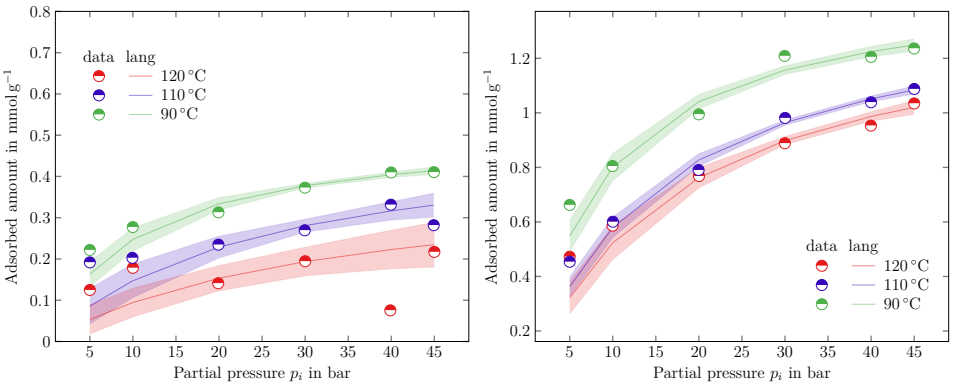

(a) Adsorbed amount of H_2 at 120 °C (red), 110 °C (blue) and 90 °C (green). The calculated *Langmuir* isotherm is shown by the solid line. The calculated Monte Carlo simulation deviation is shown in transparent colors.

(b) Adsorbed amount of CH_4 at 120 °C (red), 110 °C (blue) and 90 °C (green). The *Langmuir* isotherm was used to estimate the the values. The values of the same isotherm with the Monte Carlo simulation are shown in transparent colors.

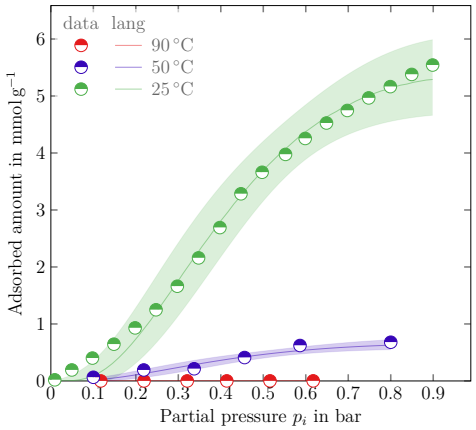

(c) Adsorbed amount of H_2O at 90 °C (red), 50 °C (blue) and 25 °C (green). The *Langmuir* isotherm was used to estimate the the values. The values of the same isotherm with the Monte Carlo simulation are shown in transparent colors.

Fig. 4.17: Comparison of the estimated adsorption isotherms with the use of monte carlo simulation to estimate the imposed error on the calculation.

- Lowest error margin for CH_4 and H_2
- Acceptable error margin for H_2O
- The *extended Langmuir* model's common use in binary and ternary systems, offering low convergence and computational issues despite its complexity

Although the use of *Do and Do* (Do et al., 2009) would be preferable, the *Langmuir* isotherm shows a small margin of error and is able to describe the highest temperature with 90 °C. The description of a different adsorption isotherm like the *Do and Do* would impose an additional numerical problem onto the model and thus would create more problems than solving uncertainties.

Based on the presented experimental results with pure component adsorption experiments and pure, binary and ternary permeation experiments, the results of the modeling approach are presented in the following section.

The H_2O experiments used lower temperatures compared to H_2 and CH_4. This results in a greater spacing between data points, potentially compromising the accuracy of the measurements and the interpretation of the results. The physical properties of water, particularly its polarity, result in a more complex adsorption behavior compared to H_2 and CH_4. This complexity makes it difficult to model and analyze the experimental data for H_2O adsorption. In addition to temperature and molecular properties, other factors can influence H_2O adsorption. These include the purity of the water, the pore size of the adsorbent material, and the specific measurement methods used.

4.3 Modeling

As described in fig. 3.7 the pure adsorption and permeation experiments of all three components are combined to calculate the single component surface diffusion coefficients $\mathcal{D}_i^s$ for the nanoporous carbon layer.

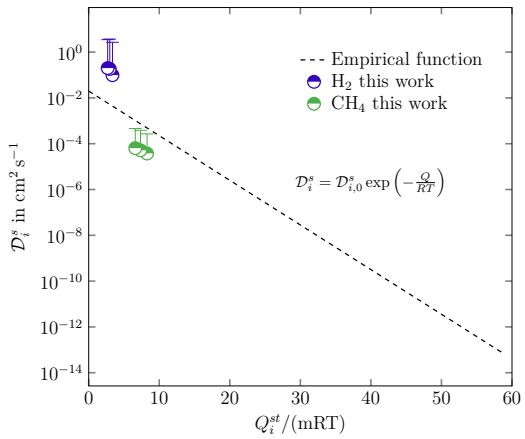

Fig. 4.18: $\mathcal{D}_i^s$ over $Q_i^{st}/(mRT)$. The empirical function is based on (Yang, 1987) and (Gilliland et al., 1974). Disclaimer: The negative error bar is hidden for better legibility.

4.3.1 Single component diffusion coefficients

Using adsorption data up to 120 °C, temperature extrapolation, and permeation experiments between 120 °C and 220 °C, the Maxwell-Stefan diffusion coefficients $\mathcal{D}_i^s$ were calculated via the three-layer model. The coefficients for H_2 and CH_4 at various temperatures are listed in table 4.5.

For H_2, $\mathcal{D}_i^s$ ranges from $9.81 \times 10^{-6}\,m^2\,s^{-1}$ at 120 °C to $2.01 \times 10^{-5}\,m^2\,s^{-1}$ at 220 °C. For CH_4, it increases from $3.73 \times 10^{-9}\,m^2\,s^{-1}$ to $6.39 \times 10^{-9}\,m^2\,s^{-1}$ over the same range. Both components' diffusion coefficients rise with temperature.

Plotting $\mathcal{D}_i^s$ against the isosteric heat of adsorption Q_i^{st} allows comparison with an empirical correlation from (Yang, 1987). As shown in fig. 4.18, the data for H_2 and CH_4 follow the same physical trend and generally agree with the correlation.

4.3.2 Binary permeation results

The developed binary model of H_2 and CH_4 is evaluated at the same conditions like the binary permeation experiments were conducted. With this method the model can be compared and validated for the binary description of mass transport.

Tab. 4.5: Calculated Maxwell-Stefan Diffusion coefficients of H_2 and CH_4 at 120 °C, 170 °C and 220 °C in $m^2\,s^{-1}$. The error range shown represents the standard deviation of the calculated values with the Monte Carlo simulation.

Component	@120.00 °C $m^2\,s^{-1}$	@170.00 °C $m^2\,s^{-1}$	@220.00 °C $m^2\,s^{-1}$
H_2	$(9.81 \pm 2.55) \times 10^{-6}$	$(1.84 \pm 0.34) \times 10^{-5}$	$(2.01 \pm 0.49) \times 10^{-5}$
CH_4	$(3.73 \pm 0.62) \times 10^{-9}$	$(5.17 \pm 0.35) \times 10^{-9}$	$(6.39 \pm 0.60) \times 10^{-9}$
H_2O	$(5.67 \pm 2.95) \times 10^{-3}$	$(5.55 \pm 2.09) \times 10^{-3}$	$(7.98 \pm 1.95) \times 10^{-3}$

When comparing the results of the permeation to another, several things are visible. In fig. 4.19a the permeance in $mol\,m^{-2}\,bar^{-1}\,s^{-1}$ are plotted over the T in °C. The results from the model show a higher permeance than the one from the experiments, but the values are in the same order of magnitude. For CH_4 the picture is different, since the values of the model rather underestimating the experimental shown permeances, but the values are in the same order of magnitude as well. The dependency of the permeance towards the temperature that is measured in the experiments is not modeled, since the values rather drop. This effect is discussed in chapter 5.

While a minor overestimation of one permeance and a slight underestimation of the other may not be significant, the model indicates that the separation factor of the two components is represented by a value that is ten times higher, as shown in fig. 4.19c. The reasons behind this physical behavior are explored in chapter 5.

4.4 Introduction of parameters for confined space and optimization

As outlined in section 3.4, the discrepancies between the modeling results and experimental values, as shown in section 4.1.3, were anticipated. To address these differences, the confinement factor ζ_i for confined spaces was manually adjusted according to (Bhatia et al., 2011). For pore diameters of $d_p = 0.75\,nm$ and $d_p = 0.6\,nm$, ζ_i was set to 0.45 and 0.23, respectively. For the slit pore carbon membrane with a diameter of $d_p = 0.42\,nm$, ζ_i was set to 0.1. These values were chosen to match experimental data and do not have direct physical significance.

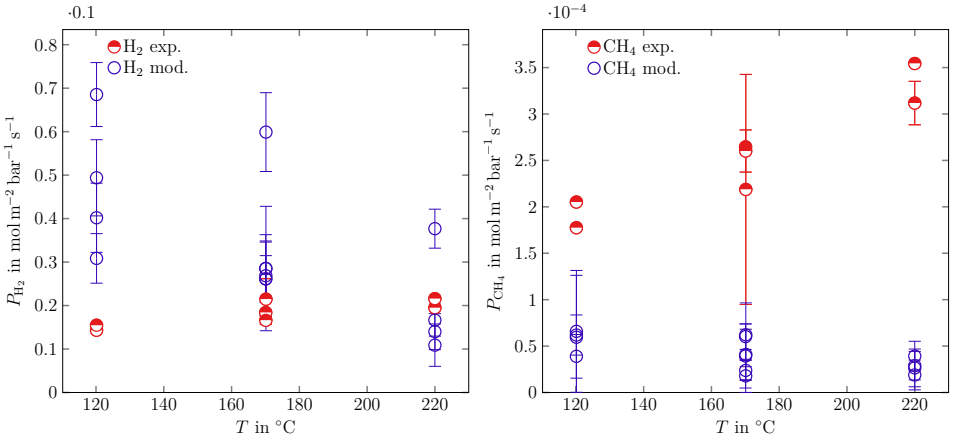

(a) Modeled binary permeance of H_2 compared to the experimental values.

(b) Modeled binary permeance of CH_4 compared to the experimental values.

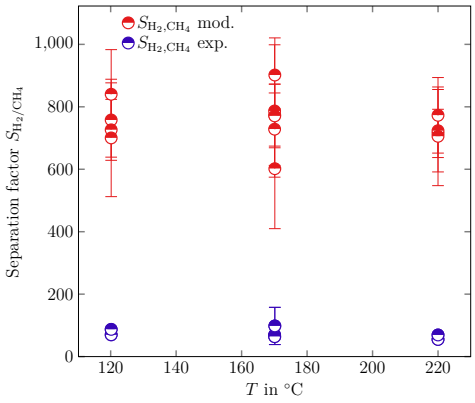

(c) Binary separation factor S_{H_2,CH_4} modeled and experimental.

Fig. 4.19: Binary permeance P_i in mol m^{-2} bar^{-1} s^{-1} over the temperature in °C of CH_4 and H_2.

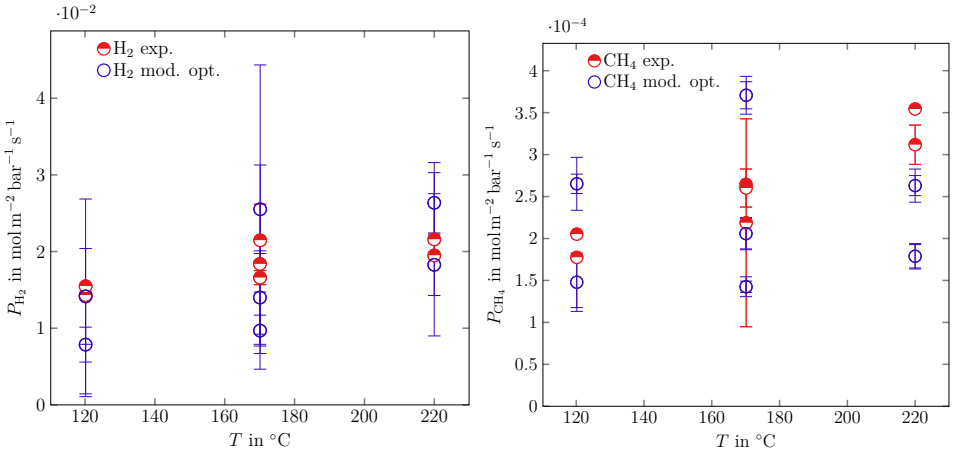

(a) Binary permeance of H_2 with optimized parameter ϕ_i.

(b) Binary permeance of CH_4 with optimized parameter ϕ_i.

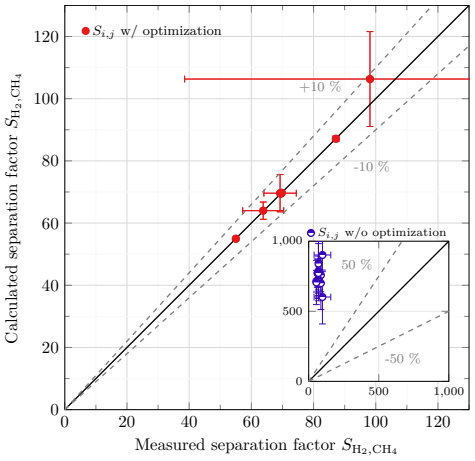

(c) Experimental and modeled binary separation factors of H_2/CH_4 compared to the modeled separation factor with the optimized parameters using a parity plot.

Fig. 4.20: Results for the optimized parameters comparing to the experimental results and the not optimized parameters in fig. 4.19.

Introducing the confinement factor resulted in a reduction of the calculated mass transport, decreasing the overall deviation to approximately 11.

Given the positive temperature dependence observed in the experimental results, the parameter ϕi was determined by optimizing all experimental data. The estimated values were $\phi_{i=1} = 0.0861$ for H_2 and $\phi i = 2 = 1.1103$ for CH_4. The combination of the optimized ϕ_i values with the confinement factor ζ_i significantly improved the agreement between the model and experimental results, reducing the deviation in modeled permeation for both H_2 (fig. 4.20a) and CH_4 (fig. 4.20b). Furthermore, the introduction of a positive dependence on the logarithmic temperature term $\ln(T)$ justified the observed increase in permeability, aligning the model more closely with experimental trends.

Before using the optimized parameters, the separation factor $S_{H_2,\,CH_4}$ showed poor agreement, as seen in fig. 4.19. This is illustrated in the parity plot in fig. 4.20c, where the small blue subfigure shows calculated and measured values that do not align well and fall outside the 50 % error margin. In the same figure, the separation factor $S_{H_2,\,CH_4}$ with optimized parameters is shown in red, with agreement between measurements and model results within a tighter 10 % margin. This effect is shown in fig. 4.20a and fig. 4.20b in more detail.

4.5 Process variable variation

The variable variation in section 3.4 was conducted by increasing the system temperature from 220 °C to 340 °C, followed by varying the feed composition using the developed and optimized model. The details of this variation are summarized in table 3.5. The impact on the separation factor S_{H_2,CH_4} is illustrated in fig. 4.21a.

The fig. 4.21a presents three data sets: experimental results (red circles), optimized model predictions (blue circles), and extrapolated values (green circles). The separation factor S_{H_2,CH_4} shows a slight decrease as temperature increases from 220 °C to 500 °C, which is likely due to fixed model parameters that do not fully capture dynamic changes occurring at higher temperatures. This trend is confirmed by the extrapolated data.

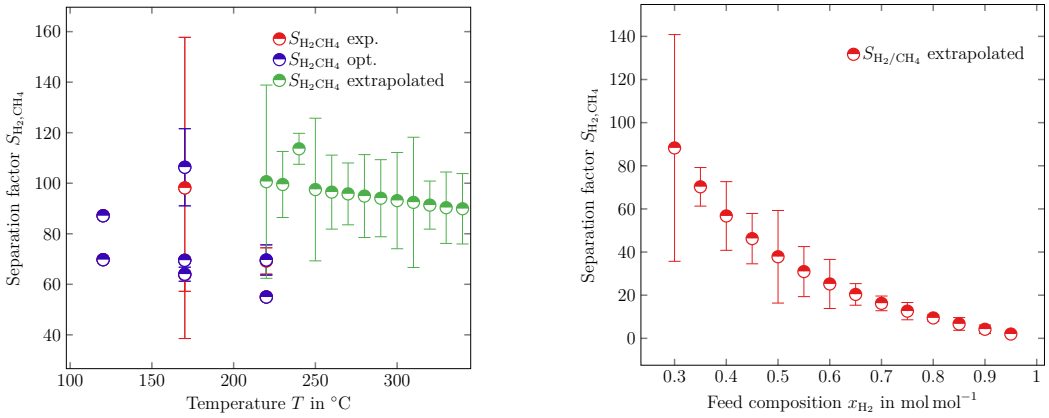

(a) Separation factor S_{H_2,CH_4} measured (exp.), calculated (opt.) and extrapolated over the temperature up to 340 °C.

(b) Feed composition X_{H_2} and the extrapolation of the corresponding separation factor S_{H_2/CH_4}.

Fig. 4.21: Results of the extrapolation of feed composition and temperature shown as a calculation of the separation factor S_{H_2,CH_4}.

Additionally, as the H_2 concentration in the feed increases, the separation factor decreases (see fig. 4.21b). This behavior is attributed to continued CH_4 diffusion through the membrane despite the higher H_2 levels, reducing overall selectivity. These findings highlight the complex interplay between temperature, feed composition, and membrane transport properties in determining separation performance.

5 Discussion

This chapter discusses the interpretation and significance of the results obtained from the experimental study of methane, hydrogen, and water permeation. The research took a diverse approach, including the measurement of pure component, binary, and ternary permeation adsorption isotherms. These measurements provided insight into the individual and combined behavior of these molecules within the selected material.

A mass transport model based on the Maxwell-Stefan surface diffusion and Knudsen diffusion descriptions was developed to mathematically represent the permeation process. This model was used to calculate the Maxwell-Stefan surface diffusion coefficients for the pure components. The calculated coefficients are used to estimate the binary mass flows through the membrane layer.

This model allows a deeper understanding of the underlying mechanisms governing the transport of CH_4, H_2, and H_2O through the material. By analyzing the experimental data and the predictions of the model, this chapter discusses the main results of the research.

5.1 Interpretation of findings

In this section the presented results in chapter 4 are discussed and compared to one another.

5.1.1 Permeation experiments

The pure permeance of H_2 and CH_4 shows a linear dependence on temperature, but H_2O shows a drop in permeance from 170 °C to 220 °C with the described variance of calculated values. This can be explained by the adsorption behavior of water, which is related to the reduced pressure, which is a function of T.

In fig. 4.6 values in the range of $2 \times 10^{-4}\,\mathrm{mol\,m^{-2}\,bar^{-1}\,s^{-1}}$ are shown. The permeances of H_2 with values of $2 \times 10^{-2}\,\mathrm{mol\,m^{-2}\,bar^{-1}\,s^{-1}}$ are two orders of magnitude higher .

The first behavior can be explained by the different adsorption behavior of the two components caused by the increasing feed pressure. This can be seen by examining at the adsorption isotherms of the two components in fig. 4.16a and fig. 4.16b. Hydrogen appears to diffuse at these temperatures with less influence from adsorption when considering the pure component. In binary permeation, the stronger adsorption of CH_4 may hinder H_2 permeation, reducing its permeance. However, in pure component experiments, this effect is absent or slightly positive.

This difference arises from the discrepancy between measured separation factors and the ratio of pure component permeances. This highlights the importance of detailed analysis of binary permeance and the development of a mass transport model, as conducted in this work.

Similarly, in binary permeation experiments with H_2O, pore blockage is evident in section 4.1.3. The measured separation factor S_{H_2O,H_2} is about 100 times higher than the ratio of pure permeances S_{H_2O}/S_{H_2}, indicating pore blockage that favors water separation factor. This effect is not observed for the CH_4 and H_2O pair in the same figure.

The permeance of the different species in the ternary permeation experiments do not show any dependence towards the temperature or the feed pressure. The comparison of the separation factors of the ternary permeation experiments in section 4.1.3 shows an interesting result, where the presence of water increases the separation factor of H_2O over H_2 by a factor of about 100. Even with the described high margin of error, this is significant. One explanation may be the blocking of membrane pores by water vapor. This effect is not visible with CH_4 permeance, which may be due to the

different kinetic diameters of the two molecules; H_2 has a kinetic diameter of 289 pm, while CH_4 has a larger kinetic diameter of 380 pm. Consequently, as indicated by the permeances of CH_4, the pore diameter of 0.4 nm (or 400 pm) imposes a significant resistance to mass transport.

One key finding of this study is the comparison of the binary and ternary separation factors of H_2, CH_4 and H_2O in section 4.1.2 and section 4.1.4. Comparing the ratio of pure component permeances to the measured separation factors $S_{i,j}$ shows an interesting picture in fig. 4.15d and fig. 4.19c. The binary separation factor of H_2 and CH_4 is lower than expected from the pure component permeances and the calculated separation factor. This is due to the fact that CH_4 is permeating with the same rate in the binary case as in the pure component case and H_2 is hindered by the presence of CH_4 by a factor of 50 % as can be seen on fig. 4.8b.

The same is true for the comparison of the calculated separation factors to the ternary permeation in fig. 4.15d, where the expected separation factor would be higher for H_2/CH_4 with the presence of H_2O and CH_4. For CH_4/H_2O the separation factor and the ratio of pure permeances is in the same order of magnitude. For the separation of H_2 from H_2O the measured separation factors are higher than what could have been expected from the ratio of pure component permeances, since blockage effects were observed.

5.1.2 Adsorption

The adsorption experiments were presented along with the estimated parameters of the adsorption isotherms in table 4.1 and table 4.2. The adsorption isotherm estimations were performed for three isotherms for H_2 and CH_4. The margin of error seem to be within the acceptable range, but when looking at the *Toth* isotherm the R^2 values are most in an exceptional good range. Nevertheless, the values for $q_{i,sat}$ and f_i were estimated to be at values which have no physical sensible value. This can be due to the fact, that the *Toth* isotherm is an extension of the *Langmuir* isotherm and this thus the three parameter model is not applicable. In addition the three parameter model is harder to be estimated using only six points of measurement.

When comparing the results in table 4.1 to the literature values in fig. 2.8, notably, the difference between the adsorption constants of CH_4 and H_2 observed in this study

is smaller than reported in the literature (compare (Choi et al., 2003; Hao et al., 2014; Ito et al., 2013; Men'shchikov et al., 2021; P. Marco-Lozar et al., 2012; Rother and Fieback, 2013; Takagi et al., 2004; Voskuilen et al., 2012)). This discrepancy can be attributed to the small pore size (0.4 nm) of the nanoporous carbon. This limited size hinders the diffusion of the relatively large CH_4 molecule (kinetic diameter: 0.38 nm), potentially leading to reduced adsorption and hindered permeability compared to the smaller H_2 molecule (kinetic diameter: 0.289 nm). Additionally, the low saturation capacities ($q_{i,sat}$) likely stem from the limited micropore volume.

The isotherm parameters for H_2O in table 4.2 are more difficult for interpretation, since the maximum temperature is limited to 90 °C and the values for the maximum adsorbed concentration $q_{i,sat}$ are decreasing rapidly until a point where the adsorbed amount can not be extrapolated. As can be seen in fig. 4.16 the *Langmuir* isotherm shows for alle three components and the different temperatures a good fit, with the exception of H_2O at 50 °C, when comparing the isotherm to the Langmuir.

5.1.3 Modeling

The developed model was implemented for the pure permeation, in order to calculate the Maxwell-Stefan surface diffusion coefficients $\mathcal{D}_i^s$. These values are compared to an empirical correlation from (Yang, 1987) in fig. 4.18.

Here revisiting the hypotheses from chapter 1:

Hypothesis 1 Maxwell-Stefan surface diffusion coefficients can be calculated from experimental data and applied in a binary mass transport model that is capable of predicting binary permeation measurements.

The calculated values of $\mathcal{D}_i^s$ show a similar behavior and the values are within a close range to the empirical data fit. The calculated $\mathcal{D}_i^s$ can be used for the binary model, where the modeled and measured permeation are close to one another. Followed by these findings the developed modeling approach and the presented model can calculate binary permeation of H_2 and CH_4 within an acceptable margin of error. With the presented results the adsorption isotherms of two important gases for the biorefiniery industry H_2 and CH_4 are measured for temperatures important to several applications as discussed in chapter 2. The calculated Maxwell-Stefan

surface diffusion coefficients can be used in different extended modeling approaches and were compared to an applied empirical correlation. The findings with water were more complicated, since the margin of error is higher of about two orders of magnitude, the physics of the adsorption of water on nanoporous carbon is significantly more complicated and the permeation experiments with water were showing an increasingly high margin of error.

The margin of error is increasing for the ternary model, where some additional simplifications and assumption were needed to calculate the permeation and based on the complicated water adsorption values the validity of these values are somewhat questionable. Nevertheless the presented approach was not able to converge to a suitable solution, but based on the high margin of error for the water permeation calculations and the adsorption isotherms, which on one side show a high margin of error and are on the other side not usable for any kind of extrapolation, the hypothetical results from the ternary model would have been even calculated with an higher error than the binary model and thus this will be discussed in chapter 6.

Revisiting the second hypothesis from chapter 1:

Hypothesis 2 The accuracy of the calculated Maxwell-Stefan surface diffusion coefficients, which are subject to uncertainty due to temperature extrapolation, can be significantly improved by applying a simple temperature-dependent correction function.

This can be answered with the relatively low margin of error present in fig. 4.19. When looking at the high margin of error and the assumptions and simplifications mentioned in section 3.2.4 this is within a good applicable range. Large influence would have been the extrapolation of the adsorption isotherms, which introduces an unquantifiable error in the calculations. The introduction of the confined space and the temperature dependent function in section 4.4 proves that this approach was very worthwhile. In fig. 4.20c this is shown with a parity plot and the difference before and after the usage of the optimized parameters is significant.

With this validated model, variable variation can be employed to predict membrane performance under process conditions closer to industrial applications, as shown in section 4.4 with varied parameters listed in table 3.5.

As can be seen on fig. 4.21 as extrapolated up to 340 °C, the membrane's separation factor remains similar, with only a slight decrease in performance. This suggests that membranes exhibiting separation factors around 100 are still suitable for such elevated-temperature systems.

The further implications of the study are presented in the next section.

5.2 Implications of findings

Calculated Maxwell-Stefan surface diffusion coefficients ($\mathcal{D}_i^s$) for H_2 and CH_4 show good agreement with existing correlations, suggesting that they can be used for further modeling (partially supporting hypothesis 2). This implies that these coefficients can be used in various modeling approaches to understand and predict gas behavior within the membrane.

The measurement of water (H_2O) adsorption and permeation proved to be more complex due to high error margins and the complicated physics involved. This highlights the need for further research on water interactions with nanoporous carbon membranes to improve model accuracy for ternary mixtures.

The developed model can accurately predict the binary permeation of H_2 and CH_4 within acceptable margins of error (validated by Hypothesis 3). This implies that the model can be used to design membranes specifically tailored for the separation of these gases from mixtures.

The presence of CH_4 significantly hinders H_2 permeation in the binary mixture compared to pure H_2, reducing the expected separation factor. This implies that the model needs to account for competitive adsorption and interactions between gas molecules for accurate predictions in multi-component mixtures. Interestingly, the measured separation factor S_{H_2,H_2O} for H_2 from H_2O is higher than expected from the pure component permeabilities. Further investigation is required to understand this behavior.

Applying the same approach to ternary modeling proved too complex. Although the Maxwell-Stefan diffusion coefficients $\mathcal{D}_i^s$ were calculated and found to be higher

than for the other components, the model failed to converge despite the simplifications. While the results are limited by these assumptions, the modeling framework presented in chapter 3 remains a useful basis for future research.

With further refinement, this model could become a valuable tool for optimizing membrane design and predicting performance in biorefinery applications. The parameter variation highlights the importance of accurate adsorption isotherms for reliable modeling of processes with H_2 and CH_4 involved. The modeled membrane holds significant potential for future energy systems involving gas mixtures of CH_4, H_2, and other components, as discussed in chapter 2. For example, Ni catalysts used in CO_2 methanation typically become active above 280 °C, making membranes stable at these temperatures highly relevant. These two extrapolations provide a useful basis for evaluating membrane performance under industrial-like conditions and can inform design decisions such as target operating temperature, feed composition, and the required membrane area to achieve a given throughput and purity. They also enable scenario analyses for different process configurations, including heat integration and alternative gas streams, to meet specified separation factors and energy targets. However, extrapolations carry uncertainties when moving beyond the validated range; real-world effects such as concentration polarization, long-term membrane aging, and deviations from ideal transport at higher total pressures may affect performance and require experimental validation and pilot-scale testing before deployment.

5.3 Limitations of the study

This study relies on several assumptions and simplifications for tractability. Notably, the experiments consider only one specific binary and one ternary mixture, while real-world systems often involve more complex mixtures that may behave differently. Additionally, the high experimental error—especially in water adsorption and permeation measurements—likely masked subtle effects, limiting the reliability of conclusions about water's performance compared to other materials.

Another limitation is the exclusion of CO_2 from the experimental mixtures. While this study focused on other components, CO_2 plays a key role in many industrial separations and is often present at low concentrations in processes like steel production

or syngas generation. Including CO_2 in future work would enhance understanding of material performance under more realistic conditions.

Additionally, adsorption isotherms were measured up to 120 °C, whereas permeation experiments extended to 220 °C. Since biorefinery processes often operate at higher temperatures, this difference limits direct correlation between adsorption and permeation data. Extrapolation of isotherms introduced uncertainty, especially for water, whose behavior above 100 °C prevented reliable extrapolation.

Due to some limitations and the not achieved convergence a solution to the ternary could not be achieved.

Nevertheless, the approach of this work significantly improved accuracy by avoiding these pitfalls for the binary system of H_2 and CH_4 through the use of appropriate methods for extrapolation.

Finally, the one-dimensional modeling approach used here offers a simplified view. Extending to multi-dimensional models could better capture the complexity of real membranes and improve predictive accuracy.

6 Conclusion and outlook

Nanoporous carbon membranes enable separation of gas mixtures common in gasification and reaction processes. Their high thermal and chemical stability enhances process efficiency and supports economic viability.

This work presents adsorption isotherms and permeation experiments for H_2, CH_4 and H_2O, and a developed binary mass transport model for H_2 and CH_4, all focused on elevated temperatures typical of these processes. Thus, it advances the practical application of such membrane systems.

The results of this work have contributed to the scope of implementation of a water and hydrogen separation membrane in the biorefinery context. The membrane tested nanoporous carbon membrane was shown to have a high separation factor for H_2 in a binary mixture of H_2/CH_4. In this thesis, adsorption and permeation experiments conducted at DBFZ and TU Berlin were evaluated to characterize the membrane and its material. Based on these results and a developed three-layer mass transport model, the Maxwell-Stefan surface diffusion coefficients are calculated and implemented in a binary mass transport model.

The main results of this work are summarized below:

- The pure component permeances P_i of H_2 and CH_4 show a linear function of temperature and feed pressure. For H_2O the pure component permeances show a peak in permeance at temperatures of 170 °C which can be described by looking at the reduced pressure. It appears that the pure component permeance is described by a unimodal function over the reduced pressure p_i^{red} with a maximum at $p^{red} = 0.4$. The same is true for the binary and ternary permeances of the three components.

- The binary permeance for H_2 and CH_4 shows a different behavior than would be expected from the pure component permeances. The separation factor S_{H_2/CH_4} appears to be a negative linear function of p^{feed} and T. Compared to the ratio of the pure component permeances, the separation factor is 50 % lower, which can be explained by the lower permeance of H_2, which is blocked by the presence of CH_4. The same phenomenon is observed in the ternary experiments.

- The adsorption experiments for H_2 and CH_4 can be described sufficiently well with the *Langmuir* isotherms. The water adsorption at 25 °C, 50 °C and 90 °C can be described by the *Do and Do* isotherms. The *Dubinin Radushkevich* isotherm is only suitable for 50 °C.

- The calculated Maxwell-Stefan surface diffusion coefficients $\mathcal{D}_i^s$ of H_2 and CH_4 were compared with several values from the literature and with an empirical correlation. Both comparisons were found to be physically reasonable and showed good agreement.

- The binary mass transport model for H_2 and CH_4 can describe the permeances with an acceptable margin of error, but the selectivities are overestimated by a factor of 10. This discrepancy likely arises from the combination of temperature extrapolation and the measured experimental error.

- With the introduction of an optimization and temperature dependent function the margin of error was reduced significantly.

- The ternary model was developed, but due to the simplifications made it was not able to converge to a suitable solution and is therefore not used.

- Although the ternary mass transport model did not converge, the experimental permeation values to complete this work are part of this work and are of high value for future publications.

This work has demonstrated that the relatively simple characterization of a membrane by adsorption and permeation experiments can lead to a useful modeling approach for gases. The model shows unpredictable behavior for water vapor. This concludes with possible next steps that can be taken to refine the approach taken:

– While this thesis provides valuable insights into multicomponent mass transport across nanoporous carbon membranes, further progress can be made to refine the experimental framework. A more suitable setup for water permeation and adsorption measurements could potentially lead to a significant reduction in the margin of error in both permeation and adsorption errors. By minimizing these uncertainties, future research can build on this foundation with even greater confidence, paving the way for a deeper understanding of these complex separation processes.

– This study establishes a foundation for better understanding mass transport in multicomponent materials. Conducting future adsorption experiments at relevant temperatures would remove the need for extrapolation, improving data accuracy. This would reduce errors in surface diffusion coefficients, providing a more reliable basis for research and model development.

– Building on this research, future studies could test the membrane system with actual industrial gas mixtures to better understand the impact of additional components on separation performance. This real-world testing would also provide insight into membrane stability and lifetime under commercial conditions. Furthermore, using flow sheet simulation tools like Aspen Plus can help model the entire process, integrating the membrane technology with experimental data to optimize design, efficiency, and separation factor. Combining practical testing and simulation will support successful integration of advanced membrane separations into industrial applications.

– The current binary mass transport model offers a solid foundation for further development. Future work could enhance its relevance by incorporating in-situ simulations within a hydrogenation reaction system. This would reveal the membrane's direct effect on reaction performance, enabling prediction and optimization of key parameters such as yield, purity, and efficiency. Emphasizing in-situ modeling will facilitate design and optimization of membrane-integrated reaction processes, advancing cleaner and more efficient industrial operations.

List of References

Abdulsalam, J., J. Mulopo, S. O. Bada, B. Oboirien (2020): Equilibria and Isosteric Heat of Adsorption of Methane on Activated Carbons Derived from South African Coal Discards. *ACS Omega* 5 (50), 32530–32539. DOI: 10.1021/acsomega.0c04744. (Last access 01/30/2024) (cit. on p. 33).

Ahlström, J. M., V. Walter, L. Göransson, S. Papadokonstantakis (2022): The Role of Biomass Gasification in the Future Flexible Power System – BECCS or CCU?. *Renewable Energy* 190, 596–605. ISSN: 0960-1481. DOI: 10.1016/j.renene.2022.03.100. (Last access 09/06/2023) (cit. on p. 9).

Andersson, J. A. E., J. Gillis, G. Horn, J. B. Rawlings, M. Diehl (2019): CasADi: A Software Framework for Nonlinear Optimization and Optimal Control. *Mathematical Programming Computation* 11 (1), 1–36. ISSN: 1867-2957. DOI: 10.1007/s12532-018-0139-4 (cit. on p. 66).

Ashok, J., S. Pati, P. Hongmanorom, Z. Tianxi, C. Junmei, S. Kawi (2020): A Review of Recent Catalyst Advances in CO2 Methanation Processes. *Catalysis Today* 356, 471–489. ISSN: 09205861. DOI: 10.1016/j.cattod.2020.07.023 (cit. on p. 1).

Bhatia, S. K. (1993): Transport of Gases Containing Condensables in Porous Solids. *Advances in Transport Processes*, 349–418. DOI: DOI:10.1016/B978-0-444-89737-4.50012-0 (cit. on pp. 31, 53).

Bhatia, S. K., M. R. Bonilla, D. Nicholson (2011): Molecular Transport in Nanopores: A Theoretical Perspective. *Physical Chemistry Chemical Physics* 13 (34), 15350. ISSN: 1463-9076, 1463-9084. DOI: 10.1039/c1cp21166h. (Last access 07/12/2025) (cit. on p. 92).

Bienfait, M., P. Zeppenfeld, N. Dupont-Pavlovsky, M. Muris, M. R. Johnson, T. Wilson, M. DePies, O. E. Vilches (2004): Thermodynamics and Structure of Hydrogen, Methane, Argon, Oxygen, and Carbon Dioxide Adsorbed on Single-Wall Carbon Nanotube Bundles. *Physical Review B* 70 (3), 035410. DOI: 10.1103/PhysRevB.70.035410. (Last access 05/16/2023) (cit. on p. 25).

Briceño, K., A. Iulianelli, D. Montané, R. Garcia-Valls, A. Basile (2012a): Carbon Molecular Sieve Membranes Supported on Non-Modified Ceramic Tubes for Hydrogen Separation in Membrane Reactors. *International Journal of Hydrogen Energy*. ICCE-2011 37 (18), 13536–13544. ISSN: 0360-3199. DOI: 10.1016/j.ijhydene.2012.06.069. (Last access 10/30/2023) (cit. on p. 13).

Briceño, K., D. Montané, R. Garcia-Valls, A. Iulianelli, A. Basile (2012b): Fabrication Variables Affecting the Structure and Properties of Supported Carbon Molecular Sieve Membranes for Hydrogen Separation. *Journal of Membrane Science* 415–416, 288–297. ISSN: 0376-7388. DOI: 10.1016/j.memsci.2012.05.015. (Last access 10/30/2023) (cit. on p. 8).

Brinker, C. J., G. W. Scherer (2013): *Sol-Gel Science: The Physics and Chemistry of Sol-Gel Processing*. Elsevier Science. ISBN: 978-0-08-057103-4 (cit. on p. 8).

Builes, S., S. I. Sandler, R. Xiong (2013): Isosteric Heats of Gas and Liquid Adsorption. *Langmuir* 29 (33), 10416–10422. ISSN: 0743-7463. DOI: 10.1021/la401035p. (Last access 01/15/2024) (cit. on p. 33).

Burket, C. L. (2007): *Genesis and Evolution of Porosity and Microstructure in Nanoporous Carbon Derived from Polyfurfuryl Alcohol*. The Pennsylvania State University. (Last access 09/29/2023) (cit. on p. 41).

Cardoso, S. P., I. S. Azenha, Z. Lin, I. Portugal, A. E. Rodrigues, C. M. Silva (2018): Inorganic Membranes for Hydrogen Separation. *Separation & Purification Reviews* 47 (3), 229–266. ISSN: 1542-2119. DOI: 10.1080/15422119.2017.1383917. (Last access 10/29/2023) (cit. on pp. 13, 24).

Cardoso, S. P., I. S. Azenha, I. Portugal, Z. Lin, A. E. Rodrigues, C. M. Silva (2017): Single and Binary Surface Diffusion Permeation through Zeolite Membranes Using New Maxwell-Stefan Factors for Dubinin-type Isotherms and Occupancy-

Dependent Kinetics. *Separation and Purification Technology* 182, 207–218. DOI: 10.1016/j.seppur.2017.03.036 (cit. on pp. 27, 28, 30).

Choi, B.-U., D.-K. Choi, Y.-W. Lee, B.-K. Lee, S.-H. Kim (2003): Adsorption Equilibria of Methane, Ethane, Ethylene, Nitrogen, and Hydrogen onto Activated Carbon. *Journal of Chemical & Engineering Data* 48 (3), 603–607. ISSN: 0021-9568. DOI: 10.1021/je020161d. (Last access 03/09/2023) (cit. on pp. 25, 36, 100).

Daniel Siderius, V. S. (2023): *NIST/ARPA-E Database of Novel and Emerging Adsorbent Materials*. URL: https://adsorption.nist.gov/isodb/index.php?DOI=10.1007/s10450-012-9397-z#biblio (last access 10/20/2023) (cit. on pp. 25, 35, 36).

Das, S. K. (2019): General Dusty Gas Model for Porous Media with a Specified Pore Size Distribution. *Chemical Engineering Science* 203, 293–301. ISSN: 00092509 (cit. on p. 19).

De Meis, D., M. Richetta, E. Serra (2018): Microporous Inorganic Membranes for Gas Separation and Purification. *Interceram - International Ceramic Review* 67 (4), 16–21. ISSN: 2523-8957. DOI: 10.1007/s42411-018-0023-2 (cit. on pp. 13, 14).

de Oliveira, L. H., J. G. Meneguin, M. V. Pereira, J. F. do Nascimento, P. A. Arroyo (2019): Adsorption of Hydrogen Sulfide, Carbon Dioxide, Methane, and Their Mixtures on Activated Carbon. *Chemical engineering communications* 206 (11), 1533–1553. ISSN: 0098-6445. DOI: 10.1080/00986445.2019.1601627 (cit. on p. 25).

Do, D. D., H. D. Do (2000): Model for Water Adsorption in Activated Carbon. *Carbon* 38 (5), 767–773. DOI: 10.1016/S0008-6223(99)00159-1 (cit. on pp. 29–31).

Do, D. D., S. Junpirom, H. D. Do (2009): A New Adsorption–Desorption Model for Water Adsorption in Activated Carbon. *Carbon* 47 (6), 1466–1473. ISSN: 0008-6223. DOI: 10.1016/j.carbon.2009.01.039. (Last access 03/06/2023) (cit. on pp. 29, 31, 53, 63, 90).

Do, D. D. (1998): *Adsorption Analysis: Equilibria and Kinetics*. Vol. 2. Chemical Engineering. London: PUBLISHED BY IMPERIAL COLLEGE PRESS and DISTRIBUTED BY WORLD SCIENTIFIC PUBLISHING CO. ISBN: 1-86094-130-3 (cit. on pp. 14, 19, 20, 28, 30–32, 34).

Dubinin, M. M. (1959): The Potential Theory of Adsorption of Gases and Vapors for Adsorbents with Energetically Nonuniform Surfaces. *Institute of Physical Chemistry, Academy of Science, Moscow, U.S.S.R.* (cit. on p. 34).

Dubinin, M., V. Serpinsky (1981): Isotherm Equation for Water Vapor Adsorption by Microporous Carbonaceous Adsorbents. *Carbon* 19 (5), 402–403. ISSN: 00086223. DOI: 10.1016/0008-6223(81)90066-X (cit. on p. 28).

Erbil, H. Y. (2006): *Surface Chemistry of Solid and Liquid Interfaces*. Wiley. ISBN: 978-1-4051-1968-9 (cit. on p. 26).

Feldman, G. J., R. D. Cousins (1998): A Unified Approach to the Classical Statistical Analysis of Small Signals. *Physical Review D* 57 (7), 3873–3889. ISSN: 0556-2821, 1089-4918. DOI: 10.1103/PhysRevD.57.3873. (Last access 12/08/2024) (cit. on p. 66).

Figoli, A., A. Cassano, A. Basile (2016): *Membrane Technologies for Biorefining*. Membrane Technologies for Biorefining. ISBN: 978-0-08-100452-4. DOI: 10.1016/C2014-0-03660-X (cit. on p. 2).

Findenegg, G. H. (1992): Principles of Adsorption at Solid Surfaces and Their Significance in Gas/Solid and Liquid/Solid Chromatography. In: *Theoretical Advancement in Chromatography and Related Separation Techniques*. Ed. by F. Dondi, G. Guiochon. NATO ASI Series. Dordrecht: Springer Netherlands, 227–260. ISBN: 978-94-011-2686-1. DOI: 10.1007/978-94-011-2686-1_8 (cit. on p. 26).

Freundlich, H. (1922): *Kapillarchemie: Eine Darstellung Der Chemie Der Kolloide Und Verwandter Gebiete*. akademische Verlagsgesellschaft (cit. on p. 27).

Gao, X., M. R. Bonilla, J. C. D. da Costa, S. K. Bhatia (2012): The Transport of Gases in Macroporous α-Alumina Supports. *Journal of Membrane Science* 409–410, 24–33. ISSN: 0376-7388. DOI: 10.1016/j.memsci.2012.03.003 (cit. on p. 55).

Gao, X., M. R. Bonilla, J. C. D. da Costa, S. K. Bhatia (2013): The Transport of Gases in a Mesoporous γ-Alumina Supported Membrane. *Journal of Membrane Science* 428, 357–370. ISSN: 0376-7388. DOI: 10.1016/j.memsci.2012.10.015 (cit. on pp. 55, 56).

Gao, X., J. C. Diniz da Costa, S. K. Bhatia (2014): Adsorption and Transport of Gases in a Supported Microporous Silica Membrane. *Journal of Membrane Science* 460, 46–61. ISSN: 0376-7388. DOI: 10.1016/j.memsci.2014.02.028. (Last access 04/16/2023) (cit. on p. 64).

Ghaib, K., K. Nitz, F.-Z. Ben-Fares (2016): Chemical Methanation of CO 2: A Review. *ChemBioEng Reviews* 3 (6), 266–275. ISSN: 21969744. DOI: 10.1002/cben.201600022 (cit. on p. 1).

Gilliland, E. R., R. F. Baddour, G. P. Perkinson, K. J. Sladek (1974): Diffusion on Surfaces. I. Effect of Concentration on the Diffusivity of Physically Adsorbed Gases. *Industrial & Engineering Chemistry Fundamentals* 13 (2), 95–100. ISSN: 0196-4313, 1541-4833. DOI: 10.1021/i160050a001 (cit. on pp. 58, 91).

Gregg, Sing (1982): *Adsorption, Surface Area and Porosity. 2. Auflage, Academic Press, London 1982*. Wiley Online Library (cit. on pp. 27, 28, 42).

Hao, S., W. Chu, Q. Jiang, X. Yu (2014): Methane Adsorption Characteristics on Coal Surface above Critical Temperature through Dubinin–Astakhov Model and Langmuir Model. *Colloids and Surfaces A: Physicochemical and Engineering Aspects* 444, 104–113. ISSN: 0927-7757. DOI: 10.1016/j.colsurfa.2013.12.047. (Last access 10/21/2023) (cit. on pp. 27, 36, 100).

He, N. A. Seaton (2006): Heats of Adsorption and Adsorption Heterogeneity for Methane, Ethane, and Carbon Dioxide in MCM-41. *Langmuir* 22 (3), 1150–1155. ISSN: 0743-7463. DOI: 10.1021/la052237k. (Last access 01/30/2024) (cit. on pp. 33, 34).

Horikawa, T., T. Sekida, J. Hayashi, M. Katoh, D. D. Do (2011): A New Adsorption–Desorption Model for Water Adsorption in Porous Carbons. *Carbon* 49 (2), 416–424. ISSN: 0008-6223. DOI: 10.1016/j.carbon.2010.09.038. (Last access 03/01/2023) (cit. on p. 31).

Iacomi, P., P. L. Llewellyn (2019): pyGAPS: A Python-based Framework for Adsorption Isotherm Processing and Material Characterisation. *Adsorption-journal of The International Adsorption Society* 25 (8), 1533–1542. ISSN: 1572-8757. DOI: 10.1007/s10450-019-00168-5 (cit. on p. 66).

Ismail, A. F., D. Rana, T. Matsuura, H. C. Foley (2011): *Carbon-Based Membranes for Separation Processes*. New York, NY: Springer. ISBN: 978-0-387-78990-3 978-0-387-78991-0. DOI: 10.1007/978-0-387-78991-0. (Last access 01/18/2024) (cit. on p. 15).

Ito, M., H. Nishihara, K. Yamamoto, H. Itoi, H. Tanaka, A. Maki, M. T. Miyahara, S. J. Yang, C. R. Park, T. Kyotani (2013): Reversible Pore Size Control of Elastic Microporous Material by Mechanical Force. *Chemistry – A European Journal* 19 (39), 13009–13016. ISSN: 1521-3765. DOI: 10.1002/chem.201301806. (Last access 10/21/2023) (cit. on pp. 36, 100).

K. Bhatia, S., M. Rincon Bonilla, D. Nicholson (2011): Molecular Transport in Nanopores: A Theoretical Perspective. *Physical Chemistry Chemical Physics* 13 (34), 15350–15383. DOI: 10.1039/C1CP21166H. (Last access 02/27/2023) (cit. on pp. 19, 20, 68).

Kaltschmitt, M. (2019): *Energy from Organic Materials (Biomass): A Volume in the Encyclopedia of Sustainability Science and Technology, Second Edition / Edited by Martin Kaltschmitt*. 1st ed. Encyclopedia of Sustainability Science and Technology Series. New York, NY: Springer New York : Imprint: Springer. ISBN: 978-1-4939-7812-0 (cit. on pp. 1, 2, 9, 10).

Kämnitz, S., A. Simon, H. Richter, M. Weyd, U. Lubenau, T. Geisler, I. Voigt (2022): Hydrogen Conditioning Using Nanoporous Inorganic Membranes. *Chemie Ingenieur Technik* 94 (1-2), 49–55 (cit. on pp. 14, 41, 56).

Karellas, S. (2015): Hydrogen Production from Biomass Gasification. In: *Production of Hydrogen from Renewable Resources*. Biofuels and Biorefineries. Dordrecht: Springer Netherlands, 97–117. ISBN: 978-94-017-7330-0. DOI: 10.1007/978-94-017-7330-0_4. (Last access 09/13/2023) (cit. on p. 2).

Kaur, S., L. K. Sarao, Ankita, H. Singh (2023): Bioenergy: Challenges Ahead and Future. In: *Agroindustrial Waste for Green Fuel Application*. Ed. by N. Srivastava,

B. Verma, P. Mishra. Singapore: Springer Nature, 281–311. ISBN: 978-981-19-6230-1. DOI: 10.1007/978-981-19-6230-1_9. (Last access 03/23/2024) (cit. on p. 10).

Kiendl, I., M. Klemm, A. Clemens, A. Herrman (2014): Dilute Gas Methanation of Synthesis Gas from Biomass Gasification. *Fuel* 123, 211–217. ISSN: 0016-2361. DOI: 10.1016/j.fuel.2014.01.036. (Last access 08/01/2024) (cit. on p. 9).

Klemm, M. (2005): Catalytic Partial Oxidation Solves Central Problem of Biomass Gasification; Katalytische Partielle Oxidation Loest Kernproblem Der Biomassevergasung. *Erdoel Erdgas Kohle* 121. (Last access 08/01/2024) (cit. on pp. 9, 10).

Knudsen, M. (1909): Die Gesetze Der Molekularströmung Und Der Inneren Reibungsströmung Der Gase Durch Röhren. *Annalen der Physik* 333 (1), 75–130. ISSN: 1521-3889. DOI: 10.1002/andp.19093330106 (cit. on p. 19).

Kohl, A. L., R. Nielsen (1997): *Gas Purification*. Elsevier. ISBN: 978-0-08-050720-0 (cit. on pp. 7, 8, 32).

Kraume, M. (2020): *Transportvorgänge in Der Verfahrenstechnik: Grundlagen Und Apparative Umsetzungen*. Berlin, Heidelberg: Springer. ISBN: 978-3-662-60011-5 978-3-662-60012-2. DOI: 10.1007/978-3-662-60012-2. (Last access 07/12/2024) (cit. on p. 7).

Krishna, R. (1990): Multicomponent Surface Diffusion of Adsorbed Species: A Description Based on the Generalized Maxwell-Stefan Equations. *Chemical Engineering Science* 45 (7), 1779–1791. ISSN: 00092509 (cit. on p. 19).

Krishna, R., R. Baur (2003): Modelling Issues in Zeolite Based Separation Processes. *Separation and Purification Technology* 33 (3), 213–254. ISSN: 1383-5866. DOI: 10.1016/S1383-5866(03)00008-X. (Last access 01/25/2024) (cit. on p. 23).

Krishna, R., J. M. van Baten (2008): Onsager Coefficients for Binary Mixture Diffusion in Nanopores. *Chemical Engineering Science* 63 (12), 3120–3140. ISSN: 0009-2509. DOI: 10.1016/j.ces.2008.03.017. (Last access 05/11/2023) (cit. on pp. 21, 56, 59).

Krishna, R., J. M. van Baten (2009): Unified Maxwell–Stefan Description of Binary Mixture Diffusion in Micro- and Meso-Porous Materials. *Chemical Engineering Science* 64 (13), 3159–3178. ISSN: 0009-2509. DOI: 10.1016/j.ces.2009.03.047. (Last access 03/14/2023) (cit. on pp. 21, 68).

Krishna, R., J. A. Wesselingh (1997): The Maxwell-Stefan Approach to Mass Transfer. *Chemical Engineering Science* 52 (6), 861–911. ISSN: 0009-2509. DOI: 10.1016/S0009-2509(96)00458-7. (Last access 03/14/2023) (cit. on p. 65).

Krishna, R. (2019): Diffusing Uphill with James Clerk Maxwell and Josef Stefan. *Chemical Engineering Science* 195, 851–880. ISSN: 0009-2509. DOI: 10.1016/j.ces.2018.10.032. (Last access 01/03/2024) (cit. on p. 21).

Kurth, M., M. Javed, T. Schliermann, G. Brösigke, S. Kämnitz, S. K. Bhatia, J.-U. Repke (2024a): Pure Hydrogen and Methane Permeation in Carbon-Based Nanoporous Membranes: Adsorption Isotherms and Permeation Experiments. *Membranes* 14 (6), 123. ISSN: 2077-0375. DOI: 10.3390/membranes14060123. (Last access 06/15/2024) (cit. on p. 4).

Lagorsse, S., M. C. Campo, F. D. Magalhães, A. Mendes (2005): Water Adsorption on Carbon Molecular Sieve Membranes: Experimental Data and Isotherm Model. *Carbon* 43 (13), 2769–2779. DOI: 10.1016/j.carbon.2005.05.042 (cit. on pp. 27–31).

Laskar, I. I., Z. Hashisho (2020): Insights into Modeling Adsorption Equilibria of Single and Multicomponent Systems of Organic and Water Vapors. *Separation and Purification Technology* 241, 116681. DOI: 10.1016/j.seppur.2020.116681 (cit. on pp. 27, 28, 63).

Liu, L., S. (Tan, T. Horikawa, D. D. Do, D. Nicholson, J. Liu (2017): Water Adsorption on Carbon - A Review. *Advances in Colloid and Interface Science* 250, 64–78. ISSN: 0001-8686. DOI: 10.1016/j.cis.2017.10.002. (Last access 02/27/2023) (cit. on p. 30).

M. Monsalve Bravo, G. (2016): Engineering Models of Permeation in Mixed-Matrix Membranes. *phdthesis*. Brisbane, Australia: University of Queensland (cit. on p. 24).

Marcano, J. G. S., T. T. Tsotsis (2002): *Catalytic Membranes and Membrane Reactors*. John Wiley & Sons, Ltd. Chap. 2.1–2.2. ISBN: 978-3-527-60198-1. DOI: 10.1002/3527601988.ch2a. (Last access 02/08/2024) (cit. on p. 13).

Markham, E. C., A. F. Benton (1931): The Adsorption of Gas Mixtures by Silica. *Journal of the American Chemical Society* 53 (2), 497–507 (cit. on p. 32).

Melin, T., R. Rautenbach (2007): *Membranverfahren: Grundlagen Der Modul- Und Anlagenauslegung*. 3rd ed. Berlin Heidelberg New York: Springer. ISBN: 3-540-00071-2 (cit. on pp. 2, 8, 11–14, 16, 17, 19).

Men'shchikov, I. E., A. V. Shkolin, A. A. Fomkin, E. V. Khozina (2021): Thermodynamics of Methane Adsorption on Carbon Adsorbent Prepared from Mineral Coal. *Adsorption* 27 (7), 1095–1107. ISSN: 1572-8757. DOI: 10.1007/s10450-021-00338-4. (Last access 05/17/2023) (cit. on pp. 36, 100).

Monsalve-Bravo, G., S. Smart, S. Bhatia (2023): *Simulation of Multicomponent Gas Transport through Mixed-Matrix Membranes - ScienceDirect*. (Last access 04/06/2023) (cit. on pp. 13, 27).

Monsalve-Bravo, G. M., S. K. Bhatia (2018): Modeling Permeation through Mixed-Matrix Membranes: A Review. *Processes* 6 (9), 172. ISSN: 2227-9717. DOI: 10.3390/pr6090172 (cit. on p. 13).

Monsalve-Bravo, G. M., R. C. Dutta, C. C. Zuluaga-Bedoya, M. P. Adams, S. Smart, M. Konarova, S. K. Bhatia (2024): Interpreting Gas Sorption Isotherms in Glassy Polymers Using a Bayesian Framework: A View on Parameter Uncertainty Propagation into Mixture Sorption Predictions. *Journal of Membrane Science* 689, 122159. ISSN: 0376-7388. DOI: 10.1016/j.memsci.2023.122159 (cit. on pp. 13, 24).

Myers, A. L., J. M. Prausnitz (1965): Thermodynamics of Mixed-Gas Adsorption. 11 (1), 7. (Last access 05/22/2023) (cit. on p. 32).

Nagy, E. (2018): *Basic Equations of Mass Transport Through a Membrane Layer*. Elsevier Science. ISBN: 978-0-12-813723-9 (cit. on pp. 11, 19, 21, 23, 24, 56, 65).

Nazely Diban, A. T. A. J. B. A. U., I. Ortiz (2013): Membrane Reactors for in Situ Water Removal: A Review of Applications. *Industrial & Engineering Chemistry Research* 52 (31), 10342–10354. ISSN: 0888-5885. DOI: 10.1021/ie3029625 (cit. on p. 2).

Nieß, S., U. Armbruster, S. Dietrich, M. Klemm (2022): Recent Advances in Catalysis for Methanation of CO2 from Biogas. *Catalysts (Basel, Switzerland)* 12 (4), 374. ISSN: 2073-4344. DOI: 10.3390/catal12040374 (cit. on p. 9).

Ohya, H., J. Fun, H. Kawamura, K. Itoh, H. Ohashi, M. Aihara, S. Tanisho, Y. Negishi (1997): Methanation of Carbon Dioxide by Using Membrane Reactor Integrated with Water Vapor Permselective Membrane and Its Analysis. *Journal of Membrane Science* 131 (1-2), 237–247. ISSN: 03767388. DOI: 10.1016/S0376-7388(97)00055-0 (cit. on p. 13).

P. Marco-Lozar, J., M. Kunowsky, F. Suárez-García, J. D. Carruthers, A. Linares-Solano (2012): Activated Carbon Monoliths for Gas Storage at Room Temperature. *Energy & Environmental Science* 5 (12), 9833–9842. DOI: 10.1039/C2EE22769J (cit. on pp. 36, 100).

Poling, B. E., J. M. Prausnitz, J. P. O'Connell (2001): *The Properties of Gases and Liquids*. 5. ed., internat. ed. McGraw-Hill International Editions Chemical Engineering Series. New York, NY: McGraw-Hill. ISBN: 0-07-011682-2 (cit. on p. 7).

Richter, H., H. Voss, N. Kaltenborn, S. Kämnitz, A. Wollbrink, A. Feldhoff, J. Caro, S. Roitsch, I. Voigt (2017): High-Flux Carbon Molecular Sieve Membranes for Gas Separation. *Angewandte Chemie International Edition* 56 (27), 7760–7763. ISSN: 1521-3773. DOI: 10.1002/anie.201701851. (Last access 04/19/2023) (cit. on pp. 13–15).

Rönsch, S., J. Schneider, S. Matthischke, M. Schlüter, M. Götz, J. Lefebvre, P. Prabhakaran, S. Bajohr (2016): Review on Methanation – From Fundamentals to Current Projects. *Fuel* 166, 276–296. ISSN: 00162361. DOI: 10.1016/j.fuel.2015.10.111 (cit. on pp. 1, 9, 10).

Rother, J., T. Fieback (2013): Multicomponent Adsorption Measurements on Activated Carbon, Zeolite Molecular Sieve and Metal–Organic Framework. *Ad-*

sorption 19 (5), 1065–1074. ISSN: 1572-8757. DOI: 10.1007/s10450-013-9527-2. (Last access 10/21/2023) (cit. on pp. 36, 100).

Rouquerol, J., F. Rouquerol, P. Llewellyn, G. Maurin, K. Sing (2013): *Adsorption by Powders and Porous Solids: Principles, Methodology and Applications*. Academic press (cit. on p. 42).

Saracco, G., H. Neomagus, G. Versteeg, W. van Swaaij (1999): High-Temperature Membrane Reactors: Potential and Problems. *Chemical Engineering Science* 54 (13), 1997–2017. ISSN: 0009-2509. DOI: 10.1016/S0009-2509(99)00009-3 (cit. on p. 13).

Schlereth, D., O. Hinrichsen (2014): A Fixed-Bed Reactor Modeling Study on the Methanation of CO2. *Chemical Engineering Research and Design* 92 (4), 702–712. ISSN: 02638762. DOI: 10.1016/j.cherd.2013.11.014 (cit. on p. 2).

Scott, K. (1995): *Handbook of Industrial Membranes*. Ed. by K. Scott. Amsterdam: Elsevier Science. ISBN: 978-1-85617-233-2. DOI: 10.1016/B978-185617233-2/50004-0 (cit. on pp. 8, 13).

Simon, A., M. Seyring, S. Kämnitz, H. Richter, I. Voigt, M. Rettenmayr, U. Ritter (2015): Carbon Nanotubes and Carbon Nanofibers Fabricated on Tubular Porous Al2O3 Substrates. *Carbon* 90, 25–33. ISSN: 0008-6223, DOI: 10.1016/j.carbon.2015.03.048. (cit. on p. 14).

Sircar, S., R. Mohr, C. Ristic, M. B. Rao (1999): Isosteric Heat of Adsorption:\, Theory and Experiment. *The Journal of Physical Chemistry B* 103 (31), 6539–6546. ISSN: 1520-6106. DOI: 10.1021/jp9903817. (Last access 01/15/2024) (cit. on p. 33).

Son, K. N., G. E. Cmarik, J. C. Knox, J. A. Weibel, S. V. Garimella (2018): Measurement and Prediction of the Heat of Adsorption and Equilibrium Concentration of CO2 on Zeolite 13X. *Journal of Chemical & Engineering Data* 63 (5), 1663–1674 (cit. on p. 34).

Stadie, N. P., M. Murialdo, C. C. Ahn, B. Fultz (2013): Anomalous Isosteric Enthalpy of Adsorption of Methane on Zeolite-Templated Carbon. *Journal of the American Chemical Society* 135 (3), 990–993. ISSN: 0002-7863. DOI: 10.1021/ja311415m. (Last access 01/30/2024) (cit. on p. 33).

Takagi, H., H. Hatori, Y. Soneda, N. Yoshizawa, Y. Yamada (2004): Adsorptive Hydrogen Storage in Carbon and Porous Materials. *Materials Science and Engineering: B*. EMRS 2003, Symposium C, Nanoscale Materials for Energy Storage 108 (1), 143–147. ISSN: 0921-5107. DOI: 10.1016/j.mseb.2003.10.095. (Last access 10/21/2023) (cit. on pp. 36, 100).

Thunman, H., C. Gustavsson, A. Larsson, I. Gunnarsson, F. Tengberg (2019): Economic Assessment of Advanced Biofuel Production via Gasification Using Cost Data from the GoBiGas Plant. *Energy Science & Engineering* 7 (1), 217–229. ISSN: 2050-0505, 2050-0505. DOI: 10.1002/ese3.271. (Last access 03/23/2024) (cit. on p. 10).

Tóth, J. (1995): Uniform Interpretation of Gas/Solid Adsorption. *Advances in Colloid and Interface Science* 55, 1–239. ISSN: 0001-8686. DOI: 10.1016/0001-8686(94)00226-3. (Last access 01/11/2024) (cit. on p. 28).

Tsuru, T., T. Morita, H. Shintani, T. Yoshioka, M. Asaeda (2008): Membrane Reactor Performance of Steam Reforming of Methane Using Hydrogen-Permselective Catalytic SiO2 Membranes. *Journal of Membrane Science*. Inorganic and Hybrid Membranes 316 (1), 53–62. ISSN: 0376-7388. DOI: 10.1016/j.memsci.2007.10.057. (Last access 03/12/2024) (cit. on p. 2).

Tun, H., C.-C. Chen (2021): Isosteric Heat of Adsorption from Thermodynamic Langmuir Isotherm. *Adsorption* 27 (6), 979–989. ISSN: 1572-8757. DOI: 10.1007/s10450-020-00296-3. (Last access 10/24/2023) (cit. on pp. 33, 34).

Ullah, S., Y. Gao, L. Dou, Y. Liu, T. Shao, Y. Yang, A. B. Murphy (2023): Recent Trends in Plasma-Assisted CO2 Methanation: A Critical Review of Recent Studies. *Plasma Chemistry and Plasma Processing* 43 (6), 1335–1383. ISSN: 1572-8986. DOI: 10.1007/s11090-023-10417-9. (Last access 11/17/2024) (cit. on p. 1).

Virtanen, P., R. Gommers, T. E. Oliphant, M. Haberland, T. Reddy, D. Cournapeau, E. Burovski, P. Peterson, W. Weckesser, J. Bright (2020): Fundamental Algorithms for Scientific Computing in Python and SciPy 1.0 Contributors. SciPy 1.0. *Nature Methods* 17, 261–272 (cit. on p. 69).

Volodymyr Kozachynskyi Dario Staubach, M. L. M. T. J. E. M. C. G. M. (2025): *mopeds - Model based Parameter Estimation and Design of Experiments*. Version 0.10.2. URL: https://git.tu-berlin.de/dbta/optimization/mopeds (cit. on p. 66).

Voskuilen, T. G., T. L. Pourpoint, A. M. Dailly (2012): Hydrogen Adsorption on Microporous Materials at Ambient Temperatures and Pressures up to 50 MPa. *Adsorption-journal of The International Adsorption Society* 18 (3), 239–249. ISSN: 1572-8757. DOI: 10.1007/s10450-012-9397-z (cit. on pp. 36, 100).

Wächter, A., L. T. Biegler (2006): On the Implementation of an Interior-Point Filter Line-Search Algorithm for Large-Scale Nonlinear Programming. *Mathematical Programming* 106 (1), 25–57. ISSN: 1436-4646. DOI: 10.1007/s10107-004-0559-y (cit. on p. 66).

Walspurger, S., G. D. Elzinga, J. W. Dijkstra, M. Sarić, W. G. Haije (2014): Sorption Enhanced Methanation for Substitute Natural Gas Production: Experimental Results and Thermodynamic Considerations. *Chemical Engineering Journal* 242, 379–386. ISSN: 13858947. DOI: 10.1016/j.cej.2013.12.045 (cit. on p. 1).

Wang, J., X. Guo (2020): Adsorption Isotherm Models: Classification, Physical Meaning, Application and Solving Method. *Chemosphere* 258, 127279. ISSN: 0045-6535. DOI: 10.1016/j.chemosphere.2020.127279. (Last access 02/08/2024) (cit. on p. 27).

Wang, K., S. Qiao, X. Hu (2004): Study of Isosteric Heat of Adsorption and Activation Energy for Surface Diffusion of Gases on Activated Carbon Using Equilibrium and Kinetics Information. *Separation and Purification Technology* 34 (1-3), 165–176. ISSN: 1383-5866. DOI: 10.1016/s1383-5866(03)00190-4. (Last access 07/07/2025) (cit. on p. 58).

Weyd, M., H. Richter, P. Puhlfürß, I. Voigt, C. Hamel, A. Seidel-Morgenstern (2008): Transport of Binary Water–Ethanol Mixtures through a Multilayer Hydrophobic Zeolite Membrane. *Journal of Membrane Science* 307 (2), 239–248. ISSN: 03767388. DOI: 10.1016/j.memsci.2007.09.032 (cit. on pp. 12, 14, 41).

Yang, R. T. (1987): CHAPTER 4 - Rate Processes in Adsorbers. In: *Gas Separation by Adsorption Processes*. Ed. by R. T. Yang. Butterworth-Heinemann, 101–139. ISBN: 978-0-409-90004-0. DOI: 10.1016/B978-0-409-90004-0.50007-6 (cit. on pp. 34, 58, 91, 100).

Zheng, Q. R., S. Gao, C. Jie (2012): Determination of the Isosteric Heat of Adsorption of Hydrogen on the Multi-Walled Carbon Nanotubes. *Advanced Materials Research* 512–515, 1484–1491. ISSN: 1662-8985. DOI: 10.4028/www.scientific.net/AMR.512-515.1484. (Last access 01/30/2024) (cit. on p. 33).

Zhou, L., Y. Zhou, Y. Sun (2004): A Comparative Study of Hydrogen Adsorption on Superactivated Carbon versus Carbon Nanotubes. *International Journal of Hydrogen Energy* 29 (5), 475–479. ISSN: 0360-3199. DOI: 10.1016/S0360-3199(03)00092-2. (Last access 01/30/2024) (cit. on p. 33).

Appendix A

Derivation of Binary Set of Equations

Together with the formulated binary case of the onsager formualted set of equations eq. (3.19) and eq. (3.20) the equation system can be solved:

$$-\frac{q_i}{RT}\nabla\mu_i = \sum_{j=1,i\neq j}^{n} \frac{q_j N_i - q_i N_j}{c_T \mathcal{D}_{ij}^s} + \frac{N_i}{\mathcal{D}_i^s} \tag{A.1}$$

with:

$$c_T = \sum_i^n q_i \text{ and } q_i = \theta_i q_{i,sat} \tag{A.2}$$

Writing out for binary case

(A.3)

(A.4)

$$-\frac{q_1}{RT}\frac{d\mu_1}{dz} = \frac{q_2N_1 - q_1N_2}{(q_1+q_2)\mathcal{D}^s_{1,2}} + \frac{N_1}{\mathcal{D}^s_1} \tag{A.5}$$

$$-\frac{q_2}{RT}\frac{d\mu_2}{dz} = \frac{q_1N_2 - q_2N_1}{(q_1+q_2)\mathcal{D}^s_{1,2}} + \frac{N_2}{\mathcal{D}^s_2} \tag{A.6}$$

(A.7)

(A.8)

Rearranging: (A.9)

(A.10)

$$\underbrace{\left(-\frac{q_{1,sat}\theta_1}{RT}\right)}_{\alpha_1}\frac{d\mu_1}{dz} = N_1\underbrace{\left(\frac{q_{2,sat}\theta_2\mathcal{D}^s_1 + (q_{2,sat}\theta_2 + q_{1,sat}\theta_1)\mathcal{D}^s_{1,2}}{(q_{1,sat}\theta_1 + q_{2,sat}\theta_2)\,\mathcal{D}^s_{1,2}\mathcal{D}^s_1}\right)}_{\beta_1} - N_2\underbrace{\left(\frac{q_{1,sat}\theta_1}{(q_{1,sat}\theta_1 + q_{2,sat}\theta_2)\mathcal{D}^s_{1,2}}\right)}_{\gamma_1}$$

(A.11)

$$\underbrace{\left(-\frac{q_{2,sat}\theta_2}{RT}\right)}_{\alpha_2}\frac{d\mu_2}{dz} = N_2\underbrace{\left(\frac{q_{1,sat}\theta_1\mathcal{D}^s_2 + (q_{1,sat}\theta_1 + q_{2,sat}\theta_2)\mathcal{D}^s_{1,2}}{(q_{1,sat}\theta_1 + q_{2,sat}\theta_2)\,\mathcal{D}^s_{1,2}\mathcal{D}^s_2}\right)}_{\beta_2} - N_1\underbrace{\left(\frac{q_{2,sat}\theta_2}{(q_{1,sat}\theta_1 + q_{2,sat}\theta_2)\mathcal{D}^s_{1,2}}\right)}_{\gamma_2}$$

(A.12)

Then rewrite for N_i (A.13)

$$N_1 = -\frac{\alpha_1}{\beta_1}\frac{d\mu_1}{dz} + \frac{\gamma_1}{\beta_1}N_2 \tag{A.14}$$

(A.15)

$$N_2 = -\frac{\alpha_2}{\beta_2}\frac{d\mu_2}{dz} + \frac{\gamma_2}{\beta_2}N_1 \tag{A.16}$$

(A.17)

rearranging (A.18)

(A.19)

$$N_1 = -\frac{\alpha_1\beta_2}{\beta_1\beta_2 - \gamma_1\gamma_2}\frac{d\mu_1}{dz} - \frac{\gamma_1\alpha_2}{\beta_1\beta_2 - \gamma_1\gamma_2}\frac{d\mu_2}{dz} \tag{A.20}$$

$$N_2 = -\frac{\alpha_2\beta_1}{\beta_1\beta_2 - \gamma_1\gamma_2}\frac{d\mu_2}{dz} - \frac{\gamma_2\alpha_1}{\beta_1\beta_2 - \gamma_1\gamma_2}\frac{d\mu_1}{dz} \tag{A.21}$$

(A.22)

(A.23)

$$N_i = \sum_{i=1}^{n} L_{i,j} \nabla \mu_i \tag{A.24}$$

$$\nabla \mu_i = \frac{RT}{p_i} \nabla p_i \tag{A.25}$$

$$\text{With } \frac{d\mu_i}{dz} = \frac{RT}{p_i} \frac{dp_i}{dz} \text{ and rearranging} \tag{A.26}$$

$$N_{1,z} = -RT \left[\frac{L_{11}(p_1,p_2)}{p_1} \frac{dp_1}{dz} + \frac{L_{12}(p_1,p_2)}{p_2} \frac{dp_2}{dz} \right] \tag{A.27}$$

$$N_{2,z} = -RT \left[\frac{L_{21}(p_1,p_2)}{p_1} \frac{dp_1}{dz} + \frac{L_{22}(p_1,p_2)}{p_2} \frac{dp_2}{dz} \right] \tag{A.28}$$

(A.29)

(A.30)

Appendix B

Code snippets used for modeling

Code B.1: Sympy Usage for derivation.

```
from sympy import *
from sympy.parsing.latex import parse_latex
from sympy import latex
from sympy import simplify
from sympy.abc import x, y, z, theta, R, T, epsilon, rho, D,q
import scipy.constants as const

D1_Kn = symbols('D_Kn_{1}')
D2_Kn = symbols('D_Kn_{2}')
D12_Kn = symbols('D_Kn_{12}')



p1_Kn = Function('p1')(z)
p2_Kn = Function('p2')(z)



alpha_1_Kn = p1_Kn/(R*T)**2
beta_1_Kn = (p2_Kn*D1_Kn +(p1_Kn + p2_Kn) * D12_Kn)/((p1_Kn +
    p2_Kn) * D1_Kn * D12_Kn)

gamma_1_Kn = p1_Kn/((p1_Kn + p2_Kn) * D12_Kn)
```

```
alpha_2_Kn = p2_Kn/(R*T)**2
beta_2_Kn = (p1_Kn*D2_Kn +(p1_Kn + p2_Kn) * D12_Kn)/((p1_Kn +
    p2_Kn) * D2_Kn * D12_Kn)

gamma_2_Kn = p2_Kn/((p1_Kn + p2_Kn) * D12_Kn)

den_Kn = (beta_1_Kn*beta_2_Kn - gamma_1_Kn*gamma_2_Kn)

L11 = -(alpha_1_Kn*beta_2_Kn)/den_Kn
L12 = -(gamma_1_Kn*alpha_2_Kn)/den_Kn
L22 = -(alpha_2_Kn*beta_1_Kn)/den_Kn
L21 = L12

# D_12 und D_21 substitute using Vignes relation
D12_Kn = D1_Kn**(p1_Kn/(p1_Kn+p2_Kn))*D2_Kn**(p2_Kn/(p1_Kn+
    p2_Kn))

L11_Kn = L11.subs('D_Kn_{12}', D12_Kn)
L12_Kn = L12.subs('D_Kn_{12}', D12_Kn)
L21_Kn = L21.subs('D_Kn_{12}', D12_Kn)
L22_Kn = L22.subs('D_Kn_{12}', D12_Kn)

dp1_dz = Derivative(p1_Kn,z)
dp2_dz = Derivative(p2_Kn,z)

N1_Kn = -R*T*(L11_Kn/p1_Kn * dp1_dz + L12_Kn/p2_Kn * dp2_dz)
N2_Kn = -R*T*(L21_Kn/p1_Kn * dp1_dz + L22_Kn/p2_Kn * dp2_dz)



## Starting from here the equations are set and will be derivated
N1_derivative = diff(N1_Kn, z)
```

```
N2_derivative = diff(N2_Kn, z)

## Finite difference method:

p1_neg = symbols("p1_neg")
p1_pos = symbols("p1_pos")
p1_pos2 = symbols("p1_pos2")
p1_dot = symbols("p1_dot")

p2_neg = symbols("p2_neg")
p2_pos = symbols("p2_pos")
p2_pos2 = symbols("p2_pos2")
p2_dot = symbols("p2_dot")

z_neg = symbols("z_neg")
z_pos = symbols("z_pos")
z_pos2 = symbols("z_pos2")
z_dot = symbols("z_dot")

dp1_dz_q = symbols("dp1_dz_q")
dp2_dz_q = symbols("dp2_dz_q")
dp1_dz2_q = symbols("dp1_dz2_q")
dp2_dz2_q = symbols("dp2_dz2_q")

## Second derivation as central differentation quotients
N1_derivative = N1_derivative.subs(diff(dp1_dz, z), dp1_dz2_q).subs(diff(
    dp2_dz, z),dp2_dz2_q)
N2_derivative = N2_derivative.subs(diff(dp1_dz, z), dp1_dz2_q).subs(diff(
    dp2_dz, z),dp2_dz2_q)

## First derivation as central differentation quotients
N1_derivative = N1_derivative.subs(diff(p1_Kn, z), dp1_dz_q).subs(diff(
    p2_Kn, z),dp2_dz_q)
```

```
N2_derivative = N2_derivative.subs(diff(p1_Kn, z), dp1_dz_q).subs(diff(
    p2_Kn, z),dp2_dz_q)
N1_derivative = N1_derivative.subs(p1_Kn,p1_dot).subs(p2_Kn, p2_dot)
N2_derivative = N2_derivative.subs(p1_Kn,p1_dot).subs(p2_Kn, p2_dot)

R = symbols("R")
T = symbols("T")

# Using the lambdify function ofsympy a numpy functio is created based on the
    function values

func1_Kn = lambdify((p1_dot,p2_dot, dp1_dz_q, dp2_dz_q, dp1_dz2_q,
    dp2_dz2_q, D1_Kn, D2_Kn, T, R), N1_derivative, modules='numpy')
func2_Kn = lambdify((p1_dot,p2_dot, dp1_dz_q, dp2_dz_q, dp1_dz2_q,
    dp2_dz2_q, D1_Kn, D2_Kn, T, R), N2_derivative, modules ='numpy')
```

Code B.2: Thermodynamic calculations for fugacity.

```
    # Set the conditions and imports
    from scipy.constants import bar
    from thermo import *
    import numpy as np

    # Define the components
    components = ['methane', 'hydrogen']

    # Obtain the necessary parameters
    constants, correlations = \\
    ChemicalConstantsPackage.from_IDs(components)
    n = 20
    p = np.linspace(1e5, 15e5, n)
    T = 120+273.15
    f_1 = np.empty([len(p)])
    f_2 = np.empty([len(p)])
```

```
    x = [0.1, 0.9]

    for i in range(0,n):
        # iterate over the pressure
        # # iterate over the temperature
        eos = PRMIX(T=T, P=p[i], \\
        Tcs=constants.Tcs, Pcs=constants.Pcs, \\
        omegas=constants.omegas, zs=x)
        f_1[i] = eos.fugacities_g[0]
        f_2[i] = eos.fugacities_g[1]
```

Code B.3: Temperature optimization.

```
import numpy as np
from scipy.optimize import minimize
import pandas as pd

experimental_data = pd.read_csv(path)
N_exp_H2 = experimental_data["wasserstoff_perm_mean"]
N_exp_CH4 = experimental_data["methan_perm_mean"]



def objective_function_dummy(F):
    return optimierung(F)

def objective_function(F):
    predictions = optimierung(F) # Vorhersagen basierend auf F
    N_pred_H2 = predictions["H2_perm_model"]
    N_pred_CH4 = predictions["CH4_perm_model"]
    error1 = np.sum((N_exp_H2 - N_pred_H2) ** 2) # H2
    error2 = np.sum((N_exp_CH4 - N_pred_CH4) ** 2) #CH4
    return error1 + error2
```

```
Nfeval = 1

def callbackF(Xi):
    global Nfeval
    print(Nfeval, Xi)
    Nfeval += 1

# Starting values for F (F1 and F2)
initial_params = [0.08612346, 1.11039317]

# Optimization
bounds = [(1e-6, 10), (1e-6, 100)]
result = minimize(objective_function,
                  initial_params,
                  method = 'L-BFGS-B',
                  bounds = bounds,
                  tol=1e-9,
                  callback=callbackF,
                 options={'disp': True, 'maxiter': 30, 'iprint':1},
                 )
```

Appendix C

Design of Experiments

Using Design Expert 12 ™by *statcon* the design of experiment was conducted with the following presets:

Purpose: Optimization

Type of design: Factorial/RSM

Hard-to-change factors: Yes

Optimal (user-defined) design: Numerical factors: 2

Search: Best

Optimality: I-optimal

Blocks: 1

Ratio of variances: 1

Groups: Required: 3, Additional: 2

Trials: Required model points: 6, Additional model points: 5, Central points: 0

Based on this setup a design of experiment (DoE) was developed and the experiments were conducted accordingly.

	α=**-1**	α=**0**	α=**+1**
H_2	T = 120 °C p^{feed} = 2 bar p^{perm} = 1 bar	T = 170 °C p^{feed} = 2.25 bar p^{perm} = 1.375 bar	T = 220 °C p^{feed} = 2.5 bar p^{perm} = 1.75 bar
CH_4	T = 120 °C p^{feed} = 6 bar p^{perm} = 1 bar	T = 170 °C p^{feed} = 11 bar p^{perm} = 2 bar	T = 220 °C p^{feed} = 16 bar p^{perm} = 3 bar
H_2O	T = 120 °C p_i^{feed} = 0.2 bar p^{perm} = 1 bar	T = 170 °C p_i^{feed} = 0.4 bar p^{perm} = 1.5 bar	T = 220 °C p^{feed} = 2.5 bar p^{perm} = 2 bar
H_2O/H_2	T = 120 °C	T = 170 °C	T = 220 °C
H_2O/CH_4	p^{feed} = 6 bar	p^{feed} = 11 bar	p^{feed} = 16 bar
H_2/CH_4	p^{perm} = 0 bar	p^{perm} = 2 bar	p^{perm} = 3 bar

Appendix D

Experimental Results

D.1 Pure Component Permeation Experiments

Tab. D.1: Pure component permeation results for H_2.

F_i / mol min^{-1}	p_i^{TMP} / bar	P_i / mol m^{-2} bar^{-1} s^{-1}	T / °C	x_i^{sweep} / mol mol^{-1}
0.00714251	2.519078257	1.611777856	170.09375	0.001532908
0.005367518	2.190285225	1.392975421	120.0695652	0.001198604
0.007164121	2.439254326	1.669432658	170.0957447	0.001536858
0.007149207	2.441537754	1.664420663	170.0818182	0.001534265
0.008112793	2.601505422	1.772705345	169.9913043	0.001704947
0.008175989	2.619130605	1.774508575	170.0093023	0.001715818
0.008450527	2.397472902	2.003632088	220.0111111	0.001763055
0.008803979	2.656258723	1.883976191	169.9869565	0.001823312
0.008450593	2.534624966	1.895135796	220.0065217	0.001763311
0.007610918	2.483812436	1.741744538	170.0673243	0.001617045
0.006223296	2.569922961	1.378293202	120.0642857	0.001361665
0.006253431	2.193924262	1.620188989	170.1021739	0.001340217
0.00622724	2.19386147	1.613423973	170.0916667	0.001363955
0.006553505	2.700122191	1.379629823	120.0557377	0.001424807
0.007910701	2.190779479	2.052401862	220.0086957	0.001668555
0.009394528	2.676065622	1.99547355	220.0108696	0.001921131

Tab. D.2: Pure component permeation results for CH_4.

F_i mol min^{-1}	p_i^{TMP} bar	P_i mol m^{-2} bar^{-1} s^{-1}	T °C	x_i^{sweep} mol mol^{-1}
0.000103702	6.191804493	0.009519482	120.0695652	2.63E-05
0.000156208	6.193702005	0.014335743	169.9125	3.96E-05
0.000130079	6.1946867	0.011936387	169.9947368	3.30E-05
0.000207887	6.200238811	0.019058674	219.9717391	5.26E-05
0.000232414	11.23273485	0.011759239	120.0387755	5.88E-05
0.000200808	11.23350639	0.010160755	120.0289474	5.08E-05
0.000279691	11.23489965	0.014150572	169.9913043	7.07E-05
0.000269334	11.24744673	0.013611249	170.0706522	6.81E-05
0.000437178	16.2350687	0.015306819	170.0711111	0.000110044
0.000272659	11.24485772	0.0137825	170.0688889	6.89E-05
0.000396263	16.24604314	0.013865786	170.0846154	9.98E-05
0.000266493	11.24471711	0.013470821	170.1010638	6.74E-05

Tab. D.3: Pure component permeation results for H_2O.

F_i mol min^{-1}	p_i^{TMP} bar	P_i mol m^{-2} bar^{-1} s^{-1}	T °C	x_i^{sweep} mol mol^{-1}
0.162695223	9.565756592	9.686736638	220.5933333	0.808625937
0.144432948	8.638727565	9.527229567	220.83	0.79353542
0.009766484	1.004098653	7.535756086	120.6756757	0.154958603
0.1164752	7.143236371	9.343006731	220.69	0.753067211
0.062576509	2.199836616	16.43210357	170.89	0.61576163
0.164434487	12.5495073	7.452529228	220.5366667	0.814760674
0.077101216	3.619966612	12.52484964	221.07	0.648112851
0.056544593	2.164233299	15.17944323	170.79	0.592699749
0.056100525	2.126623594	15.27368467	170.8333333	0.593810871
0.041557315	2.393002218	10.5439782	170.85	0.491572249
0.070084297	3.039351566	13.38575108	170.6117647	0.64540302

D.2 Binary Permeation Experiments

Tab. D.4: Binary permeation results for H_2/CH_4.

F_{CH_4} mol min^{-1}	F_{H_2} mol min^{-1}	P_{CH_4} mol m^{-2} bar^{-1} min^{-1}	P_{H_2} mol m^{-2} bar^{-1} min^{-1}	p^{feed} bar	p^{perm} bar	T °C	$x^{feed}_{CH_4}$ mol mol^{-1}	$x^{feed}_{H_2}$ mol mol^{-1}
0.000176887	0.004638169	0.012311369	0.859053961	10.23794233	1.004804922	120.16	0.726725173	0.273274827
8.44E-05	0.002765599	0.010650787	0.928558142	5.199884481	1.001946073	120.1596154	0.726725173	0.273274827
0.000228042	0.005956962	0.015874088	1.103653816	10.23631467	0.996124058	170.0777778	0.726725173	0.273274827
0.000323766	0.007762388	0.015608701	0.995954665	15.22270022	1.007517662	170.1088889	0.726725173	0.273274827
0.000104168	0.003841735	0.013124102	1.288005693	5.212290222	1.015113364	170.1444444	0.726725173	0.273274827
0.000441584	0.00912736	0.021263003	1.169732846	15.24385956	1.008060269	219.9911111	0.726725173	0.273274827
0.000268901	0.006994361	0.018707427	1.295275687	10.2427589	1.003000108	219.9897959	0.726725173	0.273274827
0.000176887	0.004638169	0.012311369	0.859053961	10.23794233	1.004804922	120.16	0.726725173	0.273274827
8.44E-05	0.002765599	0.010650787	0.928558142	5.199884481	1.001946073	120.1596154	0.726725173	0.273274827
0.000228042	0.005956962	0.015874088	1.103653816	10.23631467	0.996124058	170.0777778	0.726725173	0.273274827
0.000323766	0.007762388	0.015608701	0.995954665	15.22270022	1.007517662	170.1088889	0.726725173	0.273274827
0.000104168	0.003841735	0.013124102	1.288005693	5.212290222	1.015113364	170.1444444	0.726725173	0.273274827
0.000441584	0.00912736	0.021263003	1.169732846	15.24385956	1.008060269	219.9911111	0.726725173	0.273274827
0.000268901	0.006994361	0.018707427	1.295275687	10.2427589	1.003000108	219.9897959	0.726725173	0.273274827

Tab. D.5: Binary permeation results for H_2/H_2O.

F_{H_2O} mol min^{-1}	F_{H_2} mol min^{-1}	P_{H_2O} mol m^{-2} bar^{-1} min^{-1}	P_{H_2} mol m^{-2} bar^{-1} min^{-1}	p^{feed} bar	p^{perm} bar	T °C	$x^{feed}_{H_2O}$ mol mol^{-1}	$x^{feed}_{H_2}$ mol mol^{-1}
0.088084948	0.000451431	3.43190174	0.26053765	15.31257226	0.027287141	220.6647059	0.939624277	0.060375723
0.099201503	6.38E-05	6.207647343	0.053500419	10.2325946	1.01495848	220.58	0.939624277	0.060375723
0.004440675	1.31E-05	0.953893038	0.038550995	2.204657433	0.021973329	120.7	0.939624277	0.060375723
0.032065373	7.14E-05	4.230124007	0.040694622	4.800765033	0.027670118	220.8066667	0.827967934	0.172032066
0.026866083	0.000208581	1.709317994	0.060431595	10.41372917	0.118004904	220.33	0.827967934	0.172032066
0.022897229	3.06E-05	4.458596517	0.025184229	3.01319425	0.004069135	170.65	0.827980165	0.172019835

Tab. D.6: Binary permeation results for CH_4/H_2O.

F_{H_2O} mol min^{-1}	F_{CH_4} mol min^{-1}	P_{H_2O} mol m^{-2} bar^{-1} min^{-1}	P_{CH_4} mol m^{-2} bar^{-1} min^{-1}	p^{feed} bar	p^{perm} bar	T °C	$x^{feed}_{H_2O}$ mol mol^{-1}	$x^{feed}_{CH_4}$ mol mol^{-1}
0.018416906	2.01E-05	1.138885233	0.012598938	10.24119797	1.082389943	170.8233333	0.919386922	0.080613078
0.006864543	1.62E-05	0.277132516	0.007038916	15.2330086	1.19225651	170.9	0.919386922	0.080613078
0.023350548	1.02E-05	2.842994167	0.002219992	7.260150133	1.00833157	170.8433333	0.682907241	0.317092759
0.10304384	2.04E-05	4.427853568	0.008885776	15.1912815	1.184118227	220.5227273	0.919386922	0.080613078
0.031954356	2.88E-05	1.825109724	0.003192444	15.1744132	1.110059977	220.72	0.682907241	0.317092759
0.033767631	1.73E-05	2.950148827	0.002762581	10.25584673	1.160517333	220.8533333	0.682907241	0.317092759
0.06324261	6.16E-06	8.14165098	0.006984179	5.232093467	1.040884793	170.52	0.919386922	0.080613078

D.3 Ternary Permeation Experiments

Tab. D.7: Ternary permeation results for $CH_4/H_2O/H_2$.

P_{H_2O} mol m^{-2} bar^{-1} min^{-1}	P_{CH_4} mol m^{-2} bar^{-1} min^{-1}	P_{H_2} mol m^{-2} bar^{-1} min^{-1}	p^{feed} bar	p^{perm} bar	T °C	$x^{feed}_{H_2O}$ mol mol^{-1}	$x^{feed}_{CH_4}$ mol mol^{-1}	$x^{feed}_{H_2}$ mol mol^{-1}
2.022936949	0	0.003738064	4.531388667	1.002634723	170.9133333	0.582322219	0.317274917	0.100402864
1.261479604	0.002202381	0.004060056	4.5167399	0.992054993	170.7066667	0.57866434	0.32156348	0.099772179
15.26551931	0	0.001479073	1.503545417	1.098666358	170.95	0.582187776	0.31743254	0.100379683
3.538156167	0.000258596	0.001379899	1.554409533	0.004882962	171.0933333	0.582295211	0.317306582	0.100398207
2.498520128	0.001932243	0.005748956	4.533830333	1.026235787	170.7666667	0.578637817	0.321594577	0.099767606
2.338407127	0.001427979	0.015121132	7.148655733	1.210160767	220.67	0.578724046	0.32149348	0.099782474
7.592656326	0	0.002276403	1.565803133	0	170.94	0.582570722	0.316983568	0.10044571
2.052609066	0.002015541	0.022538665	7.228410833	0.004069135	170.7133333	0.578697504	0.321524598	0.099777898
1.287958591	0.000428858	0.003258706	4.531388667	1.2443415	170.86	0.578710775	0.321509039	0.099780186
2.702551021	0.000699921	0.004267851	4.523250433	1.2109746	170.8566667	0.578690869	0.321532378	0.099776753
1.791284463	0.001443727	0.050418372	14.810633	0.003255308	220.82	0.578558901	0.321676777	0.099764322
6.56694509	0.002182905	0	1.118198303	0	120.63	0.581584194	0.318140191	0.100275615
1.276725454	0.000582059	0.003689173	7.1592356	1.9995727	170.7166667	0.578684242	0.321540147	0.099775611
1.232436309	0.000927139	0.023865086	14.71785663	2.0109663	220.6466667	0.578605322	0.321622353	0.099772326
3.67349749	0.002269375	0	0.4443495	0.000813827	120.8133333	0.581899213	0.317770857	0.10032993
3.077436946	0.002659225	0	0.504572727	0.017090367	120.6333333	0.578690873	0.321532373	0.099776754

Tab. D.8: Pure component adsorption results for H_2.

90 °C		110 °C		120 °C	
p_i bar	q_i mmol g^{-1}	p_i bar	q_i mmol g^{-1}	p_i bar	q_i mmol g^{-1}
5.000009	0.221895	5.000011	0.12487	5.000011	0.12487
9.985321	0.277295	9.999781	0.178586	9.999781	0.178586
19.935091	0.31285	19.905232	0.14113	19.905232	0.14113
29.977451	0.37278	30.001239	0.194543	30.001239	0.194543
39.98334	0.409598	39.897639	0.075468	39.897639	0.075468
44.958228	0.410499	45.005174	0.217153	45.005174	0.217153

Tab. D.9: Pure component adsorption results for CH_4.

90 °C		110 °C		120 °C	
p_i bar	q_i mmol g^{-1}	p_i bar	q_i mmol g^{-1}	p_i bar	q_i mmol g^{-1}
5.000417	0.662422	5.000776	0.472314	5.000776	0.472314
9.97253	0.805071	9.980535	0.586393	9.980535	0.586393
19.998198	0.994613	20.012386	0.768286	20.012386	0.768286
29.959651	1.208831	29.988073	0.888567	29.988073	0.888567
39.997118	1.20527	39.978058	0.953166	39.978058	0.953166
44.996064	1.236137	45.005535	1.034464	45.005535	1.034464

D.4 Adsorption Experiments

Tab. D.10: Pure component adsorption results for H_2O.

25 °C	
p_i bar	q_i mmol g^{-1}
0.000211841	0.441959227
0.001143978	4.322725322
0.002270027	8.995472103
0.003442397	14.46023605
0.004599915	20.87354077
0.005741701	27.99291845
0.006905125	37.25321888
0.008065417	48.40429185
0.009230121	60.31738197
0.010379533	73.60643777
0.011535651	82.06845494
0.012812693	89.09828326
0.013887525	95.36416309
0.015049696	101.4448498
0.016187469	106.3785408
0.017354839	111.3148069
0.018535676	115.7515021
0.019704646	120.548927
0.020845619	124.239485

50 °C	
p_i bar	q_i mmol g^{-1}
0.012351815	0.69382864
0.024703629	1.386245502
0.037055444	1.000259538
0.049407259	1.307692308
0.061759073	1.307583525
0.074110888	1.32134537
0.086462703	1.467443993
0.098814517	1.495478983

90 °C	
p_i bar	q_i mmol g^{-1}
0.07009182	0.000337213
0.14018364	0.000509012
0.21027546	0.000686306
0.28036728	0.000821024
0.350459099	0.001071534
0.420550919	0.001304669

Appendix E

Binary Simulation Results

Tab. E.1: Binary modeling results for H_2/CH_4.

$x_{CH_4^{feed}}$ mol mol^{-1}	$x_{H_2^{feed}}$ mol mol^{-1}	F_{CH_4} mol min^{-1}	F_{H_2} mol min^{-1}	P_{CH_4} mol m^{-2} bar^{-1} min^{-1}	P_{H_2} mol m^{-2} bar^{-1} min^{-1}	T °C
0.726725173	0.273274827	0.000176887	0.004638169	0.012311369	0.859053961	120.16
0.726725173	0.273274827	8.44E-05	0.002765599	0.010650787	0.928558142	120.1596154
0.726725173	0.273274827	0.000228042	0.005956962	0.015874088	1.103653816	170.0777778
0.726725173	0.273274827	0.000323766	0.007762388	0.015608701	0.995954665	170.1088889
0.726725173	0.273274827	0.000104168	0.003841735	0.013124102	1.288005693	170.1444444
0.726725173	0.273274827	0.000441584	0.00912736	0.021263003	1.169732846	219.9911111
0.726725173	0.273274827	0.000268901	0.006994361	0.018707427	1.295275687	219.9897959
0.726725173	0.273274827	0.000176887	0.004638169	0.012311369	0.859053961	120.16
0.726725173	0.273274827	8.44E-05	0.002765599	0.010650787	0.928558142	120.1596154
0.726725173	0.273274827	0.000228042	0.005956962	0.015874088	1.103653816	170.0777778
0.726725173	0.273274827	0.000323766	0.007762388	0.015608701	0.995954665	170.1088889
0.726725173	0.273274827	0.000104168	0.003841735	0.013124102	1.288005693	170.1444444
0.726725173	0.273274827	0.000441584	0.00912736	0.021263003	1.169732846	219.9911111
0.726725173	0.273274827	0.000268901	0.006994361	0.018707427	1.295275687	219.9897959

Tab. E.2: Binary modeling standard deviation for H_2/CH_4.

σF_{CH_4} $mol\,min^{-1}$	σF_{H_2} $mol\,min^{-1}$	σP_{CH_4} $mol\,m^{-2}\,bar^{-1}\,min^{-1}$	σP_{H_2} $mol\,m^{-2}\,bar^{-1}\,min^{-1}$	σT °C
1.27E-07	2.71E-05	1.62E-05	0.005171422	0.396805425
5.60E-08	2.57E-05	4.54E-05	0.008743443	0.409332127
2.89E-07	5.34E-05	2.54E-05	0.009949812	0.566443806
2.86E-05	0.000437757	0.001361682	0.055113303	0.599174516
5.87E-05	0.000834546	0.007435404	0.28234424	0.633373204
8.05E-07	8.68E-05	6.15E-05	0.011563591	0.32180049
2.02E-05	3.68E-05	0.001404611	0.006898635	0.423893116
1.27E-07	2.71E-05	1.62E-05	0.005171422	0.396805425
5.60E-08	2.57E-05	4.54E-05	0.008743443	0.409332127
2.89E-07	5.34E-05	2.54E-05	0.009949812	0.566443806
2.86E-05	0.000437757	0.001361682	0.055113303	0.599174516
5.87E-05	0.000834546	0.007435404	0.28234424	0.633373204
8.05E-07	8.68E-05	6.15E-05	0.011563591	0.32180049
2.02E-05	3.68E-05	0.001404611	0.006898635	0.423893116

Appendix F

Model Variable Variation

Tab. F.1: Variation for the study with $x_{\mathrm{CH_4}}^{feed} = 0.73\,\mathrm{mol\,mol^{-1}}$ and $x_{\mathrm{H_2}}^{feed} = 0.27\,\mathrm{mol\,mol^{-1}}$ with the resulting permeation.

T °C	$P_{\mathrm{H_2}}$ mol m^{-2} bar^{-1} min^{-1}	$P_{\mathrm{CH_4}}$ mol m^{-2} bar^{-1} min^{-1}	$S_{\mathrm{H_2,CH_4}}$ –	$\sigma P_{\mathrm{H_2}}$ mol m^{-2} bar^{-1} min^{-1}	$\sigma P_{\mathrm{CH_4}}$ mol m^{-2} bar^{-1} min^{-1}
220	1.58491874080423	0.015752795	100.6119067	0.907759413	0.000942811
230	1.57425793557711	0.015820465	99.50769055	0.306113414	0.000671049
240	1.79981174619951	0.015839999	113.6244861	0.076276177	0.001263241
250	1.54901908561042	0.015887294	97.50049855	0.679038408	0.00023516
260	1.52746625837778	0.015830974	96.48593058	0.3390112	0.000809496
270	1.52009108332982	0.015870682	95.77982114	0.289095975	0.000566033
280	1.51574809558881	0.015968213	94.92283799	0.395435091	0.00033656
290	1.50593467	0.01600794	94.07423256	0.364792579	0.000633965
300	1.49209810162975	0.016022973	93.12242501	0.43948718	0.001490384
310	1.48205529817428	0.016034105	92.43143276	0.622322446	0.00070487
320	1.45954247456269	0.015978584	91.34366816	0.164962886	0.00167691
330	1.45201701100638	0.016078011	90.31073626	0.318315898	0.001369176
340	1.44716626703874	0.016097999	89.89727649	0.282720144	0.001987465
350	7.2762473465793	0.016126514	451.1977819	0.298844702	0.000538901
360	1.42106740400573	0.016137124	88.0619994	0.318965227	0.000500713

Tab. F.2: Variation for the study with $T = 220.00\,°C$ with the resulting permeation.

$x_{H_2^{feed}}$ $mol\,mol^{-1}$	P_{H_2} $mol\,m^{-2}\,bar^{-1}\,min^{-1}$	P_{CH_4} $mol\,m^{-2}\,bar^{-1}\,min^{-1}$	S_{H_2,CH_4} $-$	σP_{H_2} $mol\,m^{-2}\,bar^{-1}\,min^{-1}$	σP_{CH_4} $mol\,m^{-2}\,bar^{-1}\,min^{-1}$
0.3	1.443602323	0.016354227	88.27089867	1.301220143	0.000683809
0.35	1.237216098	0.017612264	70.24741777	0.233113475	0.000731332
0.4	1.082460865	0.019079978	56.73281447	0.453907992	0.001333223
0.45	0.962116086	0.020814554	46.22323796	0.357503558	0.001898465
0.5	0.865853113	0.022896052	37.81669891	0.743955634	0.000926009
0.55	0.787100992	0.025440116	30.9393633	0.444175211	0.001697765
0.6	0.721480064	0.028620212	25.20876019	0.492503467	0.001259344
0.65	0.665958808	0.032708934	20.36015035	0.231162632	0.004450144
0.7	0.618372185	0.038160609	16.20446315	0.193874696	0.00215184
0.75	0.577132703	0.045793044	12.60306476	0.275357969	0.002926721
0.8	0.541049875	0.057241893	9.451991347	0.12327401	0.003685203
0.85	0.509213419	0.076323829	6.671748848	0.338667247	0.005768168
0.9	0.480915396	0.11448966	4.200513784	0.346464802	0.000520259
0.95	0.455596949	0.229002823	1.989481801	0.177835714	0.016652334

PUBLICATIONS

Previously published reports:

DBFZ Report No. 56 Szenarien zum optimalen Einsatz von Biomasse in der Bioökonomie bis 2050
DBFZ Report No. 55 Entwicklung und Anwendung neuartiger SCR-Katalysatoren zur Niedertemperaturentstickung von Abgasen aus der thermo-chemischen Konversion biogener Festbrennstoffe – Dissertationsschrift
DBFZ Report No. 54 Transition towards a bioeconomy: discourses, vantage points, and actors' contextualized institutional work – Doctoral thesis
DBFZ Report No. 53 Hydrothermal Conversion of Hemicellulose Sugars for the Production of Furfural – Doctoral thesis
DBFZ Report No. 52 Strategies for Demand Side Management in Biorefineries – Exploring New Frontiers in Enhancing Load Flexibility and Optimization – Doctoral thesis
DBFZ Report No. 51 Emissionsminderungsstrategien zur umweltverträglichen Verbrennung (UVV) auf Basis von aktuellen Forschungsergebnissen
DBFZ Report No. 50 Biogaserzeugung und -nutzung in Deutschland - Report zum Anlagenbestand Biogas und Biomethan
DBFZ Report No. 49 Modellregion Bioökonomie im Mitteldeutschen und Lausitzer Revier
DBFZ Report No. 48 Adsorption and Membrane Filtration for the Separation and Valorization of Hemicellulose from Organosolv Beechwood Hydrolyzates – Doctoral thesis
DBFZ Report No. 47 WasteGui: Guideline for organic waste treatment in East Africa
DBFZ Report No. 46 Wasserstoff aus Biomasse
DBFZ Report No. 45 Status-Quo of organic waste collection, transport and treatment in East Africa and Ethiopia
DBFZ Report No. 44 Monitoring erneuerbarer Energien im Verkehr
DBFZ Report No. 43 Beitrag zur Optimierung des Pelletierverhaltens von Gärresten und Landschaftspflegeheu sowie deren Mischungen
DBFZ Report No. 42 Rahmenbedingungen für einen optimierten Betrieb von kleinen biomassebasierten BHKW
DBFZ Report No. 41 National Resource Monitoring for Biogenic Residues, By-products and Wastes – Development of a Systematic Data Collection, Management and Assessment for Germany
DBFZ Report No. 40 Basics of Anaerobic Digestion - Biochemical Conversion and Process Modelling
DBFZ Report No. 39 Optimierte Regelungsstrategien für Pellet-Solar-Kombiheizanlagen zur Steigerung der Systemeffizienz bei gleichzeitiger Minimierung der Energiekosten
DBFZ Report No. 38 Hydrothermal processing of biogenic residues in Germany - A technology assessment considering development paths by 2030
DBFZ Report No. 37 Economic assessment of biogas plants as a flexibility option in future electricity systems
DBFZ Report No. 36 BioplanW: Systemlösungen Bioenergie im Wärmesektor im Kontext zukünftiger Entwicklungen
DBFZ Report No. 35 Leitfaden zur Substrat- und Effzienzbewertung an Biogasanlagen
DBFZ Report No. 34 Entwicklung einer Methode zur Verwendung der Daten des Schornsteinfegerhandwerks für die energiewirtschaftliche Berichterstattung - Dissertationsschrift
DBFZ Report No. 33 Recommendations for reliable methane emission rate quantification at biogas plants
DBFZ Report No. 32 Wärmenutzung von Biogasanlagen
DBFZ Report No. 31 Die Niedertemperatursynthese von Methan in Thermoöl-temperierten Plattenreaktoren – Dissertationsschrift
DBFZ Report No. 30 Anlagenbestand Biogas und Biomethan – Biogaserzeugung und -nutzung in Deutschland
DBFZ Report No. 29 Effiziente Bioenergie für Regionen - Ergebnisse der technisch-ökonomischen Begleitforschung zur Fördermaßname Bioenergie-Regionen 2012-2015
DBFZ Report No. 28 Potenziale zur Steigerung der Leistungsfähigkeit von Biogasanlagen - Energetische Effizienz von Repoweringmaßnahmen
DBFZ Report No. 27 Neuartiger emissionsarmer Kaminofen (DBU-NEKO)
DBFZ Report No. 26 Bewertung technischer und wirtschaftlicher Entwickoungspotenziale künftiger und bestehender Biomasse-zu-Methan-Konversionsprozesse - Dissertationsschrift
DBFZ Report No. 25 Nachrüstlösung zum katalytischen Abbau von gasförmigen organischen Emissionen aus Kaminöfen
DBFZ Report No. 24 Biomasse zur Wärmeerzeugung – Methoden zur Quantifizierung des Brennstoffeinsatzes
DBFZ Report No. 23 Technisch-ökonomische Begleitforschung des Bundeswettbewerbes „Bioenergie-Regionen"
DBFZ Report No. 22 Die Biokraftstoffproduktion in Deutschland – Stand der Technik und Optimierungsansätze
DBFZ Report No. 21 Entwicklung der Förderung der Stromerzeugung aus Biomasse im Rahmen des EEG
DBFZ Report No. 20 KlimaCH4 – Klimaeffekte von Biomethan
DBFZ Report No. 19 Hy-NOW – Evaluierung der Verfahren und Technologien für die Bereitstellung von Wasserstoff auf Basis von Biomasse
DBFZ Report No. 18 Kleintechnische Biomassevergasung – Option für eine nachhaltige und dezentrale Energieversorgung
DBFZ Report No. 17 Grünlandenergie Havelland – Entwicklung von übertragbaren Konzepten zur naturverträglichen energetischen Nutzung von Gras und Schilf am Beispiel der Region Havelland
DBFZ Report No. 16 Algae biorefinery – material and energy use of algae
DBFZ Report No. 15 Politics and Economics of Ethanol and Biodiesel Production and Consumption in Brazil
DBFZ Report No. 14 Holzpelletbereitstellung für Kleinfeuerungsanlagen
DBFZ Report No. 13 Basisinformationen für eine nachhaltige Nutzung von landwirtschaftlichen Reststoffen zur Bioenergiebereitstellung
DBFZ Report No. 12 Monitoring zur Wirkung des Eneuerbare-Energien-Gesetz (EEG) auf die Entwicklung der Stromerzeugung aus Biomasse
DBFZ Report No. 11 Monitoring Biokraftstoffsektor
DBFZ Report No. 10 Ermittlung des Verbrauchs biogener Festbrennstoffe im Sektor Gewerbe, Handel, Dienstleistungen (GHD-Sektor) – Endbericht

Further information and free downloads:
https://www.dbfz.de/en/press-media-library/publication-series/dbfz-reports

DBFZ Deutsches Biomasseforschungszentrum
gemeinnützige GmbH
Torgauer Straße 116
04347 Leipzig
Phone: +49 (0)341 2434-112
E-Mail: info@dbfz.de

www.dbfz.de